# DEVELOPMENT OF A TITANIUM SHEET MANUFACTURING PROCESS VIA DIRECT POWDER ROLLING AND SPARK PLASMA SINTERING

Student: Ms Fathima Moosa

Supervisor: Dr Clinton Bemont

This dissertation is submitted in fulfilment of the requirements for the degree of

Master of Sciences: Mechanical Engineering

College of Agriculture, Engineering and Science

University of KwaZulu-Natal

February 2022

# SUPERVISOR DECLARATION

As the candidate's Supervisor I agree to the submission of this thesis


Signed




…………………………………………………………………………………




# STUDENT DECLARATION – PLAGIARISM

I, Fathima Moosa, declare that

1.  The research reported in this thesis, except where otherwise indicated, is my original research.

2.  This thesis has not been submitted for any degree or examination at any other university.

3.  This thesis does not contain other persons' data, pictures, graphs or other information, unless specifically acknowledged as being sourced from other persons.

4.  This thesis does not contain other persons' writing, unless specifically acknowledged as being sourced from other researchers.  Where other written sources have been quoted, then:
a.  Their words have been re-written but the general information attributed to them has been referenced
b.  Where their exact words have been used, then their writing has been placed in italics and inside quotation marks, and referenced.

5.  This thesis does not contain text, graphics or tables copied and pasted from the Internet, unless specifically acknowledged, and the source being detailed in the thesis and in the References sections.


Signed




…………………………………………………………………………………

# Acknowledgements

# Abstract

The intention of this research was the improvement of titanium processing in South African industry. South Africa currently has limited ability to efficiently process its titanium reserves and the results of this research, combined with other work in the associated research consortium, has the potential to lead to significant positive economic impact.

A novel method of titanium processing, combining the processes of direct powder rolling (DPR) and spark plasma sintering (SPS), was explored in the course of this research. A rolling mill was designed using modelling and simulation techniques, manufactured based on the resulting design, and the DPR-SPS process parametrically tested on the rolling mill using commercially pure titanium powder.

The mechanical aspects of this project included experimental testing on a range of titanium powder samples to determine the properties of the powder, modelling of the rolling mill behaviour using MATLAB, 3D modelling of the proposed and iterated rolling mill frame design and its components using Siemens NX and OnShape, finite element analysis of the rolling mill frame and auxiliary components using Siemens NX, and manufacture and parametric testing of the mill for titanium powder compaction.

The electrical aspects of this project included connecting and programming a variable speed drive and AC motor to control the speed of the mill rolls, simulating the behaviour of the integrated SPS-type sintering circuit using Simulink, designing a suitable method for safely and effectively transmitting the large SPS current to the rotating rolls, and building and testing the circuit for titanium compact spark plasma sintering.

The manufactured direct powder rolling mill compacts titanium powder into strip through a pair of rolls, measuring 350mm diameter and 50mm width. Each of the rolls is mounted on the same shaft as a worm-driven gear. A 5.5kW three phase AC motor drives the worm shafts, which have opposing threads to ensure the rolls rotate in opposing directions. The worm and gear arrangement serves to both evenly transmit the drive power to both rolls, and to increase the torque from the motor to the rolls. The motor is controlled using a variable speed drive – this allows the roll speed to be adjusted as necessary, to optimise the consolidation process.

The bearings used on the roll and worm shafts were designed and manufactured using an insulating bearing material to ensure the current used for sintering is not instead transmitted through the steel rolling mill frame. Flexible couplings with polymeric inserts isolate this current from the motor and between each worm gear.

The minimum density of the green compact required for further handling was determined empirically as being greater than 65 % of the theoretical density of titanium. The mill was designed for an optimal density of 81%. The density range achieved by varying the parameters of roll speed, number of passes through the mill, and roll gap, was 55 – 84%. It is expected that the strip density may be greatly increased with implementation of the improvements and parameter changes identified.

The spark plasma sintering circuit sinters the titanium either during the direct powder compaction process (simultaneous DPR-SPS), or following it (sequential DPR-SPS) during re-rolling through the same set of rolls used for compaction. A number of electrical circuits with different output types were designed for the SPS process; one of these was built and tested towards proof of concept of the DPR-SPS process. The tested circuit uses a DC source to apply a sintering current through the titanium sample. Application of the SPS current to the titanium resulted in a theoretical density increase of 11 – 14% compared to DPR only, depending on whether the processes were performed sequentially or simultaneously.

This multidisciplinary project employed a broad range of combined materials, mechanical and electrical design and analysis methods. The resulting mill can be used as is for further parametric testing, improved as will be discussed for the same process, or adapted to a range of different applications.

# Table of Contents

# List of Figures

# List of Tables

# List of Equations

# 1. Introduction

This chapter will introduce the research by giving an overview of the topic, citing the step-by-step objectives which the research aims to achieve, exploring the significance of the research presented, and explaining the organisation of the dissertation.

## 1.1. Overview

Due to its high specific strength and good thermal and corrosion resistance, titanium lends itself to several applications. South Africa has large reserves of titanium but still has room for improvement in terms of processing capacity and cost [1] [2] [3]. There is thus a strong focus locally and internationally on developing better means of processing this mineral, which could lead to meaningful economic growth in South Africa.

Direct powder rolling is a continuous powder metallurgy process used to convert powdered metal directly into sheets by compaction (and subsequent sintering). This is a cost-effective means of metal processing, especially with high-value metals like titanium where material costs are high and reduction of losses is a key consideration, and because titanium beneficiation produces powder or sponge [4] [5] [6] [7].

Sintering is a means of bonding particles through diffusion of atoms by heating them to a temperature below the melting point of the material [8] [9]. Spark plasma sintering is a type of sintering which involves passing an electric current through the powdered material in order to sinter it [8] [10]. This has several benefits when compared to conventional sintering, most notably a decreased time taken for the process, a reduction of unwanted grain growth (which improves the density of the final product), and reduction in oxidation due to more localised heating [8] [9] [11] [12].

This research is an exploration of the combination of the processes of direct powder rolling and spark plasma sintering, to be applied to titanium powder to produce a strip of titanium which ideally exhibits high density, low oxygen content, and high ductility.

## 1.2. Research Objectives

The primary objective of this research was the development of an improved method of titanium processing. To achieve this objective, it sought to combine spark plasma sintering and direct powder rolling by developing an SPS-DPR mill, and perform testing on it using titanium powder to produce sheet metal. The processing method was targeted as being cost-effective, scalable, and easy to reproduce; with the compact produced being defect-free and exhibiting high density.

The logical sequence of steps necessary to achieve these higher-level objectives, which essentially formed the sub-objectives for the research, were as follows:

1. Experimental testing of titanium powder samples to determine the powders' properties

2. Use of numeric computing software to model the rolling mill behaviour, based on the properties of the mill and the powder being rolled, as determined in (1)

3. Use of 3D modelling software to design and model a rolling mill to be used for titanium powder processing

4. Use of engineering simulation software to conduct finite element analysis on the rolling mill frame and auxiliary components designed in (3), based on the loading as determined in (2); and iterative improvement thereof

5. Design of a circuit to provide a suitable electrical current for spark plasma sintering of titanium

6. Manufacture and commissioning of the designed (3) and simulated (4) direct powder rolling mill and its designed and simulated (5) spark plasma sintering circuit

7. Initial testing of the mill through production of DPR titanium strip and DPR-SPS titanium strip

8. Determination and comparison of green density and sintered density of the strip produced in (7)

## 1.3. Research Significance

The process of designing the mill was expected to be fairly complex, and formed the heart of this research; comprehensive testing of the manufactured mill was a secondary consideration. The research conducted forms a foundation upon which to further build and improve the titanium processing industry, specifically with regards to the development of a continuous process for titanium manufacturing, which does not currently exist as for other structural metals [4] [5].

This research was submitted and accepted for oral presentation at the UKZN Postgraduate Research Innovation Symposium (PRIS) in December 2021, under the title "Development of a manufacturing process for titanium combining Direct Powder Rolling and Spark Plasma Sintering". The candidate was responsible for conducting an experimental study on titanium powder and analysing the results; writing MATLAB code based on the Johanson model to simulate expected rolling mill behaviour; preliminary finite element modelling of a rolling mill frame; and compiling and presenting this research at an online symposium. The presentation was awarded second place in the Engineering category.

An abstract was submitted and accepted for presentation of this research at the CoSAAMI conference in October 2021, under the title "Development of a Manufacturing Process Combining Direct Powder Rolling and Spark Plasma Sintering of Titanium and its Alloys". The candidate was responsible for the electrical design, simulation and analysis of a circuit to provide pulsed direct current to a titanium compact for sintering; and writing the complete manuscript to be presented at the conference. However, this conference was subsequently cancelled due to the COVID-19 pandemic, and the research was thus not presented.

## 1.4. Organisation of the Dissertation

Chapter 1 has provided an overview of the project, and set out the research objectives to be achieved.

Chapter 2 reviews, in depth, literature relating to the two primary processes upon which the research is based, namely direct powder rolling and spark plasma sintering.

Chapter 3 covers the experimental process followed for determining certain properties of the powder which are necessary in order to efficiently design the rolling mill, including the methodology followed and the results of the testing.

Chapter 4 details the design of the rolling mill, including the numerical simulation of the rolling process, the 3D modelling of the mill, the finite element analysis of the rolling mill frame and auxiliary components, and the design and simulation of the electrical circuit used for spark plasma sintering.

Chapter 5 discusses the manufacturing and commissioning processes required to bring the mill to life, including a section covering the lessons learned during these processes.

Chapter 6 summarises the parametric testing performed on the mill.

Finally, Chapter 7 provides an overall discussion of the research, including comments on the degree to which the research objectives are achieved, and makes recommendations for future work to be performed on the topics explored in this dissertation.

# 2. Literature Review

This chapter briefly discusses the properties of titanium, and the powder metallurgy process and its benefits. The balance of the literature reviewed for this chapter focusses on the exploration of the two core processes which this project aims to combine, namely the DPR process and the SPS process. There has been extensive research conducted previously on each of these processes individually, but very limited research into the combination thereof. This chapter includes overviews of each process, touching on the benefits and drawbacks of each, and detailed reviews of specific DPR and SPS research relevant to the system we wish to manufacture. The literature selected has been used to guide the design and testing processes. References [83] – [117] are not directly cited but were reviewed and found useful as part of this work.

The sections in this chapter devoted to Direct Powder Rolling and Spark Plasma Sintering include detailed analyses of published works on these topics, which are believed to be relevant both in the understanding of existing systems and development of the novel system which is the subject of this dissertation. For the Direct Powder Rolling section, the most applicable aspects of the literature are discussed at the conclusion of each presented publication. For the Spark Plasma Sintering section, a separate conclusion is provided at the end of the section to discuss the most applicable aspects of all publications reviewed for this section.

## 2.1. Titanium

Titanium has excellent mechanical properties but is very expensive, limiting its use to applications where its high cost is outweighed by the need for high performance [13] [14] [15]. Cost reduction may be achieved through direct conversion of the powder into metal products (i.e. through powder metallurgy), as an alternative to conventional processing methods.

Titanium was discovered in 1791 [16]. However, pure titanium was only successfully extracted in 1910, with large quantities of pure titanium being produced in 1932 and malleable sponge titanium being produced in 1940, after which titanium industrialisation was achieved [16] [5].

Titanium is the ninth most plentiful element, and the fourth most plentiful structural metal in the earth [6]. However, due to titanium's high reactivity in non-inert environments [17], titanium in nature is only found in its compounds, and not in its elemental state. The high cost of titanium products thus lies not in a scarcity of the raw material, but rather in the processing thereof (including secondary processing of the metal) [6]. No continuous process (ore to final product) currently exists for titanium manufacturing [4] [5].

One method that can be used to directly reduce titanium metal from its oxide, through molten salt electrolysis, is the Fray Farthing Chen (FFC) Cambridge Process [18], but this process presents challenges such as low efficiencies, incomplete reduction, and poor product purity [7]. Additionally, there are several patent issues preventing its commercialisation [7]. The Kroll process (which is expensive and energy-intensive) produces titanium as a sponge-like material, which can then be processed further into usable powder. The Kroll process requires chlorination of titanium ore to produce titanium tetrachloride, then reduction of the titanium in this compound to its elemental state using magnesium [6] [7] [19] [20]. The Hunter process is similar to the Kroll process, but uses sodium as a reducing agent instead of magnesium [7] [20].

With a density of 4.51 g/cm$^3$, titanium is treated as the heaviest of the light metals. Titanium alloys can often be used at operating temperatures in excess of 500 °C (compared to 130°C for aluminium with a density of 2.71g/cm$^3$) [21] [22] .

## 2.2. Powder Metallurgy

### 2.2.1. Overview

Powder Metallurgy (PM) is a processing technique that involves three basic steps [5]:

1. Production of a metal powder

2. Forming and compacting of the powder to the desired shape

3. Sintering of the compact to form a strengthened and integrated component

PM processing is more competitive than conventional ingot metallurgy processing; this is especially true for flat products requiring several re-rolling steps, or complicated parts requiring a large amount of material removal through machining [23]. Conventional casting and forging processes may also result in non-uniform micro-structure distribution, whereas uniform micro-structures (homogeneity) can be achieved through careful control of the PM process. Another benefit of PM is the ability to produce alloyed materials which would be either very difficult or prohibitively expensive to produce using conventional methods [15].

PM results in the production of parts that require minimal further processing to achieve their required dimensions, as they are very close to their final dimensions after the PM route – a characteristic referred to as near-net-shape [5]. PM thus results in minimal time and material wastage through machining, which is especially beneficial in cases where lead times are critical or material costs are high [20] [24] [25].

The quality of the final product of the PM process is dependent on the characteristics of the metal powders used, as well as the parameters used in the processing of the powders. Additionally, processing metal powders in an inert environment limits the formation of oxides, which may influence the compaction and sintering processes. This inert environment may be achieved through use of a vacuum or shielding with an inert gas. There may be potential to reduce the inert volume required (and therefore the operational cost) by use of nozzles to direct an inert gas into the volume immediately surrounding the material being processed [26].

### 2.2.2. Powder Production Techniques [5]

Metal powders are typically produced mechanically, electrically, or chemically.

Mechanical powder production techniques produce powders which are typically irregular in shape and may include contaminants. The different methods are as follows [27]:

1. Impaction: application of rapid impact to bulk material, creating cracks to reduce size

2. Attrition: application of a rubbing motion to wear down bulk material

3. Shearing: cutting to form a cleavage fracture in bulk material

4. Compression: application of a compressive force to break the material into powder

Electrolytic powder production typically results in powders which are high in purity. This method involves precipitation of powder at the cathode of an electrolytic cell through dissolution of the anode under an applied voltage. The precipitate is then removed, washed, dried, ground into a powder, and annealed [27].

Finally, the chemical powder production techniques are as follows [27]:

1. Decomposition of solid by gas: oxide reduction through thermo-chemical reactions, followed by grinding to fracture the inter-particle diffusion bonds and achieve the desired particle size

2. Decomposition of metal hydrides: heating of metal in hydrogen, milling the resulting brittle hydride into powder, and de-hydriding by heating the powder in a vacuum to the same temperature as used when forming the hydride [6] [20] [24]

3. Atomisation: driving molten metal through an orifice and forming a powder therefrom using a high-pressure spray of gas or water [6]

### 2.2.3. Compaction [28]

Powder compaction is used to compact powder into a desired shape, reduce its porosity, and improve green strength for subsequent processing.

Green strength is a mechanical property used to describe the ability of a compacted powder to maintain its dimensions during handling before any heat treatment has been applied. This is a critical consideration to ensure successful processing without disintegration of the compacted part. To increase green strength, one should typically [5]:

1. Increase particle surface roughness

2. Increase powder surface area

3. Decrease powder apparent density

4. Increase compaction pressure

5. Decrease surface oxidation and contamination

### 2.2.4. Sintering

The compacted green product cannot be used before the material is sintered. Sintering is a heat treatment process whereby a material is heated to a temperature below its melting point, to induce densification and shrinkage through diffusion bonding of the particles [9]. As the particle size decreases, the surface energy per unit volume increases (due to the higher surface area-to-volume ratio of the smaller particles). Thus, the smaller the particles, the higher the free surface energy available to drive the sintering process.

Two events are necessary before bonding can occur: the removal of inter-particle lubricants, and the reduction of oxides on the particles' surfaces [29] [30] [31] [32]. This is usually achieved through careful parametric control in conventional sintering furnaces, but may be achieved more efficiently through the use of a more novel sintering processes, such as spark plasma sintering [33].

## 2.3. Direct Powder Rolling

### 2.3.1. Overview

Compaction of powder through a rolling mill is a continuous process, and is achieved by feeding the powder to be compacted between two rolls. The surface friction forces the powder towards the smallest gap, or minimum roll gap, leading to high stresses imparted on the powder and subsequent formation of a compact [34]. Direct powder rolling as a consolidation technique for producing metal sheet or strip has the potential to allow for the formation of unique alloyed products too difficult or expensive to produce through conventional processes. Upon further processing, these products exhibit properties equivalent to their ingot metallurgy counterparts [35]. Process advantages include the continuity of the process, which allows for high production capacities; low compaction costs; low energy consumption (as the only power that is required is that which is used to drive the rolls, and the screw-down mechanism if applicable), and the ability to compact high-temperature materials. A major disadvantage is that of powder leakage, which can occur between the rolls or between the rolls and cheek plates. However, the leaked powder can often be recycled through the process. The prevention of leakage is thus not amongst the most critical design considerations.

In the development of a suitable rolling mill, certain published works were of particular interest to the author. Each of these works provided guidance with respect to a particular aspect of the DPR process development. These included, on a very basic level:

1. The theory behind powder rolling mills, and the basis around which to design a mill

2. The effect of varying input parameters on the output of the mill

3. Techniques utilised to improve the final product of the DPR mill

### 2.3.2. DPR Theory: Johanson's Model [36]

*Importance of the research*

There are three distinct regions in a direct powder rolling mill, namely the slip region, nip region and release region. In 1965, Johanson developed a mathematical model for DPR mills for the determination of the distribution of pressure exerted by the rolls on the powder, the nip angle (i.e. the boundary between the regions of slip and nip), the magnitudes of the roll separating force and roll torque, and the ratio of maximum (compaction) pressure to the feed pressure in the mill, which he termed the mechanical advantage.

Johanson's depiction of a direct powder roll press can be seen in Figure 1.
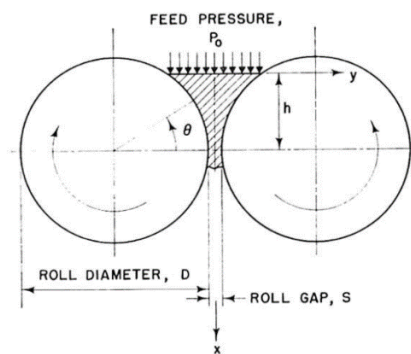


*Figure 1: A powder roll press [36]*

The characterisation of each of the three regions in the DPR process is as follows [34] [36] [37] [38] [39]:

1. The slip region, where

    a. The powder passes the feed angle

    b. The rolls move faster than the powder, causing slip at the roll surface

    c. The powder experiences low shear stress

    d. The roll surfaces do not have enough normal pressure to grab the powder

2. The nip region, where

    a. The powder passes the nip angle

    b. The powder moves at the same speed as the rolls, creating a condition of no slip

    c. The powder experiences high shear stress

    d. Continuous shear deformation of the powder occurs

    e. The powder compacts

3. The release region, where

    a. The material passes the minimum roll gap

    b. The compact is ejected

    c. The compact travels faster than the rolls, once again causing slip at the roll surface

These regions are illustrated in Figure 2; the slip region is represented in light grey, the nip region in dark grey, and the release region in black.
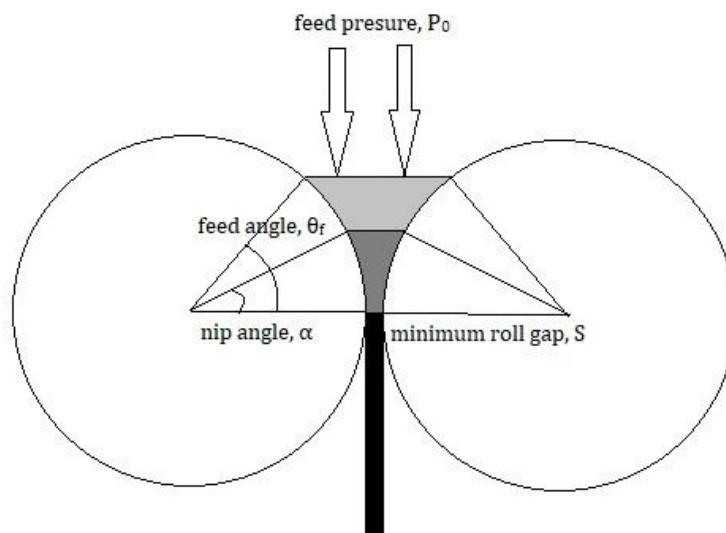


*Figure 2: Regions in a DPR mill*

In the course of his research, Johanson determined that the maximum pressure exerted by the rolls on the material is a function of:

1.  The flow properties of the powder being rolled, namely:

    a.  Compressibility of the powder, K

    b.  Internal friction of the powder, $\delta$

    c.  Surface friction between the powder and the rolls, $\phi$'

2.  The properties of the mill, namely:

    a.  Roll diameter and width, D and W

    b.  Minimum roll gap, S

    c.  Surface condition of the rolls (affecting $\phi$' above)

    d.  Feed pressure (applied at the feed height), $P_0$

The consequence of this is that, using his research, a direct powder rolling mill can be designed for a desired mill output with a specific powder, once the properties of the powder have been established.

The first powder property that shall be discussed is that of compressibility. The compressibility factor for a material, K, describes the relationship between the pressure applied to a compressible powder, and the resultant density of the compact thus formed. This pressure-density relationship, as well as the determination of the compressibility factor K for a material, is shown in Figure 3.



$$\sigma_1/\sigma_2 = (\gamma_1/\gamma_2)^K$$
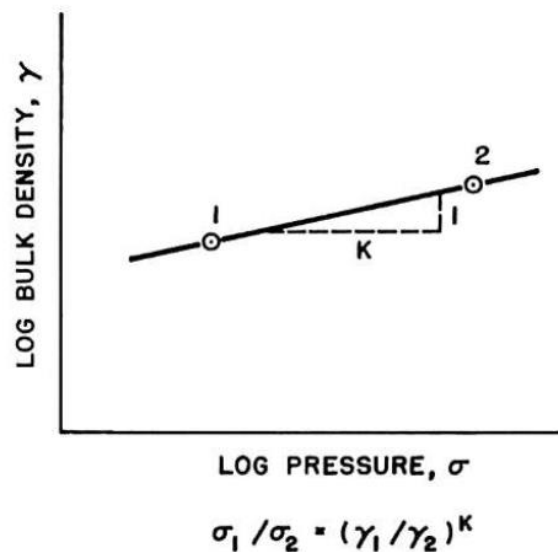
*Figure 3: Pressure-density relationship for compressible materials [36]*

When designing a DPR mill, a useful early step in the process is selecting the desired density of the compact to be formed through the mill. According to Johanson, the pressure required to produce the desired compaction of a powdered material should be known, in order to design the mill. Using the pressure-density relationship means that if a specific density is required from the compact, and the compressibility of the powder being compacted is known, the required compaction pressure can easily be determined. This value can then be used to calculate the roll dimensions and loads necessary to provide that compaction pressure for the specific material.

The two other key powder properties required for the mill design are the internal friction angle, and the wall/surface friction angle. These are necessary to determine the nip angle and the pressure distribution in the nip region, thus the loads on the mill (namely the roll separating force and roll torque).

The consequence of Johanson's research is that if the nip angle and the bulk density of the powder at the nip angle are known, the maximum pressure exerted on the material (and thus the compact density) can be calculated. Previous research did not allow for determining the nip angle and the bulk density at the nip angle without actually rolling the powder in a roll press, and the results obtained from this rolling would be specific to the particular material and pressure used. Johanson's research, by contrast, allows for the determination of these values mathematically rather than experimentally.

*Determination of the nip angle*

The equation below allows one to determine the stress at any point in the slip region:

<center>*Equation 1: Stress in the slip region [36]*</center>

$$\sigma_0 = P_0/(1 - sin\delta)$$

The equation below allows one to determine the stress at any point in the nip region:

<center>*Equation 2: Stress in the nip region [36]*</center>

$$\sigma_\theta = \sigma_\alpha \left[ \frac{d/D + (1 + S/D - cos\alpha)cos\alpha}{d/D + (1 + S/D - cos\theta)cos\theta} \right]^K$$

From the stress equations above, and using the Jenike-Shield criterion [40] the pressure differential with respect to the vertical coordinate can be determined.

The pressure differential in the slip region is given by:

<center>*Equation 3: Pressure differential in the slip region [36]*</center>

$$\frac{d_\sigma}{d_x} = \frac{4\sigma(\pi/2 - \theta - v)tan\delta}{\frac{D}{2}[1 + S/D - cos\theta][cot(A - \mu) - cot(A + \mu)]}$$

where

$$A = \frac{\theta + v + \pi/2}{2}$$

The pressure differential in the nip region is given by:

<center>*Equation 4: Pressure differential in the nip region [36]*</center>

$$\frac{d\sigma}{dx} = \frac{K\sigma_\theta(2cos\theta - 1 - S/D)tan\theta}{\frac{D}{2}[d/D + (1 + S/D - cos\theta)cos\theta]}$$

When the pressure differential for both regions are plotted against the angular position, the graphs in Figure 4 are generated.
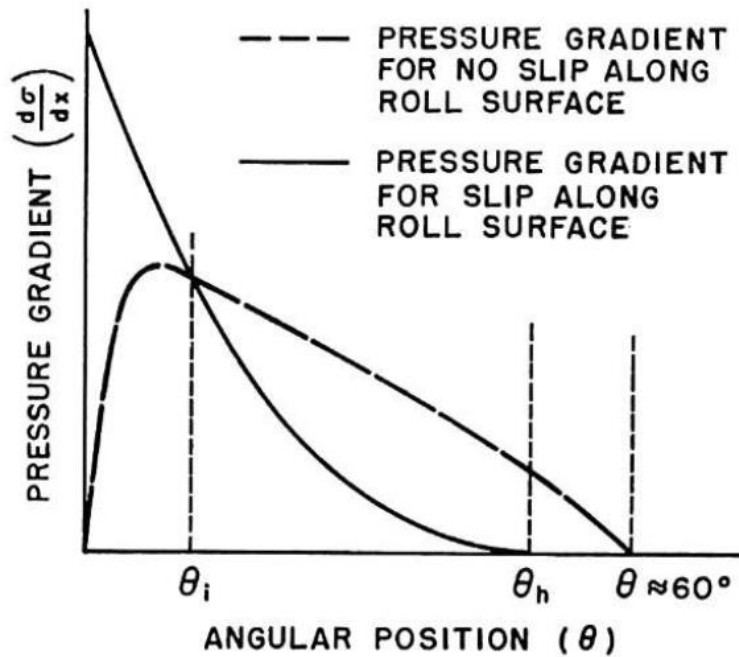


*Figure 4: Pressure gradient versus angular position*

The nip angle is the position at which the powder changes from slipping along the roll to moving with the roll (i.e. the powder moves from the slip to the no-slip condition). The nip angle thus occurs at the intersection of the two curves, given by $\theta_i$ in the figure above.

Johanson determined that slip occurs in the region where $\theta_i < \theta < \theta_h$, and that no slip occurs in the region where $0 < \theta < \theta_i$. He used the following reasoning for this determination:

1. Consider the possibility that no slip occurs at the roll surface between the entry angle ($\theta_h$) and the nip angle ($\theta_i$). The maximum pressure gradient possible is given by the slip condition, and the pressure gradient of the no slip condition is greater in this region (looking at the graph) – thus we cannot use the condition of no slip in this region, and slip occurs in the region $\theta_i < \theta < \theta_h$.

2. Consider the possibility that slip occurs at the roll surface between the nip angle ($\theta_i$) and the minimum roll gap ($\theta = 0$). Continuity requires a larger density gradient (and thus a large pressure gradient) for the condition of no slip than for the condition of slip. The pressure gradient is higher for the condition of slip than for the condition of no slip in this region (looking at the graph) – thus in order to not violate continuity, no slip can occur in the region $0 < \theta < \theta_i$.

The position of the nip angle at the intersection of the two curves as described above results in a smaller total roll force than if the nip angle had been in any other position. This is clear upon examining the graphs, as the pressure gradient is always at a minimum as per the reasoning above.

12

*Determination of the roll separating force and roll torque*

To determine the roll force and torque, which are critical to the mill design, the following steps may be followed:

1. Determine the material properties of internal friction, wall friction, and compressibility through experiment

2. Determine the nip angle using the values determined in the step above and by equating the stress gradients in the nip and slip regions

3. Determine the roll force factor based on K and the mill dimensions (roll gap and diameter), and subsequently the roll force based on the maximum pressure exerted on the material

4. Determine the roll torque factor based on K and the mill dimensions (roll gap and diameter), and subsequently the roll torque based on the maximum pressure exerted on the material

Step 1 above is explored in the experimental chapter, while steps 2 – 4 are explored in the MATLAB section of the design chapter. The equations for calculation of roll separating force and roll torque are given below.

*Equation 5: DPR mill roll separating force [36]*

$$RF = P_m WDF/2$$

*Equation 6:DPR mill roll force factor [36]*

$$F = \int_{\theta=0}^{\theta=\alpha} \left[ \frac{(d+S)/D}{d/D + (1 + S/D - \cos\theta)\cos\theta} \right]^K \cos\theta d\theta$$

The two equations above can be used to calculate the roll separating force, which is an important value to consider when designing the roll shafts, bearings, and the supporting frame. The pressure in the nip region is much higher than the pressure in the slip region, thus the roll separating force due to the pressure in the slip region is neglected and the nip angle is used as the upper limit of integration.

*Equation 7: DPR mill roll torque [36]*

$$TQ = P_m WD^2 T/8$$

*Equation 8:DPR mill roll torque factor [36]*

$$T = \int_{\theta=0}^{\theta=\alpha} \left[ \frac{(d+S)/D}{d/D + (1 + S/D - \cos\theta)\cos\theta} \right]^K \sin2\theta d\theta$$

The two equations above can be used to calculate the torque on each roll, which is another important value to consider when designing the roll shafts, bearings, and supporting frame. The pressure in the nip region is much higher than the pressure in the slip region, thus the roll torque due to the pressure in the slip region is also neglected and the nip angle is used as the upper limit of integration.

*Determination of the mechanical advantage*

The mechanical advantage of the mill is the ratio of the maximum pressure on the material $P_m$ (at the minimum roll gap) to the applied/feed pressure $P_0$. This is given by the equation below.

$$P_m/P_0 = \sigma_m/\sigma_0 \frac{1 - sin\delta}{1 + sin\delta}$$

As can be seen from this equation, the mechanical advantage is directly proportional to the pressure ratio (the ratio of the maximum to minimum mean normal stress) for a given material.

*Effect of varying mill and material parameters on the nip angle*

Johanson's method for determination of the nip angle was further used to determine what effect varying parameters of both the mill and the material used would have on the nip angle. The effect of varying the roll gap on the nip angle is shown in Figure 5.
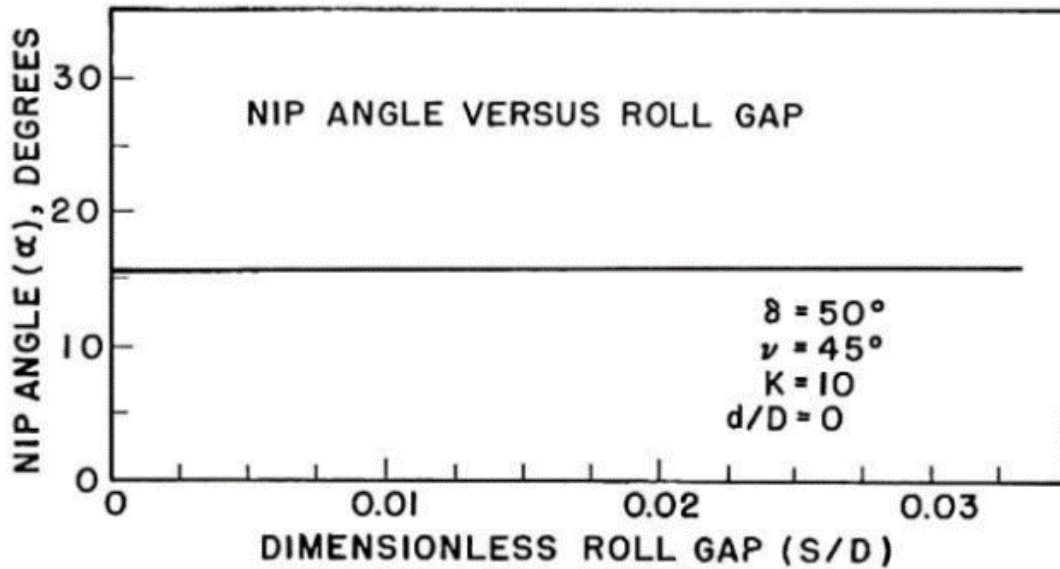


*Figure 5: Nip angle versus dimensionless roll gap [36]*

The graph of nip angle versus dimensionless roll gap illustrates that the varying the geometry of the mill has no influence on the nip angle – there is no variation of nip angle with the dimensionless parameter of roll gap or roll diameter. Note however that this is only true for small values of roll gap relative to roll diameter; where the roll gap is very small compared to the diameter, the nip angle is only dependent on the material properties of compressibility (K), internal friction ($\delta$), and wall friction($\phi$').

The effects of varying the compressibility and the effective angle of internal friction on the nip angle are shown in Figure 6.
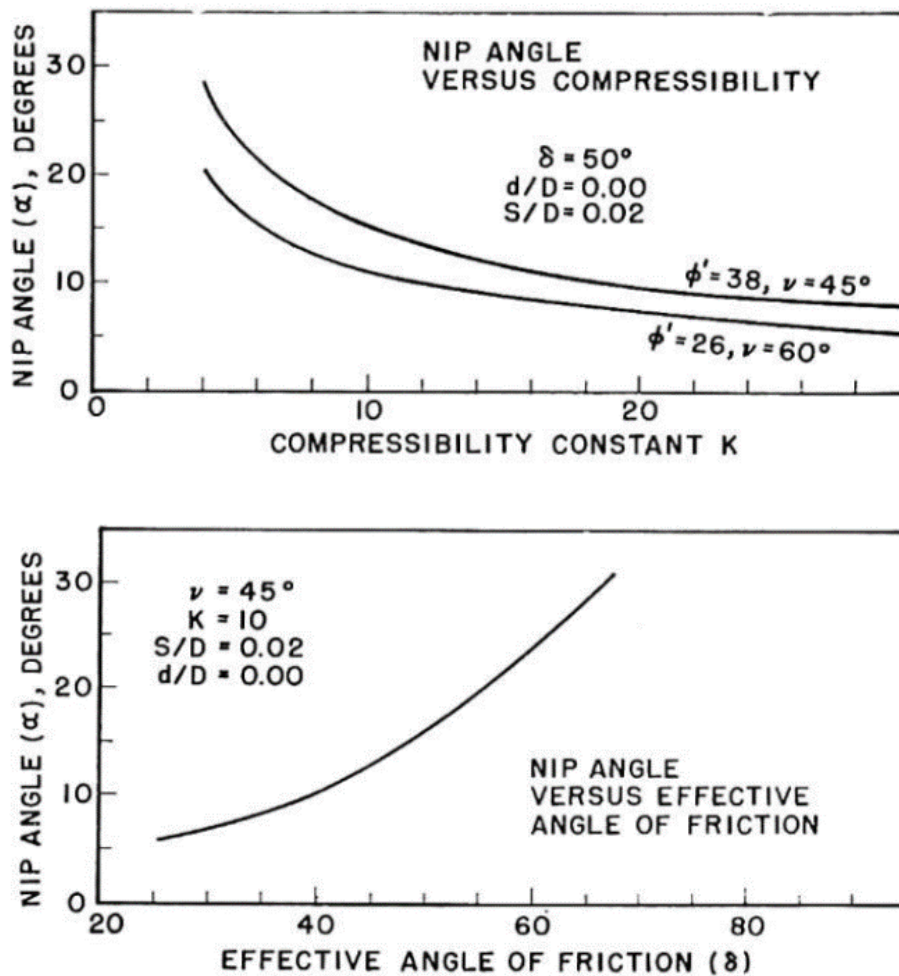


*Figure 6: Nip angle versus compressibility constant and effective angle of friction [36]*

The graph of nip angle versus compressibility illustrates that very compressible materials (with a small K value) have larger nip angles than incompressible materials (with a large K value). We also see from this graph that the nip angle increases with increasing surface friction, especially when highly compressible powders are used.

Considering the graph of nip angle versus effective angle of friction, it is clear that the greater the internal friction of the material, the greater the nip angle. Comparing the two graphs, we see that the internal friction affects the nip angle to a greater degree than the surface friction does.

We also conclude that more compressible, higher friction materials compacted with rougher rolls will be dragged into the mill and be subject to a condition of no slip sooner (i.e. at a larger nip angle) when compared to less compressible, lower internal friction materials compacted with smoother rolls.

The above results indicate that a specific powder rolling mill may have a wide range of operational variation depending on the properties of the material being rolled.

*Effect of varying material parameters on the pressure ratio*

The pressure ratio is compared to the dimensionless roll gap for varying material property parameters. Regardless of the material properties, the roll gap is inversely proportional to the pressure ratio, i.e. as the roll gap is increased, the pressure ratio (and thus the mechanical advantage of the mill) decreases. These results can be seen by considering the graphs in Figure 7.
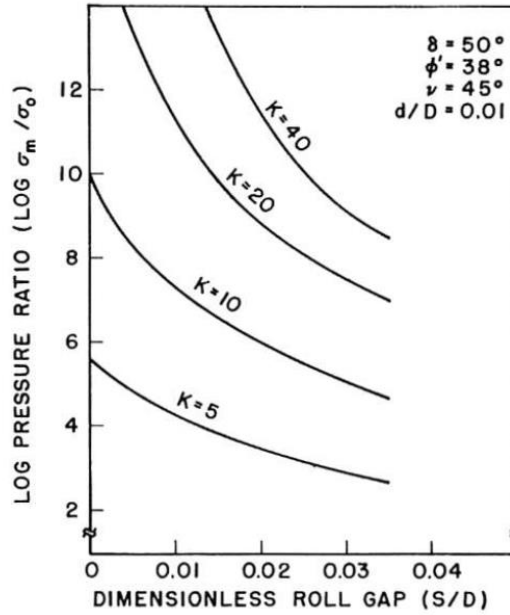


*Figure 7: Effect of compressibility on pressure ratio [36]*

The compressibility constant K is proportional to the mechanical advantage (i.e. materials with higher K values, which are less compressible, result in a higher mechanical advantage). This is also shown in Figure 7.
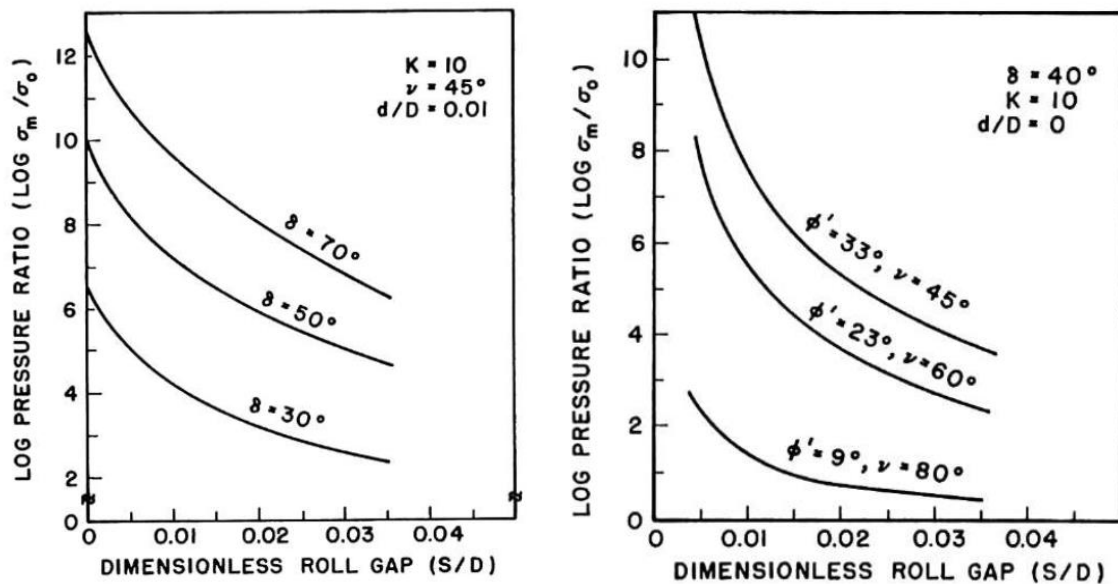


*Figure 8: Effect of internal friction and wall friction on pressure ratio [36]*

The internal friction is proportional to the pressure ratio. However, note that the mechanical advantage is calculated from the above pressure ratio multiplied by a factor dependent on the internal friction, so it is not as simple as stating that a higher internal friction will result in a higher mechanical advantage.

The surface friction is proportional to the mechanical advantage (less friction results in a lower mechanical advantage, thus we do not want to lubricate the rollers and would prefer a rough roll surface). Rougher rolls drag the material into the roll bite with greater force.

The effects of internal friction and surface friction on pressure ratio are shown in Figure 8.

*Effect of the weight of the material on the pressure ratio*

The relationship of pressure ratio to dimensionless roll gap as explored above is valid only when the weight of the material being compressed is neglected, i.e. when the powder is force-fed into the rolls. For gravity feed, the weight is important and the pressure ratios must be increased. This is shown in Figure 9.
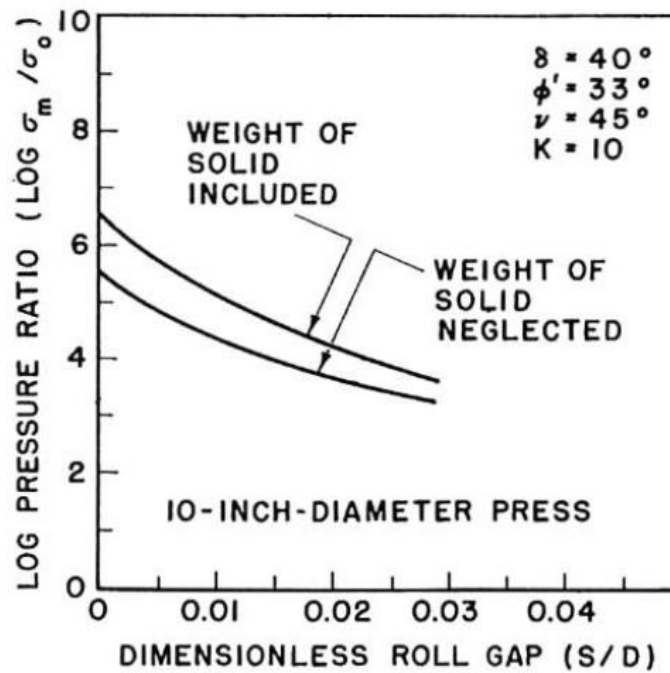


*Figure 9: Pressure ratio versus dimensionless roll gap, with and without weight of compressed material considered [36]*

The graph above shows the effect of including the weight of the material being rolled in the calculation of the pressure ratio; including the weight of the rolled material results in a higher calculated pressure ratio (and thus mechanical advantage).

This relationship is not explicitly considered when designing the mill, but is included here as one of the general considerations for the Johanson model.

*Effect of material loss on the pressure ratio*

The equation for mechanical advantage explored above assumes, through continuity, that there is no material loss from the rolls between the nip angle and the minimum roll gap. In reality, the effect of material loss may be appreciable.

$$P_m/P_0 = \sigma_m/\sigma_0 \left(\frac{1 - sin\delta}{1 + sin\delta}\right)(1 - f)^K$$

The above equation is used to correct the pressure ratio (and thus the mechanical advantage) based on possible material loss from the mill during rolling.

*Discussion*

Johanson has proposed, through his research, a theoretical method for calculating the mill dimensions and the roll force, roll torque and feed pressure required to produce a desired roll compaction pressure based on a few inputs for the material properties which can be determined experimentally with relative ease. His theory can thus be used as a basis for designing a DPR mill. The theory discussed here has been used to develop a MATLAB model to simulate the behaviour of the mill, using powder characteristics determined experimentally as inputs, and roll forces and torques as outputs. These roll forces and torques were then used as loading conditions for the finite element analysis employed in designing the rolling mill frame, to ensure a suitably dense compact could be produced without failure of the mill.

**2.3.3. Experimental Validation of DPR Theory: Bindhumadhavan et al [41]**

*Importance of research*

In 2005, Bindhumadhavan et al conducted research on the direct powder rolling of microcrystalline cellulose. This aim of the research was to experimentally validate Johanson's model [36], which at that time had yet to be accomplished.

An illustration of the direct powder rolling mill used by Bindhumadhavan et al in their experiments is shown in Figure 10.



*Figure 10: Experimental apparatus, Bindhumadhavan et al [41]*

*Determination of material properties*

Before this team could verify Johanson's model through direct powder rolling experiments, it was necessary to determine the properties of the material being used. This was done as below:

1. Rotational shear tests were used to measure

    a. The effective angle of internal friction, $\delta$

    b. The surface friction, $\varphi$

2. A uniaxial test was used to measure

    a. The compressibility, K

18

The graph in Figure 11 is a logarithmic plot of the density of the compact formed at different applied pressures in the course of their experimentation. It is from slope of this graph that the compressibility was determined.
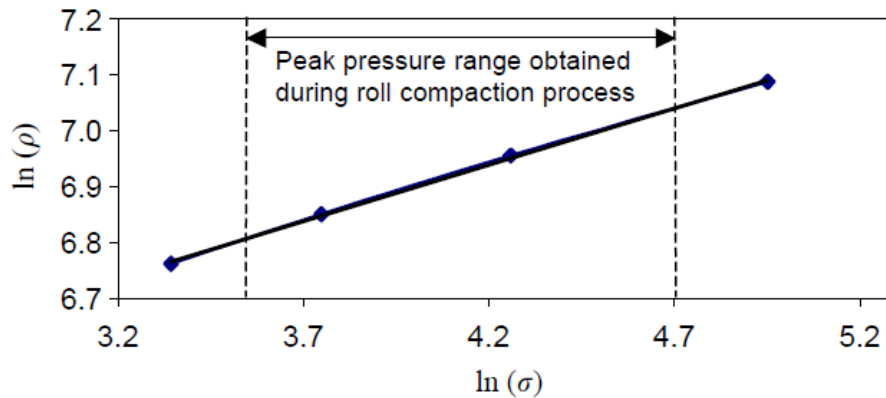


*Figure 11: Experimental determination of pressure-density relationship [41]*

*Determination of nip angle*

The material properties having being determined, it was now possible to determine the theoretical nip angle using Johanson's theory, and to then validate this experimentally.

The nip angle was determined in the following ways:

1. Solving for the nip angle through equating the differential pressure for the slip and no slip conditions (i.e. directly from Johanson's model)

2. Determining the nip angle experimentally through a direct powder rolling experiment

3. Determining the pressure profile and pressure-density relationship experimentally, and using this to calculate the nip angle using Johanson's model

The results of these calculations and experiments are shown in Figure 12.
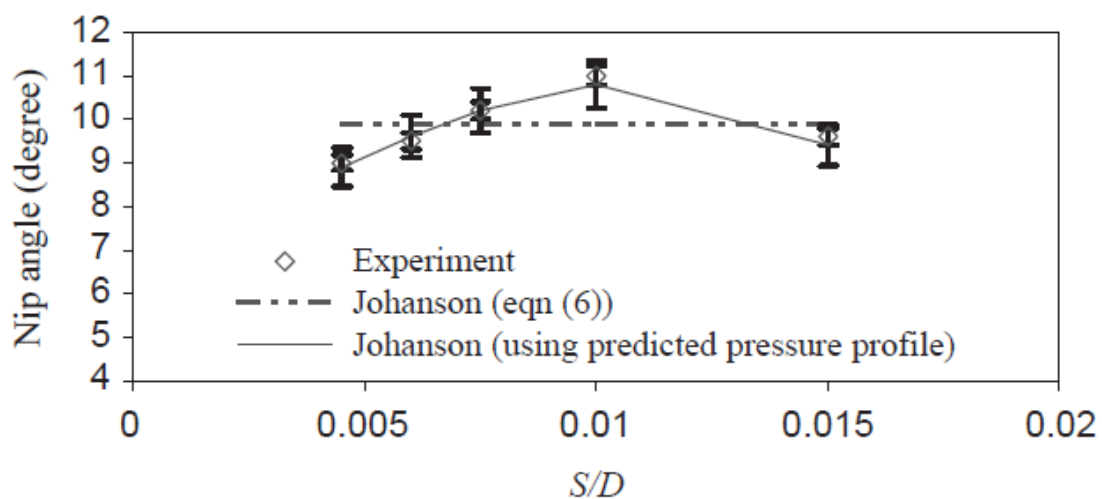


*Figure 12: Nip angle as determined theoretically and experimentally [41]*

As per Johanson's model, the nip angle should be independent of the roll gap if the dimensionless roll gap is sufficiently small. The horizontal line depicts the expectation of the nip angle based on the method of calculation (1) above – Figure 13 shows how the nip angle was determined for each specific roll gap.
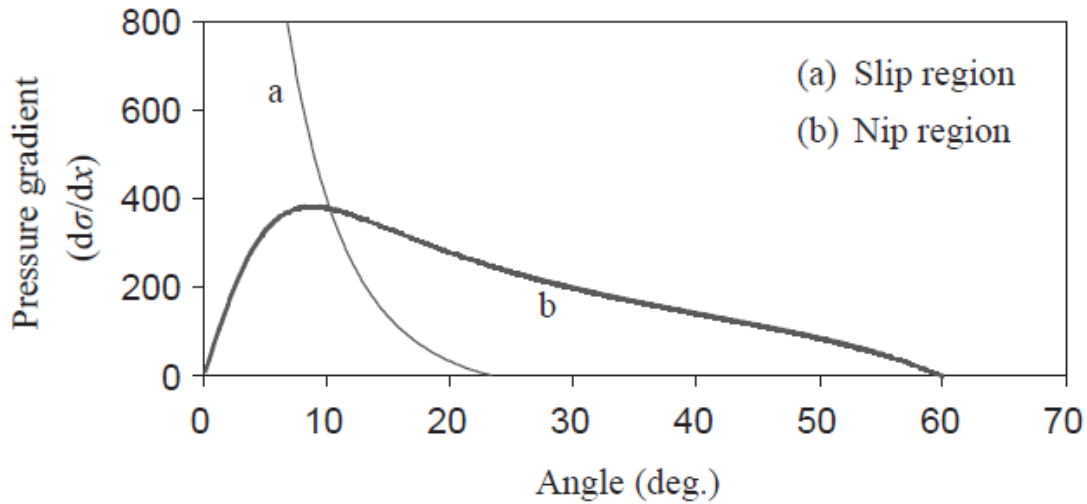


*Figure 13: Theoretical determination of nip angle [41]*

Experimentally, as per method (2), there were slight variations of the nip angle with varying values of the dimensionless roll gap. This was explained by inaccuracies caused by the sensitivity of the pressure sensor which was used to detect the position of the nip angle during experimentation. The experimental nip angle was found to agree very closely with the nip angle determined from the method of calculation (3) above.

*Determination of the pressure profile*

The pressure profile was calculated using Johanson's theory for pressure in the nip region, and verified experimentally by direct powder rolling with varying values of roll gap. This is shown in Figure 14.
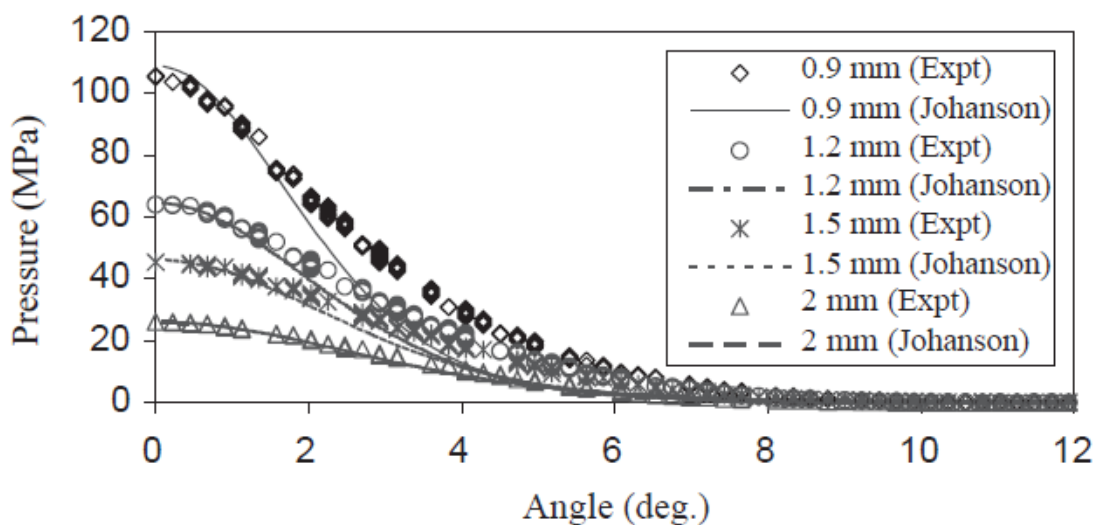


*Figure 14: Pressure profile as determined theoretically and experimentally [41]*

The results, as seen above, indicate that the magnitude of the pressure exerted on the bulk material by the rolls increases:

1.  With decreasing distance from the minimum roll gap, i.e. as the material gets pulled further into the roll bite, and

2.  With decreasing value of the roll gap

Both these observations agree with the theory of the Johanson model, and the actual experimental values followed the calculated values quite closely. Variations from the theory with smaller roll gaps were explained by the powder particles approaching the minimum roll gap in size.

The effect of roll speed on the peak pressure achieved by the mill, which was determined experimentally and compared to the calculated peak pressure values for specific roll gaps, can be seen in Figure 15.
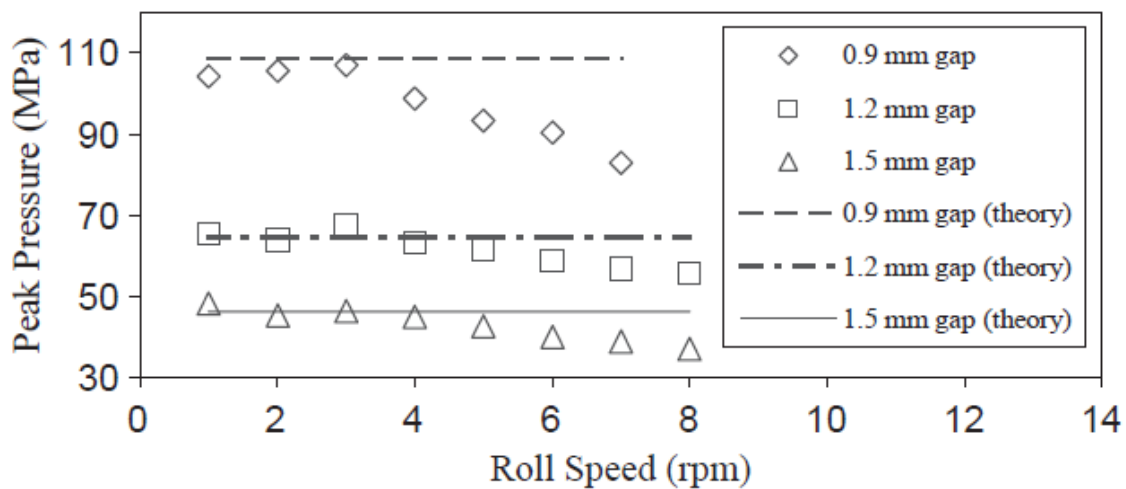


*Figure 15: Peak pressure versus roll speed as determined theoretically and experimentally [41]*

At low speeds, the peak pressure was independent of the roll speed, and was closely correlated to values of peak pressure versus roll gap calculated from the Johanson model. However, at higher speeds, the peak pressure decreased with increasing roll speed. The Johanson model does not take roll speed into account, but Bindhumadhavan et al explained that this discrepancy in peak pressure at high speeds was due to:

1.  Decreased roll force and torque for the same applied power at higher speeds, and

2.  Entrainment of air in the powder at higher speeds

*Discussion*

Bindhumadhavan et al did not explore the roll separating force or roll torque in the course of their research. However, they did validate a portion of Johanson's theory for direct powder rolling by exploring the nip angle and pressure profile, and confirming that the values achieved experimentally follow the theory quite closely. Johanson's model can thus be used with confidence for the calculation of the nip angle and peak pressure when designing a gravity-fed direct powder rolling mill.

### 2.3.4. Application of DPR Theory to Produce Fully Dense Titanium: Moxson and Duz [15]

*Importance of research*

In 2007, a patent was published by Moxson and Duz on the processing of alloyed titanium powder which was aimed at producing fully dense titanium strip. This involved multiple process steps, which did indeed result in a strip with a final relative density of close to 100%.

The proposed consolidation technique consisted of the following steps:

1. Powder preparation

2. Direct powder rolling

3. Cold re-rolling

4. Sintering

*Powder preparation*

The preparation of the powder (specifically the particle size optimisation) was described as a key factor in achieving a final product of close to 100% relative density.

The materials used to produce the optimised alloy are as follows:

1. Soft commercially pure titanium particles for the base

2. Hard alloys consisting of:

   a. Master alloy powder consisting of 60 weight % aluminium and 40 weight % vanadium to produce the desired final chemistry, with particles attrited to smaller than ten times the size of the titanium base particles

   b. Reinforcing particles of titanium carbide to improve the mechanical properties

   c. Graphite powder mechanically alloyed with chromium and commercially pure titanium, with particles attrited to smaller than ten times the size of the titanium base particles

*Direct powder rolling*

The details of the mill in which the initial powder rolling was carried out are listed below:

1. The mill rolls were positioned horizontally, and were gravity fed by a single hopper

2. Each of the rolls had a different diameter in order to produce a bent green strip

3. The diameters of the rolls for this mill were $40 - 250$ times larger than the desired strip thickness

4. The green strip produced in this process had a relatively low density of $60\pm20\%$ of the theoretical value; this is described as being a key element, providing the ductility necessary for effective densification of approximately 99% in further process steps

*Cold re-rolling*

Cold re-rolling was carried out on two different mills, termed densification mills. The first densification mill consisted of a horizontal stand with vertical edging rolls, and was in-line with the direct powder rolling mill. The second was a single horizontal stand, and was used after annealing in a vacuum (for stress relief). Details of these processes are as follows:

1. The roll diameters are 1.1 – 5 times larger than those of the direct powder rolling mill, in order to impart large compressive forces to the green strip

2. For at least one of the roll passes, the speed of the vertical edging rolls should differ by 5-15% in order to promote densification of the green strip by shear deformation

3. The rolled green strip produced at the end of both these processes had a density of 90±10% of the theoretical value

*Sintering*

Conventional furnace sintering was performed in a vacuum, for 4 hours at 1150°C, as the final stage of the consolidation process. The only requirement of the sintering was to avoid the liquid phase during this process. The final product displayed the following mechanical properties:

1. Final relative density of 99.8%

2. Ultimate yield strength of 1110 – 1193MPa

3. Yield strength of 890 – 1007MPa

4. Elongation of 3.2 – 3.9%

*Challenges overcome from previous research*

As stated by the authors, the challenges to achieving 100% relative density encountered during previous research were as follows:

1. The presence of residues of organic binders that do not allow for effective densification through compaction, and evaporation of which creates voids that cannot be removed through sintering. This is termed gaseous porosity.

2. The diffusion voids created by interactions between the base titanium particles and the alloying elements at the sintering temperature. This is termed diffusion porosity.

Both these challenges, gaseous and diffusion porosity, are said to have been overcome by the authors through the processes described in their patent.

*Discussion*

The process as described above gives a good guideline for the production of fully-dense alloyed titanium strip. The lessons learned from this publication include:

1. The importance of using an alloy much smaller than the titanium matrix in order to fill the voids in the final strip.

2. The effect that the selection of alloys has on the mechanical properties of the strip produced.

3. The importance of producing a ductile green strip through the direct rolling step which will allow for good densification in further rolling steps.

4. The range of diameters that should be considered based on the strip thickness required.

### 2.3.5. Parametric Study of DPR on Titanium: Zhang [5]

*Importance of research*

In 2010, Zhang undertook a parametric study of DPR of stainless steel and titanium. This research was a study of the effect of varying operational parameters (rolling speed, roll gap, roll surface width, powder feeding rate) on the final product of the DPR process, the overall objective being to produce as dense a strip as possible (first through DPR, then through subsequent hot rolling).

*Process flow*

The process flow for the titanium rolling setup was as follows:

1. Production of a green strip through direct powder rolling

2. Sintering of the green strip at 1200 °C in a vacuum environment for 2 hours

3. Deformation via cold rolling to 50% of the original green strip thickness

4. Post-deformation annealing at 750 °C in a vacuum environment for 0.5 hours

*Experimental results*

Johanson's model was used to simulate the performance for DPR, and a purpose-built rolling mill used to verify this performance. A summary of the results is listed here:

1. Maximum relative density achieved through DPR:

    a. Stainless steel: 82%

    b. Titanium: 85%

2. The thickness of the green strip was always greater than the roll gap

3. Decreasing the roll gap increased the relative density of the green strip

4. Increasing the powder feeding rate from the hopper increased the relative density of the final product

5. Increasing the rolling speed increased the width of the final product

6. The Johanson model provided a reasonable prediction of nip angle and pressure distribution for a gravity-fed vertical rolling compaction process

7. Titanium green strip with relative density of 85% was vacuum sintered at 1200°C for 2 hours, resulting in an increase in relative density of 7%. Subsequent cold rolling and recrystallisation annealing provided a further increase in density, with the mechanical properties of the final product being comparable to grade 2 wrought titanium

*Discussion*

Zhang's research provides a good basis for the setup of parameters for a direct powder rolling mill. Parametrically speaking, the aims for the mill design should be as follows:

1. The roll gap should be as small as possible in order to produce a high relative density strip (limitation: required strip thickness)

2. The powder should be fed as quickly as possible into the rolls in order to produce a high relative density strip (limitation: powdered material loss)

3. The rolling speed should be as high as possible to control the width of the product (limitation: porosity at very high rolling speeds)

The optimisation of these parameters was considered during the mill testing as discussed in Chapter 6.

## 2.4. Spark Plasma Sintering

### 2.4.1. Overview

Spark Plasma Sintering (SPS) is a rapid sintering technique used to consolidate metal or ceramic powders into a sintered compact. In general, this technique requires the simultaneous application of mechanical pressure and high-intensity pulsed direct electrical current to the powder, resulting in rapid densification.

The advantages of SPS over conventional sintering methods, provided the process parameters are carefully controlled, include that [8] [9] [11] [12]:

1. Very high rates of heating are possible with this process

2. Full densification of the compact can be achieved

    a. At a low sintering temperature, and

    b. In a short holding time at this temperature

3. Subsequent grain growth can be well controlled due to the low sintering temperature

4. Superior mechanical properties can be achieved with this process

It is believed that the efficacy of SPS is achieved through the following mechanisms:

5. Internal and external heating [8] [11] of the powder – the high energy pulse flows through the powder (internal heating of powder) as well as heating the die in which the powder is placed (external heating of powder). This heating of the die is considered to be very important as it allows the die to act as a heating element.

6. Generation of spark discharges across the powder particles, which results in:

    a. Cleaning of the particle surfaces from adsorbed species [11]

    b. Breakdown of the oxide layer on the particles' surfaces [42]

7. Enhancement of the subsequent grain boundary diffusion and migration [11]

8. Generation of a plasma due to the microscopic electrical discharges in the voids surrounding the particles [43]. This mechanism results in accelerated transfer of material and consequently rapid densification. However, to date there is no proof of actual formation of plasma in the material being sintered.

The internal heating referred to above is achieved in part through a mechanism called Joule heating or resistive heating. The equation governing the heat generated by this process is given below, where Q is the generated heat in Joules, I is the applied current in Amps, t is the time over which this current is applied in seconds, and R is the resistance of the material being heated in Ohms:

*Equation 10: Heat generated by current flowing through a resistor [44]*

$$Q = I^2 \times R \times t$$

When determining the temperature that can be achieved through resistive heating, the equation below is used, where $C_v$ and m are the specific heat in J/(kg.K) and mass in kg respectively of the material being heated, and $\Delta T$ is the change in temperature of the material.

*Equation 11: Temperature change induced by heat generation [44]*

$$\Delta T = \frac{Q}{Cv \times m}$$

Combining the two equations above, we get the equation below.

*Equation 12: Temperature change induced by current flowing through a resistor*

$$\Delta T = \frac{I^2 \times R \times t}{Cv \times m}$$

From this equation it is noted that the parameters which can easily be controlled to enable achievement of the desired sintering temperature are

1. The current flowing through the compact, and

2. The time over which this current is allowed to flow

It should be noted that the above equation gives an indication of only the bulk temperature increase of the material. A significant temperature change also occurs at the contact points of the powder particles, due to the small surface area at these points of contact, across which the current must travel. This phenomenon contributes significantly to the efficacy of the SPS mechanism.

The speed of the SPS process results in short holding times required at the sintering temperature, which allows less time for grain coarsening. In this way, a fine grain structure may be achieved through careful process control.

In the development of a suitable technique to provide economical and efficient sintering through electric current, certain published works were of particular interest to the author. Each of these works provided guidance with respect to a particular aspect SPS process development. These included, on a very basic level:

9. Existing techniques for successful consolidation, including the effect of AC vs DC supply, and the mechanism of heating of the compact

10. The role of electrical conductivity of surrounding equipment on the process

11. The effect of varying input parameters on the mechanical properties of the compact

It is believed that for titanium, sintering can be induced at temperatures as low as 700°C [20] [45].

### 2.4.2. Review of SPS Techniques: Orru et al [9]

*Importance of research*

In 2009, Orru et al published a review of over one thousand sources which referenced the use of electric current for the consolidation of materials. In it, the authors classify these consolidation techniques into two broad categories, namely electric discharge sintering (EDS) and resistance sintering (RS). EDS utilises high voltage, high current pulses from capacitor banks to form compacts over very short periods of time. These compacts exhibit levels of high porosity; they thus require further processing, or must be used in applications where this porosity is acceptable or advantageous. EDS techniques will not be focussed on in much detail for the purpose of this study. RS techniques are of far greater interest for our application, and involve the use of a low voltage, high current supply over a longer period of time to produce compacts which require little, if any, further processing. The findings of the comprehensive study conducted which pertain to our research are summarised in this sub-section.

*Current supply waveforms*

Most of the literature available on the use of electrical resistance for sintering refers to the power supply for the sintering process as being pulsed DC. The review depicts the following breakdown of current waveforms utilised for resistance sintering, as shown in Figure 16.
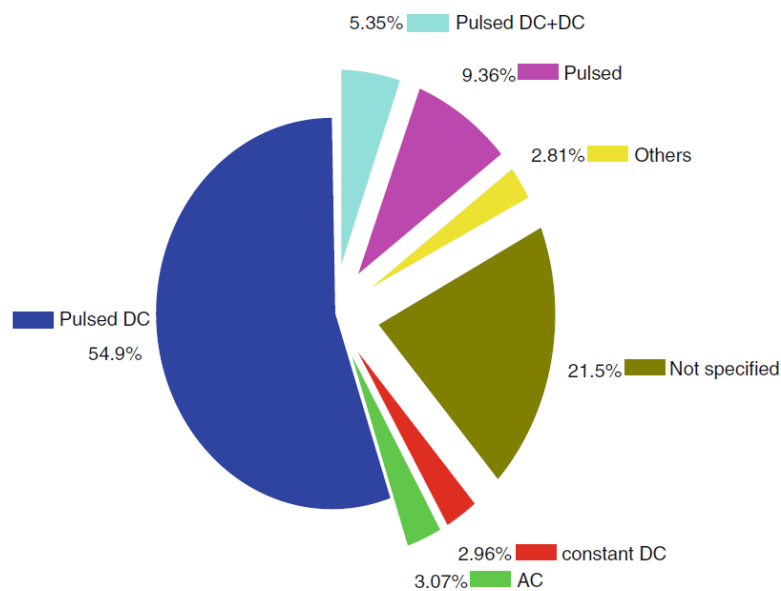


*Figure 16: Current waveforms applied for resistance sintering processes [9]*

Oftentimes, the available literature does not fully specify the apparatus or electric parameters used for the RS process. This creates uncertainty as to the exact waveforms used for different applications, and their effect on the properties of the sintered product. However, it is clear that a successful SPS process may be realised with either AC or DC, with careful parametric control. This allows for both a large degree of flexibility in the design of SPS circuit for this project, and scope for further research which specifically explores the effect of varying waveforms on the resultant compact.

Typical waveforms which may be used to achieve resistive sintering are shown in Figure 17.
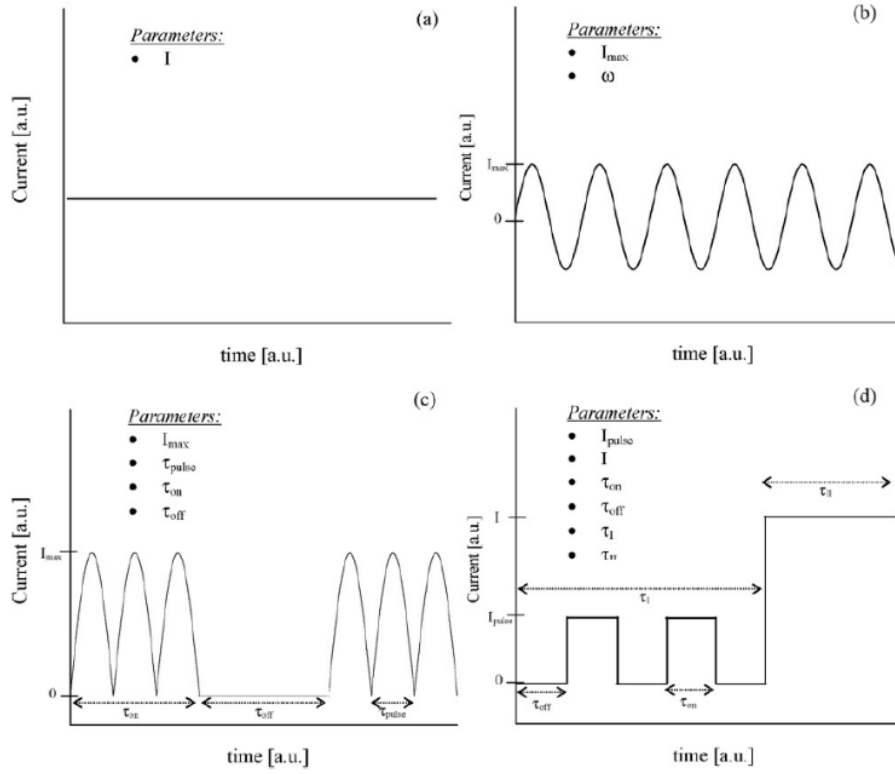


*Figure 17: Typical electric current waveforms applied in the resistive sintering processes: (a) constant DC; (b) AC; (c) pulsed DC; (d) pulsed DC + DC [9]*

For equivalent heating to a compact, in terms of power supplied to the circuit, the values for AC (RMS) and DC should be the same. However, in their description of the heating mechanism of SPS, an additional heating benefit is proposed for the use of AC over DC. This additional heating is related to the skin effect [46], which results in uneven distribution of current through a conductor, with higher current at the surface of the due to the electromagnetic induction. They also indicate that the same benefit can be achieved through the use of a pulsed DC supply, due to a square waveform being equivalent to a series of sinusoidal waveforms. An example of this can be seen in Figure 18.
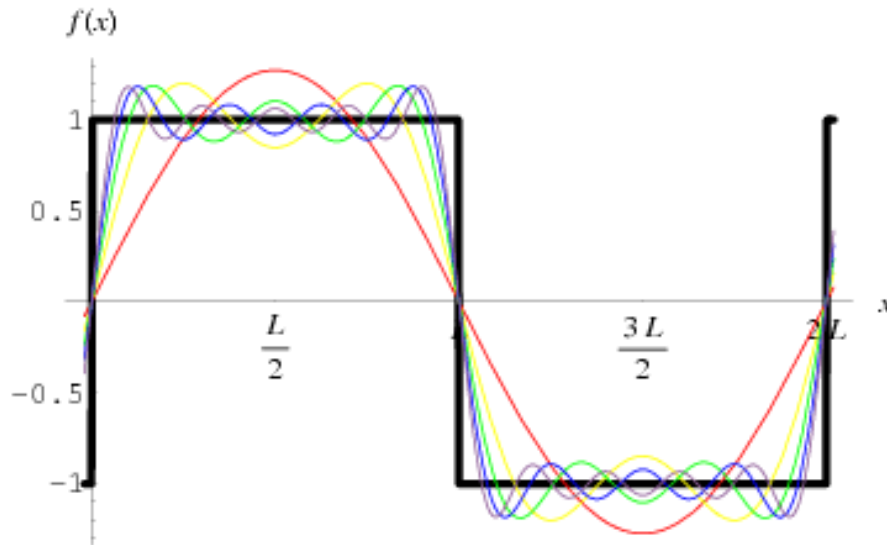


*Figure 18: Fourier series: a square wave and its sinusoidal constituents [47]*

*Historical developments*

The earliest reported use of electric current for sintering of powders to form compacts was in 1922 [48], while the earliest reported combined usage of electric current and mechanical pressure for sintering of metals was in 1932 [49]. This process reportedly took minutes to produce a fully dense compact.

In 1933 [50], a process which modified this design was reported to take a second or less for complete densification, due to the application of pulsed DC followed by AC. It was reported that a high voltage discharge was necessary at the onset of the sintering process due to the high initial resistance of the powdered materials being sintered. It was also claimed that the use of a high-voltage electrical discharge reduces the load resistance and thus permits the flow of current when a subsequent low voltage alternating current is used, allowing the desired sintering temperature to be reached.

In 1944 [51], it was proposed that the high current density used during resistance sintering allows high temperatures at the contact points of the particles being sintered. The bulk of the material remains relatively cold, but becomes sufficiently plastic to allow elimination of porosity with the application of moderate pressures.

In 1945 [52], the idea was reinforced that pulsating current is preferable to continuous current, in particular due to the ability to heat the contact points of the powder particles to sintering temperature while keeping the rest of the compact and the surrounding equipment cold.

In 1961, [53] experimentation was conducted with a method of RS that applied the electric current in a different orientation to the mechanical pressure. Low voltage (1 – 5V) and high amperage (1 – 10kA) AC or DC was applied for 1-52 minutes, depending on the desired output.

Between 1965 [29] and 1966 [30] , it was claimed that the mechanism of critical importance in welding metal particles together was the stripping of the contact surfaces of the particles from oxides and other contaminants in an inert environment. The stripping of the contact surface exposes a metal surface with a higher energy level than that of the rest of the particle – this surface then combines with other available surfaces to reduce the surface energy to the same level as the internal energy, forming a weld between the particles. The oxide layer is believed to be important as an insulator between the particles, prior to a spark being discharged across the particles. This is analogous to a dielectric material being used in a capacitor. The resulting heat and pressure from the spark are reported to disintegrate the surface contaminants and allow for particle-to-particle bridging. A coherent mass is formed if mechanical pressure is applied while the bridged particles are still in a plastically deformable state. Spark discharges between the particles are thought to last 1 –2s. The rest of the sintering time is used in resistance heating of the material to below its melting point to achieve additional particle binding and densification of the mass. An applied mechanical pressure provides final densification, with the entire process taking 12 – 15s and the relative density ranging from 65 – 98%. The parameters requiring control are the spark energy, duration and frequency, the particle size, the resistive heating current and temperature, and the mechanical pressure. It was also reported that due to the sintering process being so rapid, no controlled atmosphere was required. This speculation on the mechanism of the process was not backed up by experimental evidence.

In 1966 [31], a system was patented which supplied DC and AC simultaneously, together with a relatively low pressure of 10MPa. The inventor claimed that densification could be achieved in a matter of a seconds. However, he claimed in a different patent later that year [54] that the method was only suitable for producing high porosity or low-density compacts. He also claimed advantageous results on the compact density when the current supply was either reduced to a low level or cut off one or more times in the course of the sintering process. He then further patented a process in 1970 [32] which used applied voltage and current in the order of magnitude of 10V and 1000A respectively. In this patent, he reiterated the role of high temperature and reducing atmosphere in destroying the film around the particles, allowing particle binding to occur.

The discharge is also believed to urge the newly-exposed particle surfaces together by creating a shock wave. He claimed in this patent that it was possible to achieve spark sintering through use of DC or, with less efficiency, AC. He also claimed, however, that it was advantageous to promote fusion by the application of current surges or pulses superimposed on the DC component used for resistance heating. It was reported in 1969 [55] by those utilising these methods that spark sintering appeared effective for consolidation of powders with a high creep resistance at elevated temperatures. This due to the ability to control process parameters such that the sintering temperature remains between the narrow band of plasticity and melting.

In 1971 [56], it was proposed that the spark sintering mechanism occurs in two stages. The first stage uses a low mechanical pressure and a combination of AC and DC to create electric spark discharges in the powders and hence the initial bonds between particles. The second stage consists purely of resistance heating of the compact under increased mechanical pressure.

*Application to titanium*

Research was conducted between 1977 and 1979 [57] [58] [59] [60] on titanium and titanium alloys, to investigate the effect of processing conditions on the final product during the resistive sintering process. During this research, it was found that the electrical sintering is related to the current level, applied pressure, particle size, powder pre-treatment and the presence of alloying metal powders.

Titanium compacts of 96% relative density have been produced within 2s, with the microstructural and mechanical properties (including yield stress and ultimate tensile stress) of these compacts found to favourably compare to analogous products obtained through alternative PM techniques [61].

*Discussion*

From this extremely relevant SPS review paper, various pertinent information has been extracted, such as the different waveforms that may be used for successful SPS processing; the historical development of the SPS process (including details on how the electrical and mechanical parameters influence the final product); and the techniques for applying SPS to different materials, specifically titanium. This information will be used to guide the SPS design for the mill. However, very few of the published works explored in this review paper deal specifically with the effect of the current or voltage waveform on the compact. There is thus flexibility in the design of the SPS system for this mill, as well as room for further study on this topic, where focus should be directed on the effect of current and voltage waveforms on the final product.

### 2.4.3. Effect of Electrical Conductivity on Process Efficiency: Guillon et al [62]

In 2014, Guillon et al published a paper on the technological advancements of Spark Plasma Sintering (SPS), which they considered more correctly termed as Field-Assisted Sintering Technology (FAST). One of the aspects of the process explored here is the electrical conductivity of the compact and the compacting equipment. A classical SPS system consists of a punch and die setup containing a sample to which a pulsed current is applied. In this setup, the die surrounding the sample, as well as the sample itself, can be either electrically conductive or non-conductive, as shown in Figures 19, 20 and 21.
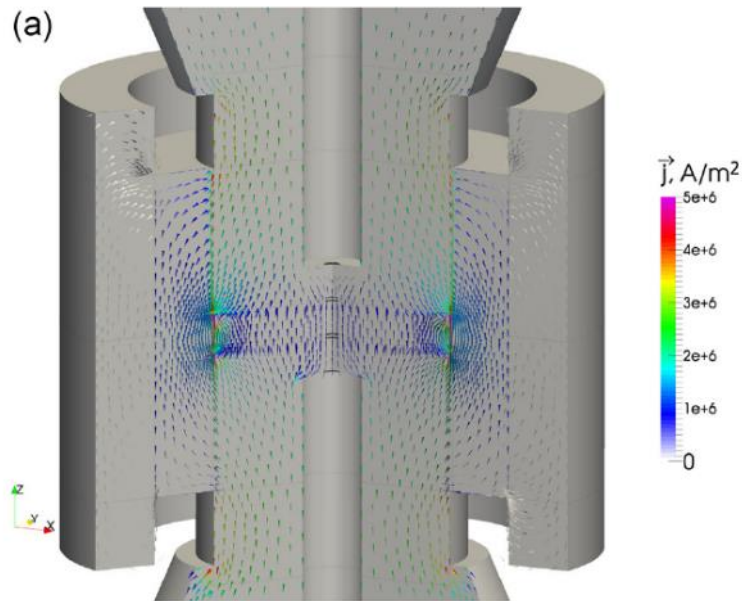


*Figure 19: Conductive die, conductive sample [62]*
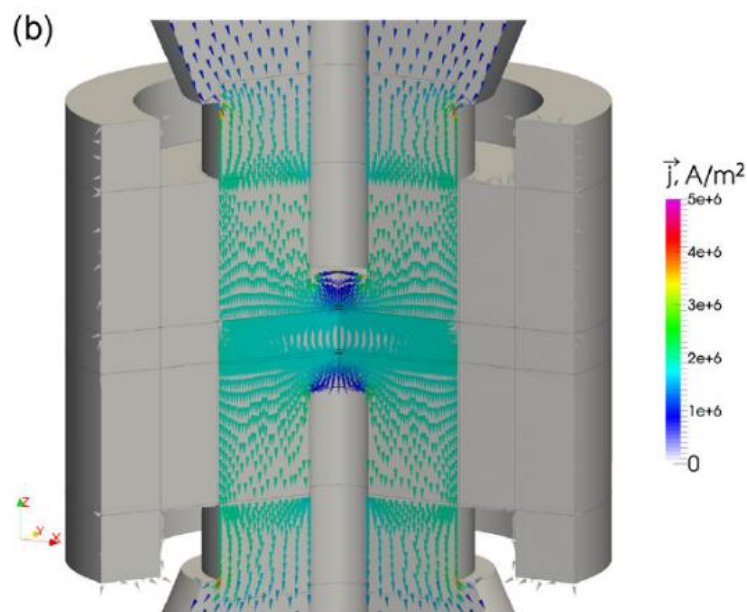


*Figure 20: Non-conductive die, conductive sample [62]*

32
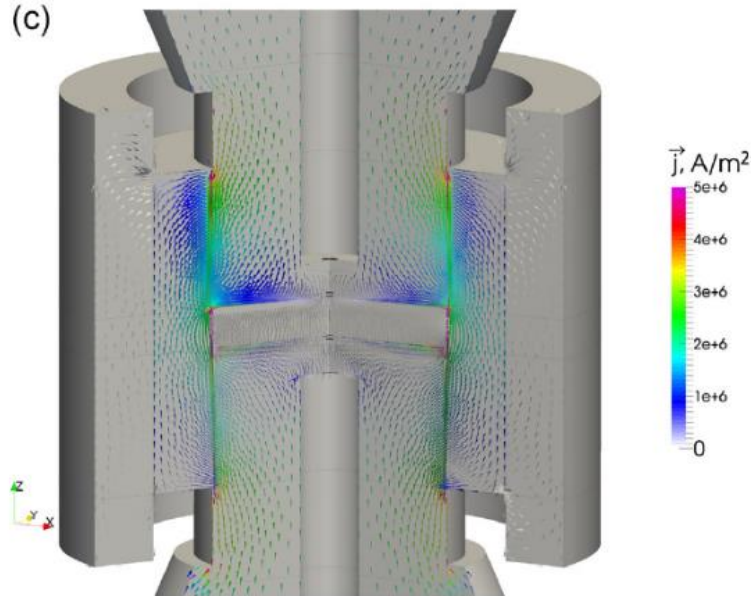
*Figure 21: Conductive die, non-conductive sample [62]*

In cases (a) and (b), the powder itself is electrically conductive. As can be expected, using a non-conductive material for the die, as in (b), results in better current density through the bulk of the powder (compared to (a), which uses an electrically non-conductive die), as the powder then becomes the only electrical pathway through which the current can flow. However, the advantage of (a) over (b) is that there is both internal and external heating of the sample when current is allowed to flow through both the sample and the die. Case (c) is that of an electrically non-conductive sample, surrounded by a conductive die. Sintering in this case is purely external through heating from the punch and die, as current does not flow through the sample.

A historic problem encountered in the SPS setup is the distribution of current in the compact, leading to uneven heating and thus deviation in mechanical properties throughout the sample at best, and unwanted melting of the bulk sample and damage to the equipment at worst. This uneven current distribution can be seen in the figures above [62].

The researchers quote typical electrical values of less than 10V, and 1 – 10kA, for the power supply to the compact being sintered, citing good conductivity of the tooling for the high currents (and thus efficient Joule heating) possible with low voltages. They also quote figures of 50 – 250kN applied mechanical pressure to the compact for enhancement of densification.

It may be seen from this paper that the level of electrical conductivity of both the sample and the tooling, and thus the current pathway during the SPS process, can have a significant effect on the sintered compact. This was borne in mind during the process of designing the SPS system for the mill.

### 2.4.4. Parametric Study of SPS: Shen et al [11]

*Overview*

In 2002, Shen et al conducted a comprehensive study on the effect of varying SPS process parameters on the mechanical properties of a sintered compact formed using pulsed DC on alumina powder ($Al_2O_3$). A schematic of the apparatus used is depicted in Figure 22.
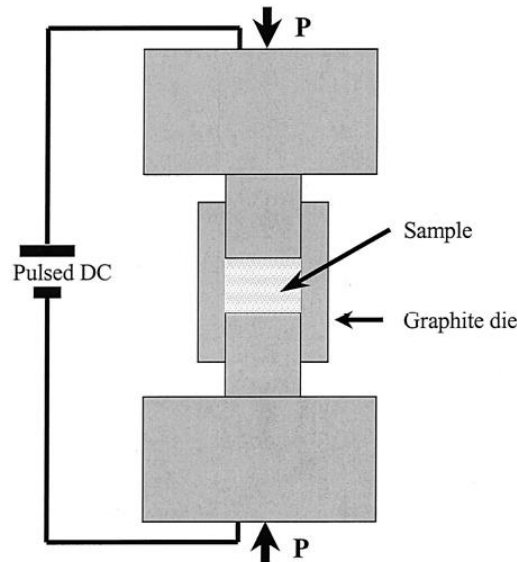


*Figure 22: Schematic of SPS apparatus [11]*

This study will be of interest when conducting parametric testing of the SPS system on the mill. Their findings are summarised below.

*Temperature effect*

During the experimentation, a critical sintering temperature became apparent; the behaviour of the material being sintered varied depending on whether the material was sintered at above or below this critical temperature. The critical temperature was believed to be dependent on the properties of the powder, the density of the pre-sintered compact, and the applied pressure. The results of varying temperature on the density and grain size of the sintered compact are shown in Figure 23.
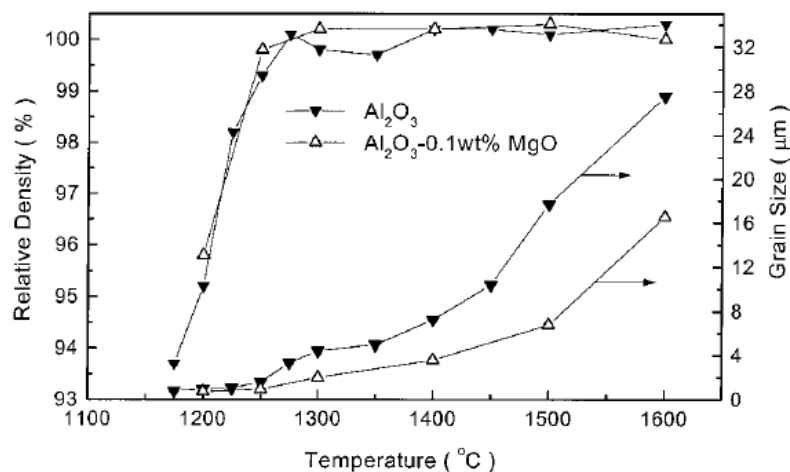


*Figure 23: Relative density and grain size versus sintering temperature [11]*

34

As per the figure above, at temperatures below the critical temperature, higher sintering temperature resulted in:

1. Higher relative density of the sintered compact

At or above the critical temperature, higher sintering temperature resulted in:

1. No change to the relative density as all compacts produced above this temperature were fully dense

2. Larger grain sizes of the sintered compact (i.e. coarser grains were formed at a higher temperature)

3. Lower hardness of the sintered compact

*Time effect*

The results of varying holding time at the sintering temperature on grain size and grain growth rate, for two different sintering temperatures (one above the critical temperature and one below), are shown in Figure 24.
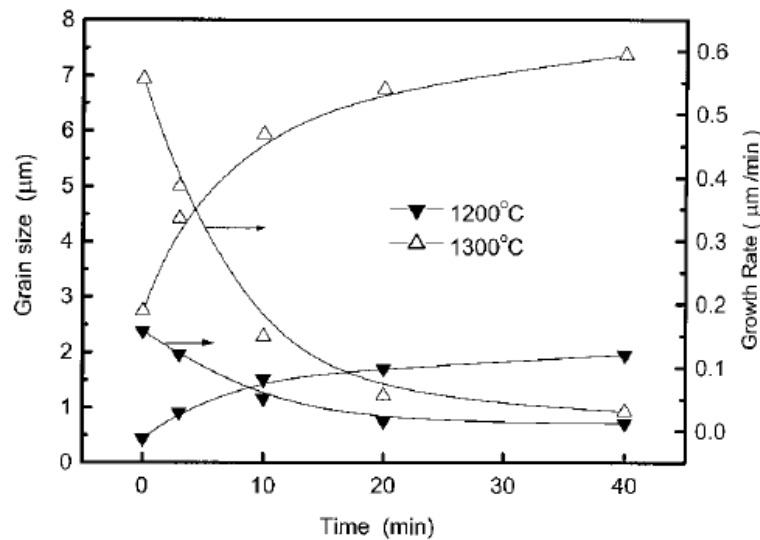


*Figure 24: Grain size and grain growth rate versus holding time, at different sintering temperatures [11]*

The longer the compact is held at the sintering temperature, the larger the grain sizes formed in the compact. The grain growth rate is high at the start of the sintering process, then gradually decreases (i.e. most grain growth occurs at the initial part of the sintering).

*Applied pressure effect*

The results of varying sintering temperature on relative density, for two different compaction pressures, are shown in Figure 25.
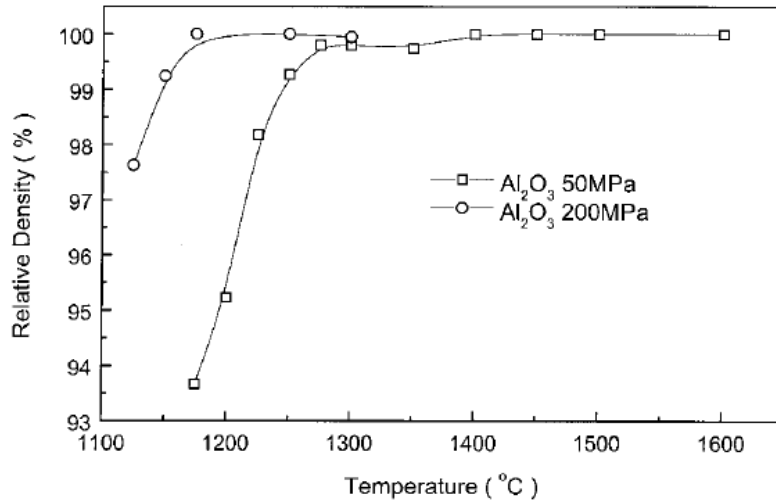


*Figure 25: Relative density versus sintering temperature, at different compaction pressures [11]*

At higher applied pressures, full densification was achieved at lower sintering temperatures.

In order to achieve a finer grain structure, it is better to initiate the applied pressure only once the final sintering temperature has been reached, rather than applying the pressure for the duration of the sintering cycle (including heating up).

The enhanced degree of densification at higher applied pressures is most likely due to a higher packing density of the particles at higher pressures.

*Heating rate effect*

The results of varying heating rate on relative density and grain size, for two different sintering temperatures (both above the critical temperature), are shown in Figure 26.
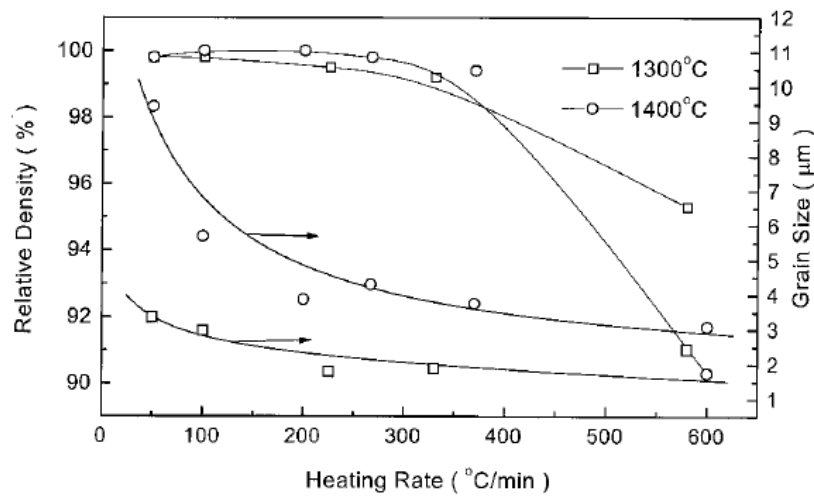


*Figure 26: Relative density and grain size versus heating rate, at different sintering temperatures [11]*

Higher heating rates resulted in finer grain structures. This is more apparent at higher sintering temperatures. However, if the heating rate was too high, the sintered samples started to exhibit porosity.

*Pulse-sequence effect*

The results of varying the pulse-sequence on the densification rate, for different sintering temperatures, are shown in Figure 27.
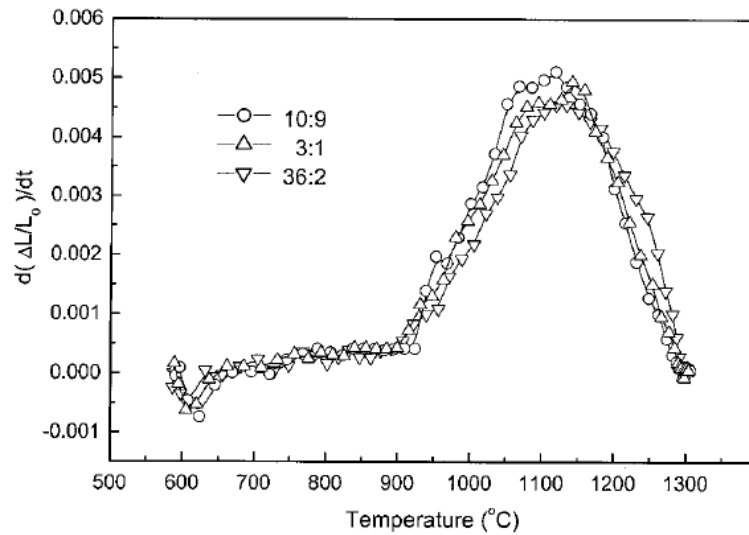


*Figure 27: Densification rate versus sintering temperature, for different pulse-sequences [11]*

Although the pulse-sequence did not affect the final density of the samples, it did affect the densification rate. For higher pulse on/off ratios, the maximum densification rate:

1. Decreased, and

2. Occurred at a higher sintering temperature

However, these effects were not as obvious as those discussed previously.

*Discussion*

A critical sintering temperature is apparent, above which relative densities cannot be increased, but the grain growth is undesirable. It is thus recommended to aim for as close to this critical temperature as possible without exceeding it. Grain size also increases with longer holding times at the sintering temperature, but this effect is less marked below the critical temperature. Maximum shrinkage (densification) could be achieved at lower temperatures through increasing the heating rate or increasing the applied compaction pressure.

The electric discharge effect in the voids between the particles can only be active in the initial sintering phase, which may account for the rapid densification at the start of the process. Once the pores between the particles are closed, grain boundary diffusion and grain boundary migration determine the rate of densification.

MgO was successfully used as a grain growth inhibitor, as samples containing this compound exhibited smaller grains than those samples without the compound after sintering. This can be seen from the graphs of grain size versus temperature.

### 2.4.5. SPS Literature Discussion

Spark Plasma Sintering is a technology that offers many benefits over the conventional sintering process. Additionally, the spark plasma sintering process has successfully been used on titanium [6] [9] [63] [64] [65]. It is therefore the intention of this project to integrate SPS technology into the DPR process as the method of sintering.

It is proposed that in order to achieve a fully dense compact with good mechanical properties, the process parameters be controlled as follows:

1. The sintering temperature should be high enough that the compact can reach full density, but not so high that the grains become coarse (i.e. adherence to the critical temperature).

2. Similarly, the holding time should be long enough that the compact can reach full density, but not so long that grain coarsening is allowed to occur.

3. Pressure should be applied to the compact once the sintering temperature is reached, if possible, and should be high enough in magnitude to allow for sintering to full density at a temperature low enough to avoid grain coarsening.

4. The heating rate should be as high as possible without creating porosity in the compact.

5. The pulse on/off ratio does not appear to have a considerable effect on the properties of the sintered compact. It would be sufficient to ensure that a pulsed direct current (regardless of the pulse on/off ratio), or alternating current, is applied to the compact. However, if using pulsed direct current, there may be a small benefit to keeping the pulse on/off ratio as low as possible (to allow higher maximum densification rates at lower temperatures).

The cheek plates of the rolling mill are analogous to the die in a conventional SPS setup. For future observation of the effects of current pathways on the quality of the sintered compact, allowance was made for two different configurations as described below:

1. The cheek plates being electrically insulative, such that the only pathway for the current to follow is through the sample itself, in order to achieve a high current density through the material being sintered

2. The cheek plates being electrically conductive, such that the current is allowed to flow through both the sample and the cheek plates, in order to achieve both internal and external heating of the sample.

# 3. Experimental Process

This chapter will detail the experimental process followed for determining certain powder properties required for the mill design. The experimental process will include the experimental methodology, the experimental results, and a brief experimental discussion.

In the course of this chapter, the properties of the powder required as the parameters for determining the behaviour of the mill are established. This behaviour is determined using the Johanson method described in Section 2.3.2, via the MATLAB model as described in Section 4.3.

## 3.1. Experimental Methodology

This section details the methodology used in preparing a range of suitable powders for the SPS-DPR mill and determining their frictional and compressibility characteristics.

As reviewed in Section 2.3.2., according to Johanson's theory, the powder characteristics and mill dimensions directly affect the pressure applied to the powder and thus the density of the compact produced. This knowledge was used in the selection of an ideal powder for production of a compact with a particular density and thickness.

A range of powders was prepared by separating different particle size ranges using sieves. The prepared powders will then be tested to determine their characteristics. Based on the theory of the Johanson model, an ideal powder will be selected based on the expected compact properties for each of the powders.

### 3.1.1. Raw Powder and Sieving Equipment

There were two raw powders available for testing:

1. Powder 1: 100 mesh HDH titanium (< 150 micron)

2. Powder 2: 325 mesh HDH titanium (< 45 micron)

The specifications received from the supplier of these powders are shown in Table 1.

*Table 1: Titanium powder specifications*

| Powder | Chemical Composition (%) | | | | | | | | | | Maximum Particle Size | Apparent Density | Flow Rate |
| --- | --- | --- | --- | --- | --- | --- | --- | --- | --- | --- | --- | --- | --- |
| | Ti | H | O | N | Fe | C | Si | Cl | Mn | Mg | | | |
| HDH-Ti 100 mesh (<150 μm) | Balance (99.62) | 0.022 | 0.26 | 0.021 | 0.013 | 0.01 | 0.012 | 0.02 | 0.01 | 0.01 | 150 μm | 1950kg/m$^3$ | 1.4g/s |
| HDH-Ti 325 mesh (<45 μm) | Balance (99.57) | 0.026 | 0.31 | 0.023 | 0.011 | 0.01 | 0.011 | 0.02 | 0.01 | 0.01 | 45 μm | 1500kg/m$^3$ | 0.9g/s |

There were also three sieves available for use:

1. Sieve 1: -105 μm

2. Sieve 2: -75 μm

3. Sieve 3: -45 μm

### 3.1.2. Powder Preparation

Based on the powder and sieving equipment available, titanium powder with the following particle size ranges was used for preliminary testing:

1. <150 μm (as-received)

2. 105-150 μm (sieved)

3. 75-105 μm (sieved)

4. 45-75 μm (sieved)

5. <45 μm (sieved)

6. <45 μm (as-received)

7. A combination of 75% by mass 105-150 μm (sieved) and 25% by mass <45 μm (sieved)

It was expected that improved compact densities may be achieved by removal of the "medium" powder sizes, and use of a combination of the "large" and "small" particle sizes (as an adaptation of the powder preparation process used by Moxson and Duz [15]). This was the reason for the preparation of powder number (7) above.

### 3.1.3. Powder Testing

The following testing, to be performed at the UKZN Civil Engineering Department, was required to determine the frictional and compressibility characteristics of the powder:

1. Uniaxial compression test – To determine the compressibility, K

2. Internal shear test – To determine the equivalent angle of internal friction, δ

3. Wall shear test – To determine the angle of wall friction, ϕ'

As can be seen from the description of the powder preparation, there are different powders available on which we may perform our testing. However, to run a full range of tests on all these powders would be impractical. Preliminary testing was thus conducted to determine the preferred powders with respect to the density that may be achieved at a specified pressure. This took the form of a uniaxial compression test on a single sample of each of the seven prepared powders, at a single applied force, with the density of each compact recorded. The three powders exhibiting the highest densities were used for further testing as described below.

### 3.1.4. Manufactured Components

*Powder compression die*

A die set was manufactured for the purpose of housing the powder during the uniaxial compression testing. Originally, the machined die set consisted of two pieces, namely the bottom die and the top die. This two-piece die set was found to have a design flaw in that the compact could not easily be removed after it had been formed, as it became lodged in the bottom die. The die set, as well as the compact lodged therein, is shown in Figure 28.

*Figure 28: Two-piece die-set manufactured for uniaxial compression testing*

The design was thus modified to a three-piece die set, which allowed for easy removal of the formed compact. This essentially entailed a separation of the blind bottom die into a through bottom die and a stopper.

Further, the bottom of the die required slight machining refinement to prevent powder leakage after the modification as it was found to not sit flush with the centre piece of the die. The compact formed in the three-piece die set before and after the refinement can be seen in Figures 29 and 30.



*Figure 29: Powder leakage in the three-piece die-set due to poor seating of the bottom stopper*



*Figure 30: Refined three-piece die-set, without powder leakage*

*Shear plate*

For the shear test used to determine wall friction angle, a mild steel plate with a clean surface resembling that of the rolling surfaces of the mill was manufactured. This component was placed in the shearing device, flush with the bottom half of the shear box, to enable the powder in the top half of the shear box to shear against it. The position of this plate in the shear box apparatus is shown in Figure 31.
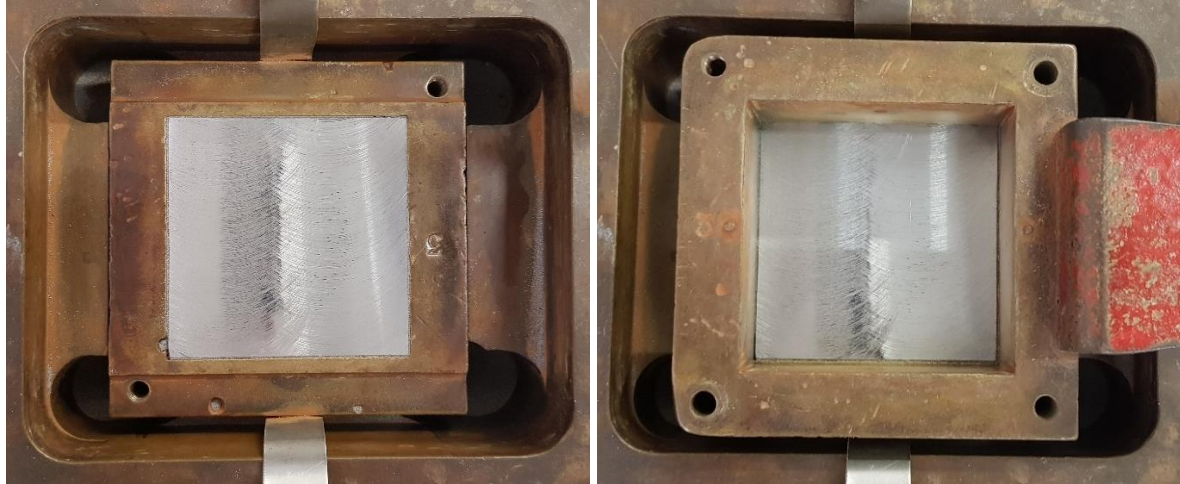


*Figure 31: Position of shear plate, wall shear test*

### 3.1.5. Uniaxial Compression Test

*Background*

The compressibility factor K describes the relationship between the pressure applied to a powder and the density of the compact produced. This value can be determined experimentally via the uniaxial compression test. A known force is applied over a constant cross-sectional area of powder, and the density of the compact produced during compression is then measured. Using a logarithmic scale and plotting the values of applied pressure on the x-axis and compact density on the y-axis for different compressive forces, the K value can be obtained directly as the inverse gradient of the resulting straight-line graph.

*Experimental procedure*

The uniaxial compression test was carried out on three different powders, as selected during the preliminary testing. Each powder was compacted at five different pressures, with the density of each compact subsequently being measured by measuring its mass and volume. A 25mm three-piece die set was manufactured for the purpose of holding the powder during compaction. The hydraulic press available at the UKZN Civil Engineering Laboratory, which was used for the compression testing, has an applied force range of 0 – 520kN.

The step-by-step procedure followed for the uniaxial compression test was as follows:

1. Measure a 5g sample of powder into a glass container

2. Seat the stopper into the bottom die

3. Pour the powder into the bottom die, and seat the top die into the bottom die

4. Insert the die set containing the powder onto the bottom plunger of the press

5. Compress the powder using the top plunger, until the desired applied force is reached

6. Remove the applied force by raising the top plunger

7. Record the maximum force applied by the press

8. Remove the formed compact from the die set, and

    a. Measure its thickness

    b. Measure its mass

    c. Use (a) and (b) above to calculate the sample density

This procedure was first followed for a single load point for all seven powders prepared, as a preliminary selection of the three most suitable powders (based on the highest densities observed), to be used in subsequent testing.

Each of the three selected powders was then tested using the procedure above at five different loads, to determine the compressibility of the powder samples. For each powder, the experiment was performed three times at each load; the average of the three measurements was used to determine the compressibility of each powder.

Based on the compressibility as determined during this test, a single powder was selected for the shear testing (internal shear and wall shear).

*Density determination*

Since it was expected that a simple disc shape would be produced during the uniaxial testing, the density of these compacted parts was determined through simple measurement of the mass and dimensions of the part, and application of the equation below. Note that $\rho$ is the compact density, m is the measured mass, d is the compact diameter, and t is the measured thickness.

*Equation 13: Calculation of uniaxially compressed sample density*

$$\rho = \frac{4m}{\pi d^2 t}$$

This method of using a part's mass and dimensions to calculate its density has been used previously for density determination of direct-rolled titanium strip [66] – this method was thus also used in Chapter 6 for determining the density of the titanium strip rolled through the manufactured DPR mill.

### 3.1.6. Internal Shear Test

*Background*

The internal friction angle δ describes the relationship between the normal stress exerted on a powder and the corresponding shear strength of the powder. This value can be determined experimentally via a shear box test. A known vertical force is applied over a cross-sectional area of powder, and the horizontal force at shear failure is then measured. Plotting the values of normal stress on the x-axis and shear strength on the y-axis for different vertical loads, the δ value can be obtained directly as the angle formed between resulting straight-line graph and the x-axis (equivalent to the arctangent of the gradient of the resulting straight-line graph).

The use of this method to determine the internal friction angle is well established [67]. This is shown graphically in Figure 32.



*Figure 32: Graphical determination of internal shear angle [67]*

*Experimental apparatus*

A schematic of the experimental apparatus used for this testing is shown in Figure 33 [67].
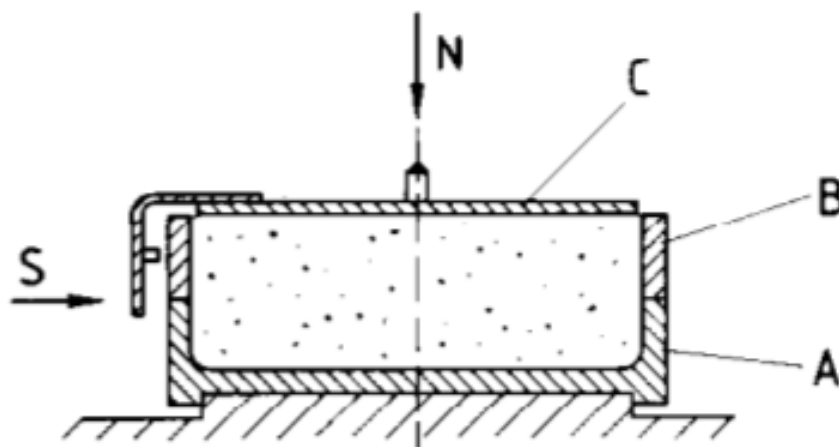


*Figure 33: Shear tester; base (A), ring (B), lid (C) [67]*

In the schematic above, N represents the vertical normal force applied to the lid, and S represents the horizontal shearing force applied to the lid via a bracket. N is a known force (and is thus the independent variable) and S is measured via a load cell (and is thus the dependent variable in this case). The wall shear test apparatus is identical to this, except that the powder in the base is replaced with the wall material for which the wall friction angle is to be determined.

The actual apparatus used for conducting the internal shear testing and wall shear testing is shown in Figure 34.
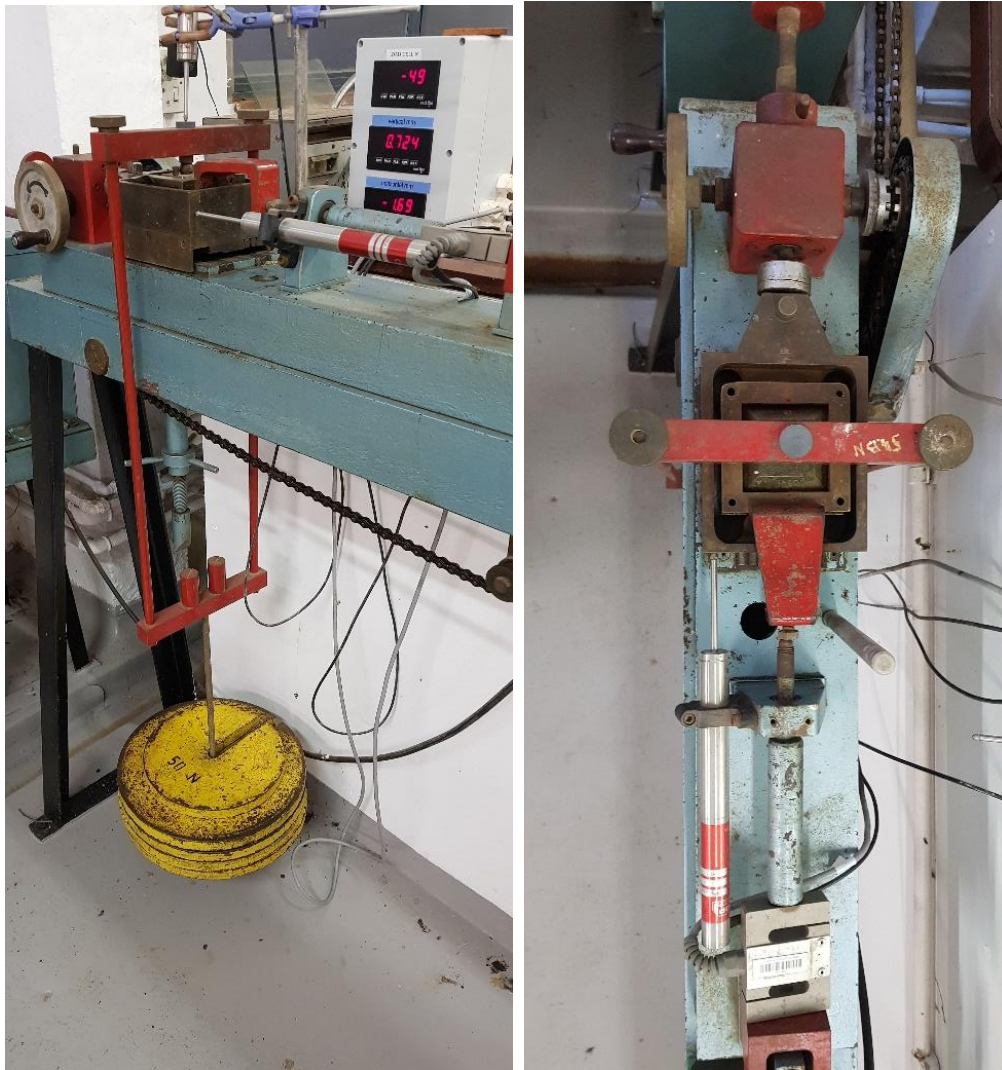


*Figure 34: Experimental apparatus, internal and wall shear testing*

*Experimental procedure*

The shear test to determine the internal friction angle was carried out on the powder selected during the uniaxial compression tests. The powder was subjected to five different normal loads, with the shear strength at failure being recorded for each normal load. A shear box testing apparatus was used to perform these tests.

The step-by-step procedure followed for the internal shear test was as follows:

1. Measure the height and cross section of the shear box

2. Measure out the required mass of the powder sample based on the shear box volume

3. Place the shear box inside the shearing device

4. Stabilize the shear box by affixing the two vertical screws

5. Place the porous stone in the shear box, followed by the powder sample, the second porous stone, and the loading cap

6. Place the hanger onto the loading cap, and ensure correct positioning of the dial gauges

7. Zero the shear force measured by the load cell

8. Zero the vertical and horizontal displacements of the dial gauges

9. Place the vertical load on the hanger

10. Wait for the vertical displacement to stabilise

11. Remove the two stabilising screws and engage the motor clutch

12. Switch the motor on to begin the shearing stage

13. Take readings of the horizontal load every minute until the shear stress peaks and falls, and a plateau is witnessed

The powder selected during the uniaxial compression test was tested using the procedure above, at five different vertical loads, to determine the internal friction angle of the powder samples.

### 3.1.7. Wall Shear Test

*Background*

The wall friction angle ϕ' describes the relationship between the normal stress exerted on a powder and the corresponding shear strength of the powder. This value can be determined experimentally via a shear box test. A known vertical force is applied over a cross-sectional area of powder, and the horizontal force at shear failure is then measured. Plotting the values of normal stress on the x-axis and shear strength on the y-axis for different vertical loads, the ϕ' value can be obtained directly as the angle formed between resulting straight-line graph and the x-axis (equivalent to the arctangent of the gradient of the resulting straight-line graph).

The use of this method to determine the wall friction angle is well established [67]. This is shown graphically in Figure 35.

*Figure 35: Graphical determination of wall shear angle [67]*

*Experimental procedure*

The shear test to determine the wall friction angle was carried out on the powder selected during the uniaxial compression tests. The powder was subjected to five different normal loads, with the shear strength at failure being recorded for each normal load. A shear box testing apparatus was used to perform these tests.

The step-by-step procedure followed for the wall shear test was as follows:

1. Measure the height and cross section of the shear box

2. Measure out the required mass of the powder sample based on the shear box volume (half the amount of powder used for the internal shear test)

3. Place the shear box inside the shearing device

4. Stabilize the shear box by affixing the two vertical screws

5. Place the steel plate in the shear box, followed by the powder sample and the loading cap

6. Place the hanger onto the loading cap, and ensure correct positioning of the dial gauges

7. Zero the shear force measured by the load cell

8. Zero the vertical and horizontal displacements of the dial gauges

9. Place the vertical load on the hanger

10. Wait for the vertical displacement to stabilise

11. Remove the two stabilising screws and engage the motor clutch

12. Switch the motor on to begin the shearing stage

13. Take readings of the horizontal load every minute until the shear stress peaks and falls, and a plateau is witnessed

The powder selected during the uniaxial compression test was tested using the procedure above, at five different vertical loads, to determine the wall friction angle of the powder samples.

## 3.2. Experimental Results

This section will examine the results of the experimentation performed on a range of prepared powders, as described in the experimental methodology section. The results of the preliminary testing, uniaxial compression testing, and shear testing (internal shear and wall shear) will be discussed here.

### 3.2.1. Preliminary Test

Table 2 indicates the number allocated to each of the preliminary tests performed.

*Table 2: Classification of preliminary testing*

| Applied Load | Powder 1 | Powder 2 | Powder 3 | Powder 4 | Powder 5 | Powder 6 | Powder 7 |
|---|---|---|---|---|---|---|---|
| 100kN | Test PT1 | Test PT2 | Test PT3 | Test PT4 | Test PT5 | Test PT6 | Test PT7 |

The results of the preliminary testing on the powder are tabulated in Table 3.

*Table 3: Results of preliminary testing*

| Test Number | Applied Pressure (MPa) | Density (kg/m$^3$) | Relative Density (%) | Indicative Density/ Pressure Ratio |
|---|---|---|---|---|
| PT1 | 203.9 | 2910 | 64.53 | 0.316 |
| PT2 | 205.1 | 3056 | 67.76 | 0.330 |
| PT3 | 204.5 | 2928 | 64.93 | 0.317 |
| PT4 | 204.1 | 2874 | 63.72 | 0.312 |
| PT5 | 204.9 | 3099 | 68.71 | 0.335 |
| PT6 | 204.9 | 2983 | 66.14 | 0.323 |
| PT7 | 204.7 | 3062 | 67.90 | 0.332 |

The compacts formed during the preliminary testing are shown in Figure 36.



*Figure 36: Compacts formed during preliminary testing, PT1 to PT7, left to right*

Due to the performance of the various powders under the applied pressure, the following powders were selected for further testing:

1. Powder 2: 105-150 μm

2. Powder 5: <45 μm

3. Powder 7: 75% of [105-150 μm (Powder 2)] + 25% of [<45 μm (Powder 5)]

These powders exhibited the highest densities on compaction by a single applied pressure (i.e. 100kN). Their compressibility factor, K, was determined during the next set of tests.

### 3.2.2. Uniaxial Compression Test

The uniaxial compression tests were conducted on the three powders selected during the preliminary testing. In order to determine the compressibility of the powders, samples of each powder were compressed at five different pressures, with the density at each pressure being determined thereafter.

Table 4 indicates the number allocated to each of the uniaxial compression tests performed.

*Table 4: Classification of uniaxial compression testing*

| Applied Load | Powder 2 | Powder 5 | Powder 7 |
|---|---|---|---|
| 20kN | Test UCT1 | Test UCT6 | Test UCT11 |
| 40kN | Test UCT2 | Test UCT7 | Test UCT12 |
| 60kN | Test UCT3 | Test UCT8 | Test UCT13 |
| 80kN | Test UCT4 | Test UCT9 | Test UCT14 |
| 100kN | Test UCT5 | Test UCT10 | Test UCT15 |

The results of the uniaxial compression tests are tabulated in Table 5.

*Table 5: Results of uniaxial compression testing*

| Test Number | Force (kN) | Pressure (MPa) | Thickness (mm) | Density (kg/m$^3$) | Relative Density (%) |
|---|---|---|---|---|---|
| UCT1 | 20.4 | 41.6 | 4.55 | 2239 | 49.65 |
| UCT2 | 40.3 | 82.1 | 4.07 | 2503 | 55.50 |
| UCT3 | 60.3 | 122.8 | 3.80 | 2683 | 59.49 |
| UCT4 | 80.5 | 164.0 | 3.60 | 2827 | 62.69 |
| UCT5 | 100.3 | 204.4 | 3.41 | 2990 | 66.30 |
| UCT6 | 20.2 | 41.1 | 4.53 | 2250 | 49.90 |
| UCT7 | 40.3 | 82.2 | 4.06 | 2511 | 55.68 |
| UCT8 | 60.2 | 122.7 | 3.82 | 2669 | 59.18 |
| UCT9 | 80.3 | 163.7 | 3.64 | 2799 | 62.05 |
| UCT10 | 100.1 | 203.9 | 3.45 | 2952 | 65.46 |
| UCT11 | 20.1 | 40.9 | 4.39 | 2318 | 51.41 |
| UCT12 | 40.3 | 82.0 | 4.04 | 2519 | 55.86 |
| UCT13 | 60.2 | 122.6 | 3.76 | 2709 | 60.07 |
| UCT14 | 80.5 | 164.0 | 3.58 | 2848 | 63.15 |
| UCT15 | 100.5 | 204.8 | 3.43 | 2967 | 65.79 |

Three samples were used to generate each data point, i.e. each of the tests (UCT1 – UCT15) was performed three times, with the average of the three results tabulated. The use of multiple samples for each datapoint should result in high result accuracy, and was feasible for this test due to the relatively short time taken to perform each test and the small amount of titanium powder required for each test. The compact density versus the compaction pressure applied to the powder was drawn up for each powder. These graphs are shown in Figures 37, 38 and 39.
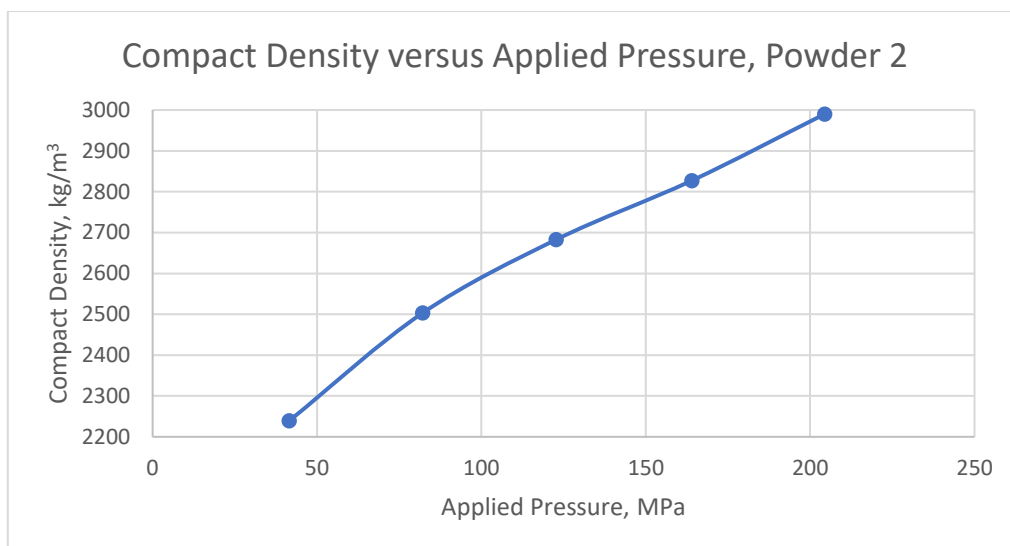
*Figure 37: Compact density versus applied pressure, powder 2*
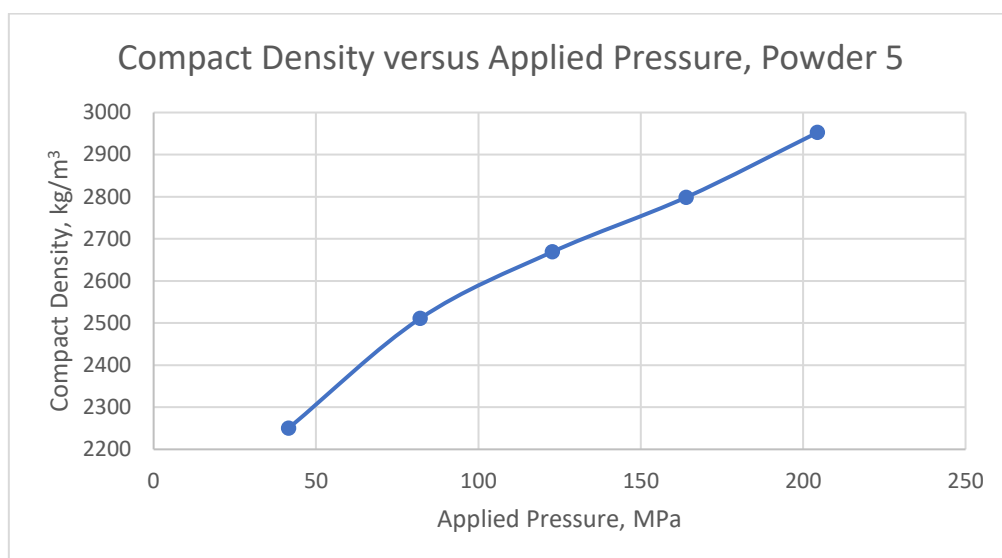


*Figure 38: Compact density versus applied pressure, powder 5*
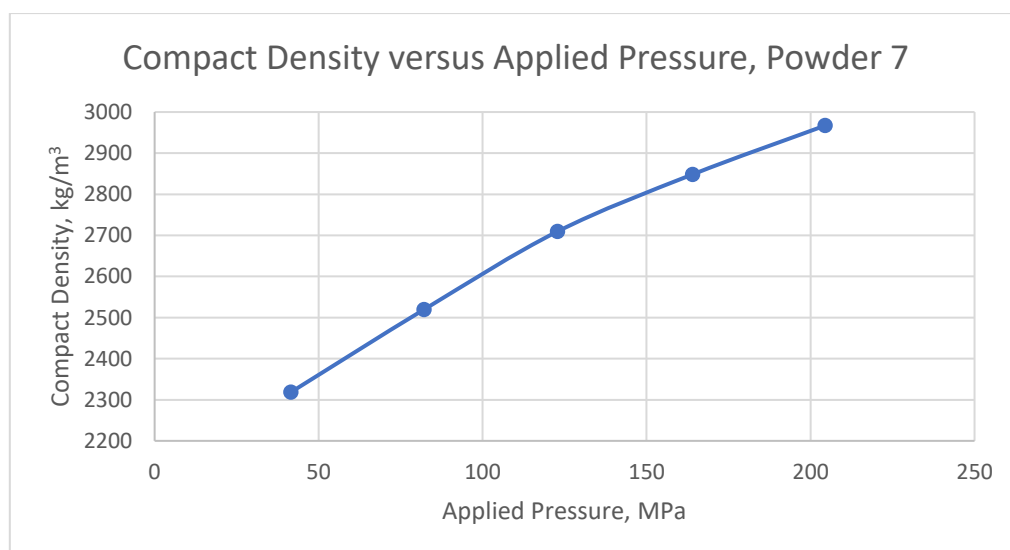


*Figure 39: Compact density versus applied pressure, powder 7*

For the determination of the compressibility of each of the powders, a plot of the natural logarithm of the compact density versus the natural logarithm of the compaction pressure applied to the powder was drawn up for each powder. A linear trendline was then generated for each of the powders. These graphs are shown in Figures 40, 41 and 42.
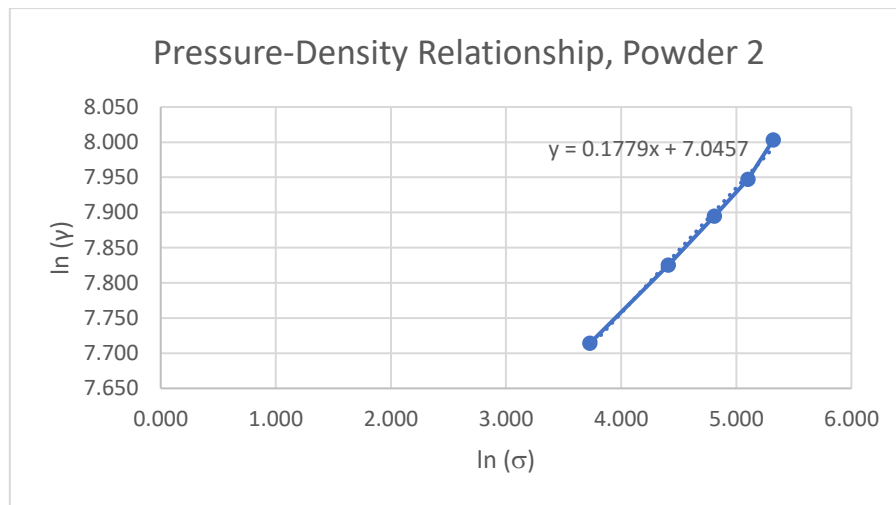


*Figure 40: Determining the compressibility for powder 2*
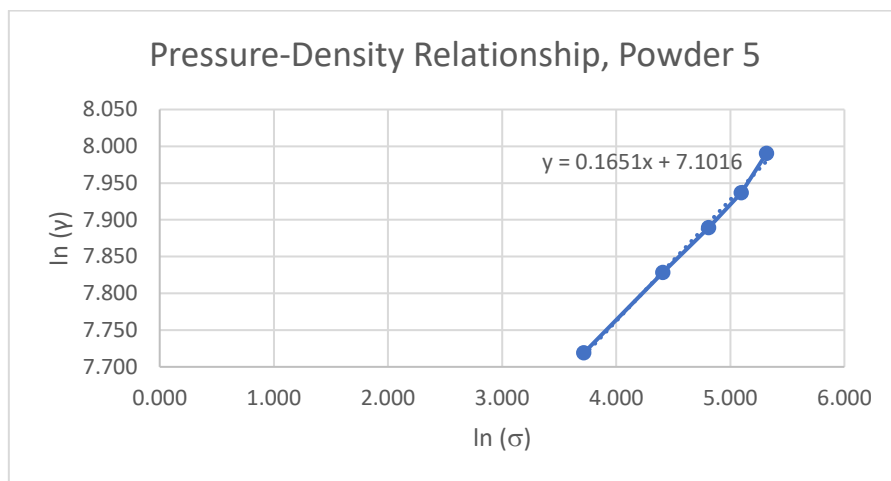


*Figure 41: Determining the compressibility for powder 5*
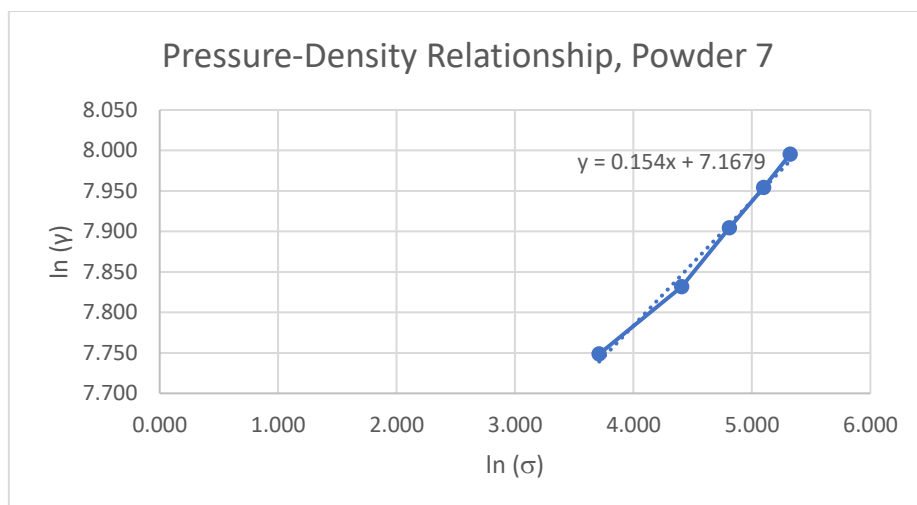


*Figure 42: Determining the compressibility for powder 7*

Note from Johanson's model [36] as reviewed in Section 2.3.2. that the pressure and density are related to the compressibility by the equation below:

*Equation 14: Pressure-density relationship for compressible materials*

$$\sigma_1/\sigma_2 = (\gamma_1/\gamma_2)^K$$

Taking the natural logarithm on each side of this equation, then solving for K, we get:

*Equation 15: Determining the compressibility constant*

$$\ln \sigma_1 - \ln \sigma_2 = K(\ln \gamma_1 - \ln \gamma_2)$$

$$K = \frac{\ln \sigma_1 - \ln \sigma_2}{\ln \gamma_1 - \ln \gamma_2}$$

It can thus be seen that the compressibility constant for each powder can be determined directly as the inverse gradient of the trendline of the $\ln(\gamma)$ versus $\ln(\sigma)$ graph for each respective powder. The compressibility constants were thus determined to be:

1. $K_{powder\ 2} = 5.62$

2. $K_{powder\ 5} = 6.02$

3. $K_{powder\ 7} = 6.49$

It was apparent that powder 2 has the lowest K value of the powders tested. A lower K value is indicative of a higher resultant density for the same applied pressure to the powder, thus powder 2 is the preferred powder for densification from the three powders tested.

Images of five of the fifteen sets of compacts formed during the uniaxial compression testing are shown in Figures 43 – 47.



*Figure 43: Compacts formed from powder 5 at 40kN*



*Figure 44: Defect observed on compact formed from powder 5 at 60kN*

*Figure 45: Compacts formed from powder 2 at 80kN*



*Figure 46: Compacts formed from powder 2 at 100kN*



*Figure 47: Compacts formed from powder 7 at 100kN*

Upon visual inspection of the compacts formed, the following observations were made:

1. For all three powders, the compacts formed at relatively low pressures resulting from applied uniaxial forces of 20kN (UCT1, UCT6, UCT11) and 40kN (UCT2, UCT7, UCT12) were difficult to handle without the edges disintegrating. This is shown in Figure 43. The relative density of these compacts was below 56%.

2. The compacts formed using powder 5 at intermediate pressures resulting from applied uniaxial forces of 60kN and 80kN (UCT8 and UCT9 respectively) exhibited cracking between the top and bottom faces. i.e. alligatoring [68]. This is shown in Figure 44.

3. For powders 2 and 7, reasonable consolidation of the compacts was achieved with applied uniaxial forces from 60kN and above (UCT3, UCT4, UCT5, UCT13, UCT14, UCT15). These compacts did not display visual defects, and could be handled without disintegrating. This is shown in Figure 45. These compacts all exhibited a relative density of 59% and above.

4. For all three powders, very good compacts were formed at a uniaxial force of 100kN (UCT5, UCT10, UCT15). This is shown in Figure 46 and Figure 47. The density of these compacts exceeded 65%.

Based on the K values achieved, as well as the observations above concerning the visual appearance of the compacts, powder 2 was selected for further testing. It is fortuitous that this powder is the most suitable for testing as it is the least expensive and requires the least preparation before use.

### 3.2.3. Internal Shear Test

Table 6 indicates the number allocated to each of the internal shear tests performed.

*Table 6: Classification of internal shear testing*

| Applied Load | Powder 2 |
|:---:|:---:|
| 50kg | Test IS1 |
| 40kg | Test IS2 |
| 30kg | Test IS3 |
| 20kg | Test IS4 |
| 10kg | Test IS5 |

The results of the internal shear tests are tabulated in Table 7.

*Table 7: Results of internal shear testing*

| Test Number | Vertical Load (N) | Normal Stress (MPa) | Horizontal Load (N) | Shear Stress (MPa) |
|:---:|:---:|:---:|:---:|:---:|
| IS1 | 500 | 0.139 | 495 | 0.138 |
| IS2 | 400 | 0.111 | 350 | 0.097 |
| IS3 | 300 | 0.083 | 193 | 0.054 |
| IS4 | 200 | 0.056 | 139 | 0.039 |
| IS5 | 100 | 0.028 | 66 | 0.018 |

A single sample was used to generate each data point, i.e. each of the tests (IS1 – IS5) was performed once. Typically, more samples should have been used for each data point, but a single sample was used for each due to the time taken to perform each test with the available equipment and the high cost of the large amount of titanium powder required for the testing.

The shear load at failure is determined by the point at which the shear load plateaus, as described in Section 3.1.6. The plots of the shear load versus the horizontal displacement are shown in Figures 48 – 52.
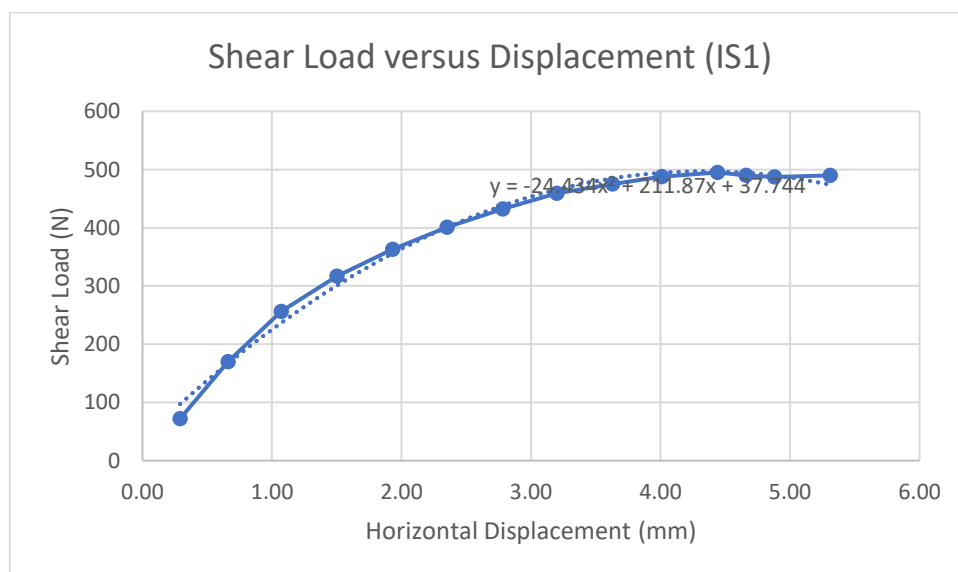


*Figure 48: Shear load versus displacement, 500N vertical load*
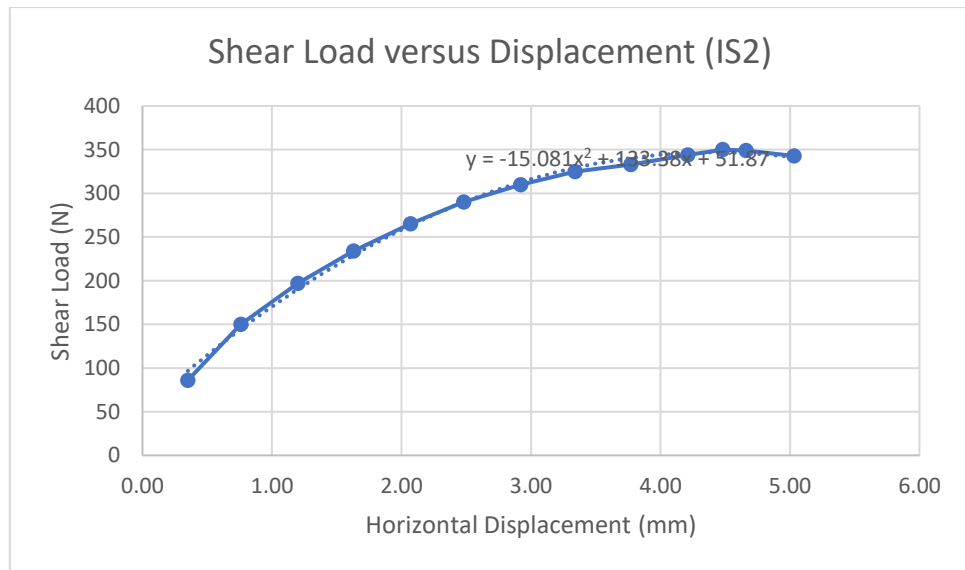
*Figure 49: Shear load versus displacement,400N vertical load*
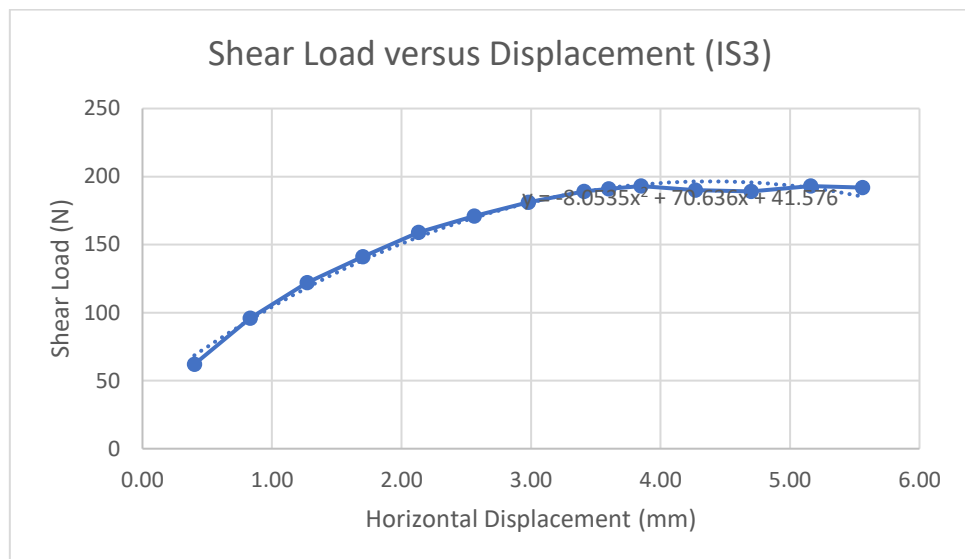


*Figure 50: Shear load versus displacement, 300N vertical load*
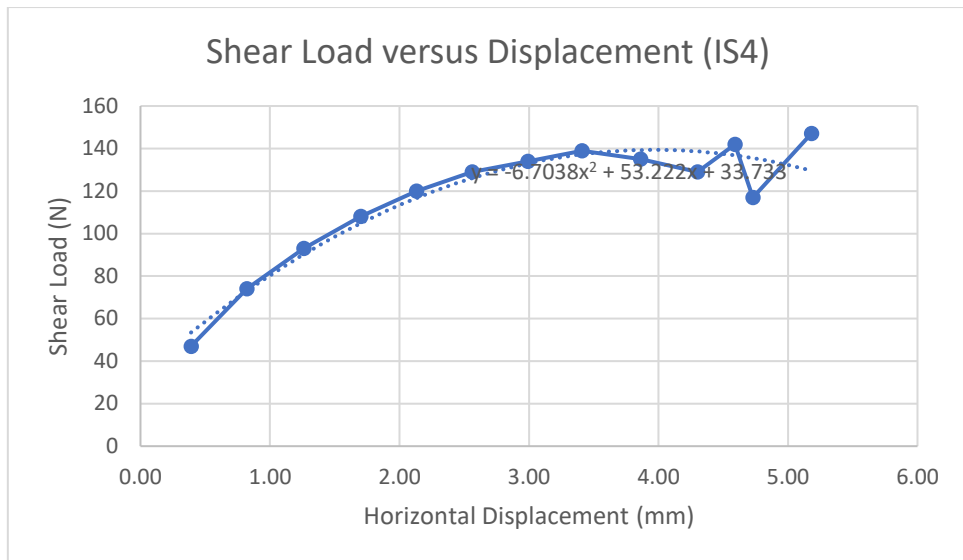
Figure 51: Shear load versus displacement, 200N vertical load
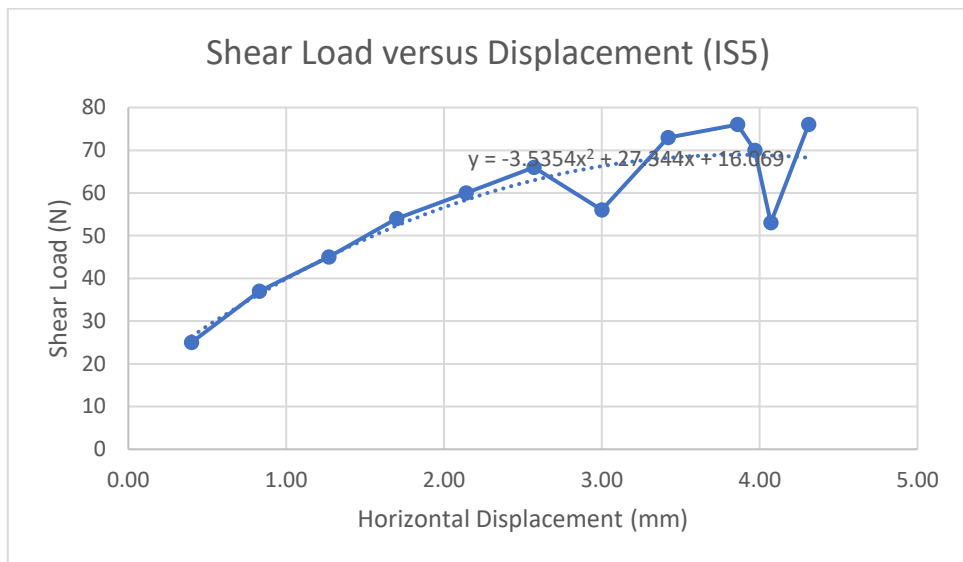


Figure 52: Shear load versus displacement, 100N vertical load

The values of normal stress versus shear stress at failure were then plotted for the five vertical loads at which the testing was performed, as shown in Figure 53.
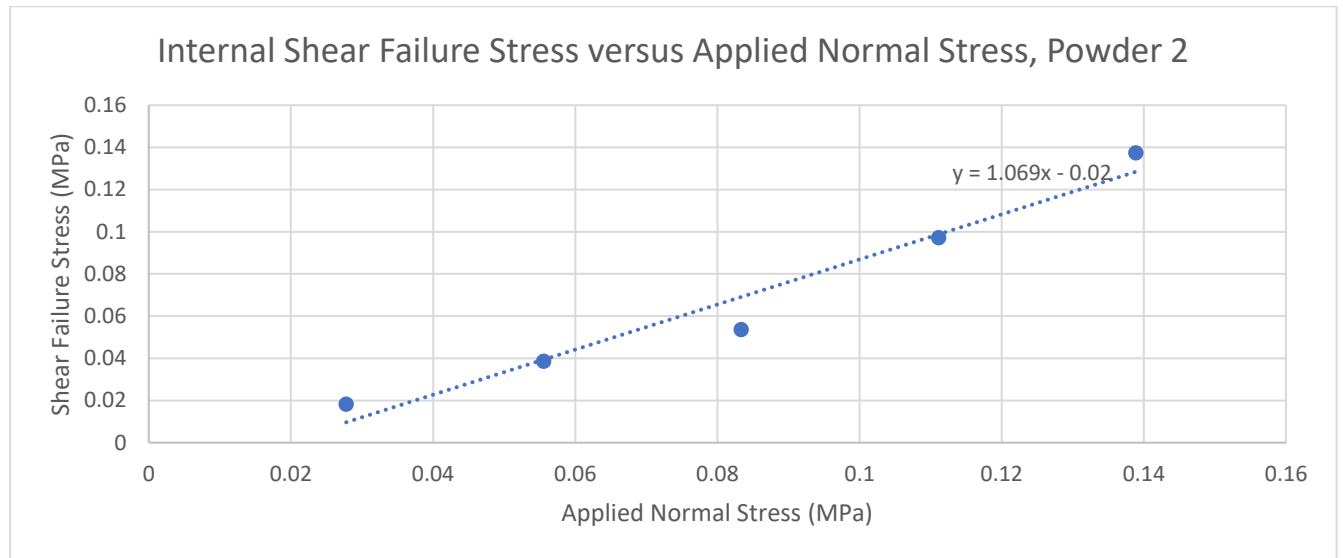


*Figure 53: Determining the internal friction angle for powder 2*

Note from the experimental methodology in Section 3.1.6. that the effective angle of internal friction is given by the equation below:

$$\delta = \tan^{-1}\left(\frac{\Delta\sigma_{shear}}{\Delta\sigma_{normal}}\right)$$

Thus, to graphically determine the internal angle of friction, a trendline was generated for the plot of internal shear failure stress versus applied normal stress. The internal friction angle is the arctangent of the gradient of this trendline. This value was determined to be 46.91° for powder 2.

### 3.2.4. Wall Shear Test

Table 8 indicates the number allocated to each of the wall shear tests performed.

*Table 8: Classification of wall shear testing*

| Applied Load | Powder 2 |
|---|---|
| 50kg | Test WS1 |
| 40kg | Test WS2 |
| 30kg | Test WS3 |
| 20kg | Test WS4 |
| 10kg | Test WS5 |

The results of the wall shear tests are tabulated in Table 9.

*Table 9: Results of wall shear testing*

| Test Number | Vertical Load (N) | Normal Stress (MPa) | Horizontal Load (N) | Shear Stress (MPa) |
|---|---|---|---|---|
| WS1 | 500 | 0.139 | 234 | 0.065 |
| WS2 | 400 | 0.111 | 156 | 0.043 |
| WS3 | 300 | 0.083 | 169 | 0.047 |
| WS4 | 200 | 0.056 | 122 | 0.034 |
| WS5 | 100 | 0.028 | 60 | 0.017 |

A single sample was used to generate each data point, i.e. each of the tests (WS1 – WS5) was performed once. Typically, more samples should have been used for each data point, but a single sample was used for each due to the time taken to perform each test with the available equipment and the high cost of the large amount of titanium powder required for the testing.

The shear load at failure is determined by the point at which the wall shear load plateaus, as described in Section 3.1.7. The plots of the wall shear load versus the horizontal displacement are shown in Figures 54 – 58.
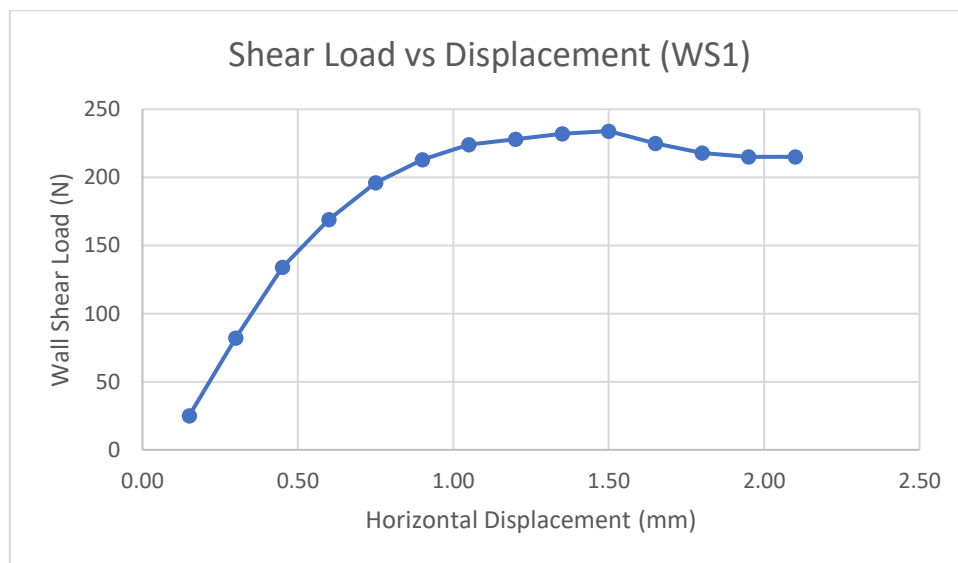


*Figure 54: Wall shear load versus displacement, 500N vertical load*
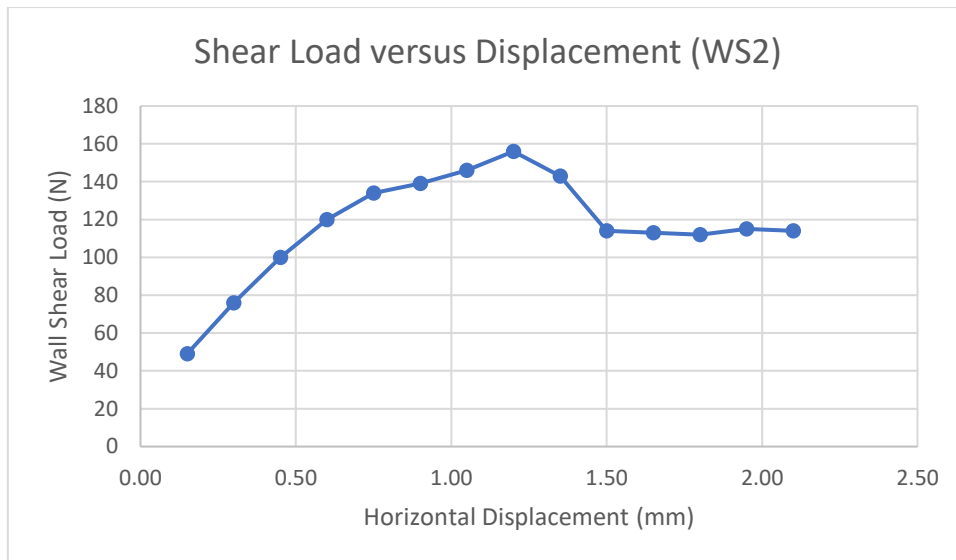
*Figure 55: Wall shear load versus displacement, 400N vertical load*
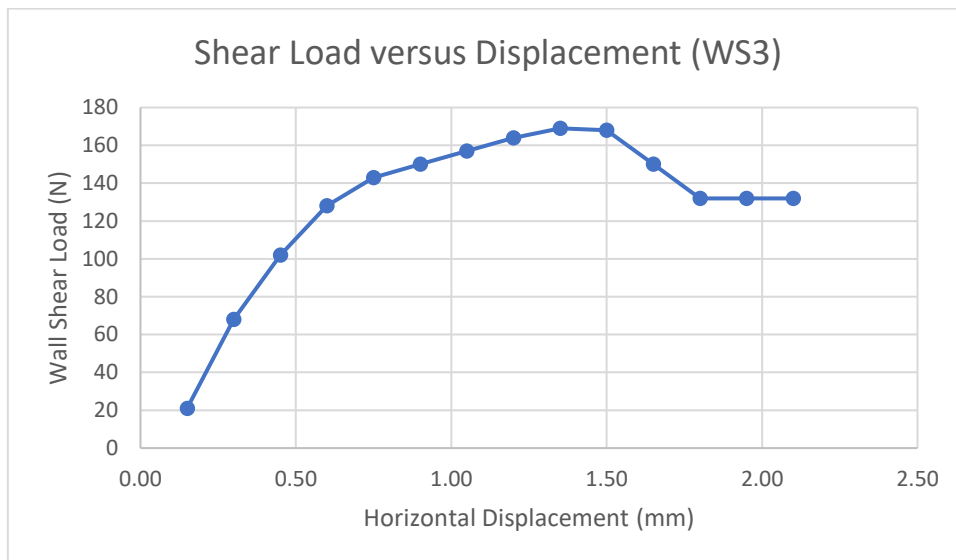


*Figure 56: Wall shear load versus displacement, 300N vertical load*
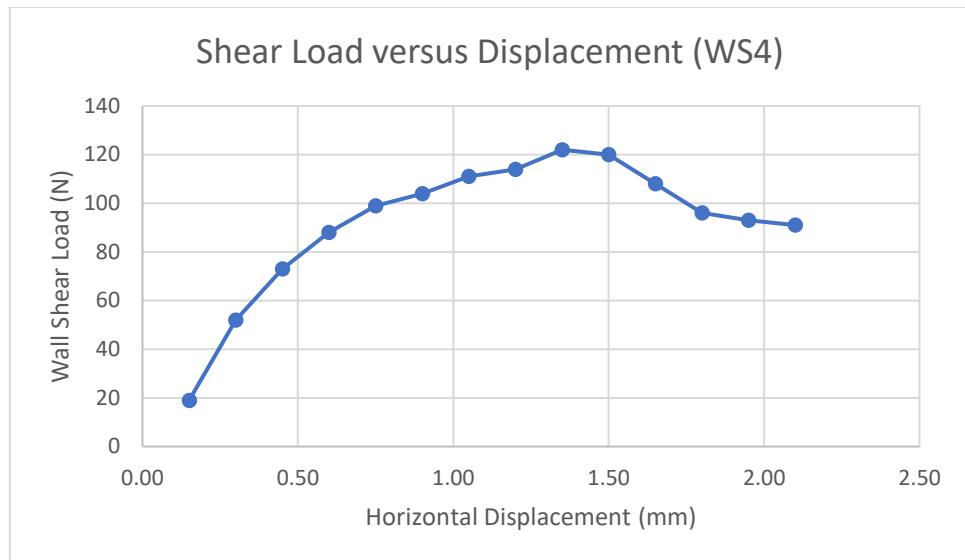
*Figure 57: Wall shear load versus displacement, 200N vertical load*
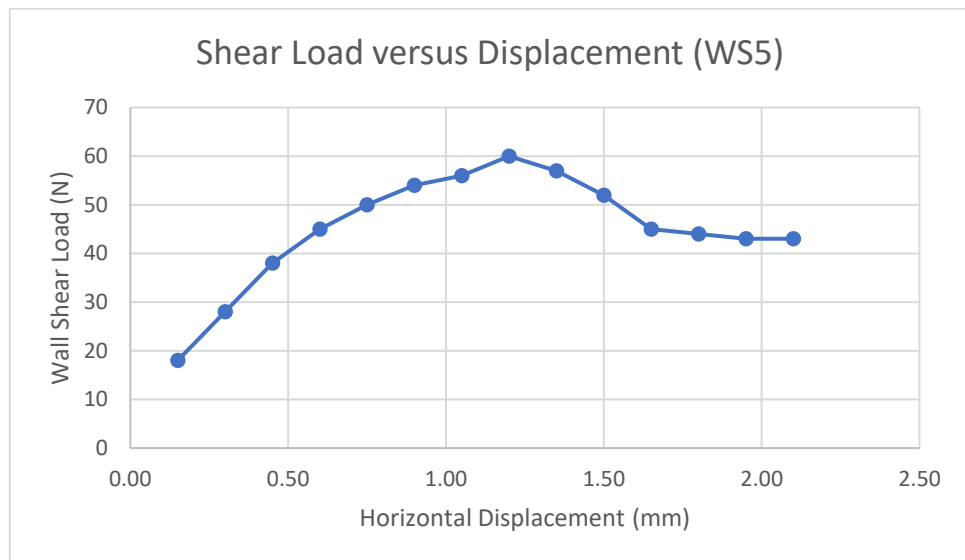


*Figure 58: Wall shear load versus displacement, 100N vertical load*

The values of wall normal stress versus wall shear stress at failure were then plotted for the five vertical loads at which the testing was performed, as shown in Figure 59.
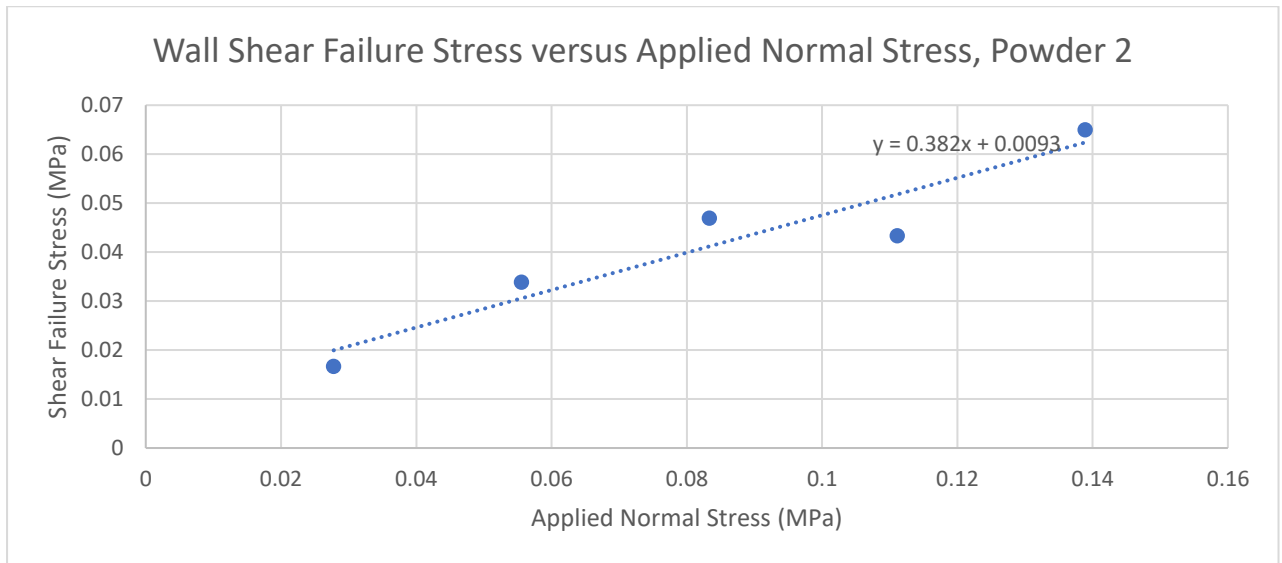


*Figure 59: Determining the wall friction angle for powder 2*

Note from the experimental methodology in Section 3.1.7. that the wall friction angle is given by the equation below:

$$\phi' = \tan^{-1}\left(\frac{\Delta\sigma_{shear-wall}}{\Delta\sigma_{normal-wall}}\right)$$

Thus, to graphically determine the wall friction angle, a trendline was generated for the plot of wall shear failure stress versus applied normal stress. The wall friction angle is the arctangent of the gradient of this trendline. This value was determined to be 20.91° for powder 2.

## 3.3. Experimental Discussion

### 3.3.1. Discussion of Experimental Shortfalls and their Justification

The internal and wall friction of the selected powder should have been determined using a rotary shear tester. However, traditional and modified shear box tests (respectively) were conducted due to unavailability of a rotary shear tester.

The values of compressibility and internal friction determined during testing were in the region of what was expected for these values, given the existing literature consulted [5] [69].

The value of wall friction was on the higher end of what was expected from literature [5] [69]. Possible sources of error were the use of a modified shear box for determination of the wall friction, and the use of a softer material for the shear plate than would typically be used for the rolls of a rolling mill. However, higher wall friction leads to a larger nip region, which in turn results in a higher roll force for the same compaction pressure. This high value for wall friction was thus retained in the MATLAB model of Section 4.3., resulting in a conservative mill design.

Ideally, more samples should have been used for the internal and wall shear tests to provide more accurate results; however, due to the large amount of powder required for each test and the expense of the powder, it was deemed sufficient for these purposes that a single sample be used.

### 3.3.2. Experimental Conclusion

Seven samples of HDH titanium powder were prepared for the experimental portion of this research. Strictly speaking, any of these powders (or a different powder) could have been used for the design of the mill, and the incorporation of safety factors in the mill design should ensure that any of these powders can in fact be rolled successfully. However, the preliminary test as well as the range of uniaxial compression tests performed was an efficient way of selecting a powder that should produce a compact with favourable characteristics.

Based on the results of the uniaxial compression testing, it was decided that the green density from the first pass through the rolling mill should, by design, exceed 65% in order to ensure reasonable consolidation and ease of handling of the green strip during further processing.

The compressibility factor, internal friction angle, and wall friction angle determined here were important factors in designing the mill. These will be used to build the MATLAB model, as described in Section 4.3. This model will be used to determine the expected behaviour of the mill during direct rolling of the selected powder, and will aid in ensuring that the mill designed, as described in Section 4.4., will withstand the expected loading, as modelled in Section 4.5, and thus be suitable for the testing described in Chapter 6.

# 4. Designing the SPS-DPR Mill

This chapter forms a critical part of the research in that it presents the bulk of the technical design for the mill. The chapter begins with an overview of the components already available for use, then moves into the process followed and the results obtained through simulation of the rolling mill behaviour, 3D modelling of the mill, and finite element analysis of its critical components. It then models a range of suitable circuits for achieving SPS of the material. Discussions are included per section as necessary.

## 4.1. Design Overview and Existing Components

### 4.1.1. Overview

The purpose of this project was the combination of the processes of Direct Powder Rolling (DPR) and Spark Plasa Sintering (SPS), for titanium. This was achieved through design, manufacture and testing of a mill capable of utilising either a one-step process to both consolidate and sinter powdered titanium in a single pass through the mill rolls to form a sintered compact, or a two-step process to first consolidate powdered titanium into a green strip, then sinter the green strip via a suitable current. This design chapter will discuss the requirements of the mill, the methods involved in designing its mechanical and electrical components, and the considerations that were borne in mind when conducting parametric testing on the manufactured mill.

The criteria for acceptable design of the components were that:

1. All components are safe to use in an academic environment
2. The stresses caused by the expected loads on the system do not exceed the yield strengths of the components
3. Manufacture can be completed easily, cheaply, and within the timeframe of the project
4. Quick and easy reconfiguration of the roll gap is possible during parametric testing

### 4.1.2. Existing Components

In 2017, a group of final-year mechanical engineering students at the University of KwaZulu-Natal was assigned the SPS-DPR rolling mill project [70]. Upon project completion, they had designed and manufactured certain components of the mill, but did not complete the project in its entirety. The degree of completion of each of the components from the 2017 project, and their suitability for this project, will be discussed below.

*Rolling mill frame*

This is one of the most critical components of the mill. In 2017, the frame was designed but not manufactured. The nature of the design was complex, with limited access to certain mill components, which would lead to difficulties experienced during operation and testing of the mill. The rolling mill frame design was thus not used for this project.

*Compacting rolls and drive system*

The rolls designed in 2017 are 350mm in diameter, and 50mm wide. Each of the rolls is on the same shaft as a gear, driven by a worm, with a ratio of 52:1 (speed reduction) between the worm and gear. The rolls and gear sets had been manufactured in 2017, and were deemed suitable for this application, through gear calculations and FEA on the rolls using Siemens NX. The rolls manufactured in 2017 were thus used for this project.

The worms were designed to be coupled to each other and to motor driving them via hubs fixed to each other with an adhesive polymer for electrical isolation. The couplings for the system had been designed but not manufactured. The method of using adhesive for the coupling of high-torque components was ruled out, and thus the coupling design was not used for this project.

The roll shafts and worm shafts were designed to be fixed to the frame via adjustable bearing housings with vesconite bushings. The bearings for the system had been designed but not manufactured. The use of a two-piece vesconite bushing for each bearing was not ideal, nor was the use of blind threads on the bearing housings for connecting the housings to the mill frame. The bearing and bushing designs was thus not used for this project.

A 5.5kW SEW AC motor was selected in 2017. The motor was tested and found to be in good working condition, as described in Section 5.2., and through simulation of the rolling mill using MATLAB, as described in Section 4.3.5., was determined to meet the torque requirements for the desired compaction. The motor selected in 2017, together with the Emerson VSD donated for the purpose of speed control, was be used for this project.

*Roll collars to prevent loss of powder*

The rolls collars are plates with their diameter larger than that of the roll which were bolted to either side of one of the rolls to prevent material loss from the sides of the rolls. The design of the roll collars was such that they were difficult to remove, and posed a risk of creating a short circuit in the SPS system if left on the rolls during rolling. The manufactured roll collars were thus not used for this project.

*Screw-feed system for the powder*

This component was designed and manufactured in 2017. However, upon consideration of both screw-fed and gravity-fed hopper systems, it was decided that a gravity-fed hopper would be used to supply powder to the rolls. The manufactured screw-feeding mechanism was thus not used for this project.

*Inert gas chamber for the SPS process*

This chamber was designed and manufactured in 2017. However, due to flaws in its sealing, a non-inert environment results within the chamber rendering it unfit for purpose. The manufactured chamber was thus not used for this project.

*SPS circuit*

The design of the SPS system was a good starting point, but was incomplete. Additionally, there were concerns with the point of application of the current to the system. This system was thus redesigned.

As described above, some of the components manufactured or selected in 2017, primarily the drive components, were deemed acceptable for the current design, and were thus used to save the time and cost associated with their manufacture. However, there were still several outstanding components which were required to be designed and manufactured before the mill could be assembled and tested.

The major components still required to be designed and manufactured for this project were as follows:

1. A structural frame for the rolling mill and its associated SPS system

2. A set of cheek plates to limit powdered material loss from the edges of the rolls

3. A gravity-fed hopper to provide powder to the rolls

4. A suitable coupling and bearing mechanism for the rolls and gears

5. An electrical circuit to create the pulsed waveform required for SPS of the compact, and a mechanism to apply this pulsed waveform to the compact

## 4.2. Design Process

Due to the various interacting aspects of this project, it was important to determine at the outset a logical sequence of steps to be followed in the design process. Upon consideration of the objectives to be achieved and the resources available, the higher-level design process included the steps detailed below.

### 4.2.1. Simulation of the Mill Behaviour

The primary goal during this step was to determine the loads expected to act on the system during operation. For a suitable rolling mill to be designed, the expected behaviour of the mill should be simulated with the powder selected during experimental testing. The Johanson model was used as the guiding theory, and MATLAB was the modelling software used to run the simulation.

The inputs to the MATLAB simulation were:

1. The characteristics of the titanium powder to be rolled:

    a. Compressibility, $K$

    b. Internal friction angle, $\delta$

    c. Wall friction angle, $\phi'$

2. The characteristics of the mill:

    a. The roll diameter, $D$

    b. The roll width, $W$

    c. The roll gap, $S$

The outputs of the MATLAB simulation were:

1. The nip angle, $\alpha$, based on equating the pressure differential equations at nip and slip regions. Note that the nip angle is dependent only on compressibility ($K$) and frictional characteristics (and $\nu$) of the powder for small roll gaps ($S$)., and the nip height, $h_n$

2. The feed angle, $\theta_f$, and the feed height, $h$

3. The mean normal stress at the nip angle, $\sigma_\alpha$, based on the feed pressure $P_0$ (an estimated value of $P_0$, based on previous powder rolling research [71], was used)

4. The mean normal stress at the minimum roll gap, $\sigma_{max}$

5. The maximum horizontal pressure required, $P_m$, based on the mean normal stress

6. The roll separating force, $F$, based on $P_m$

7. The roll torque required, $T$, based on $P_m$

The following parameters for the system should also be checked:

1. The motor torque required (to ensure the selected motor was suitable)

2. The motor speed required (to be controlled via the VSD). Typical stable rolling speeds were confirmed from previous works [66], to ensure the value for roll speed in this system was not so low as to result in very narrow strip being formed, and not so high as to cause insufficient densification during rolling. These results are witnessed during the parametric testing described in Section 6.2.3.

3. The desired output density of the compact, and the corresponding mean normal stress on the powder in the minimum roll gap, were calculated. This required value must be less than or equal to the actual stress value simulated, to ensure the desired density is achieved.

## 4.2.2. Generating Solid Models using CAD

The required components were modelled using Siemens NX software, as this software is available for use through the university and can be used both for CAD and FEA. The design criteria and considerations discussed earlier in this chapter were borne in mind when generating the solid models as described in Section 4.4.

The parts and assemblies designed in this process were subject to a sanity check, to ensure there is sufficient clearance between components, access to the mill components is not restricted, and that the assembly is not unwieldy.

Once the design was finalised, 2D drawings were generated from the solid models, which were used for manufacturing the mill frame and auxiliary components.

The components required for the mill have been listed in Section 4.1.

## 4.2.3. Testing the Solid Models using FEA

The CAD models were strength-tested using the FEA package of the Siemens NX software, as described in Section 4.5. The FEA process was iterative; proposed designs were strength-tested, weak points addressed in the model, and then the model retested, until an optimal design was reached.

Any design modifications necessary, as identified during the strength testing step or through further consideration of the requirements of the mill and optimal operation thereof, were implemented before finalisation of the design.

### 4.2.4. Modelling the SPS System

The circuit to provide high current pulsing to the sample was designed and built from components which are cost-effective and easy to source. As discussed in the literature review in Section 2.4., SPS has been successfully conducted with many different current waveforms. This allowed for a modicum of flexibility in the design of the electrical circuit. At its most complex, the electric circuit includes the following components:

1. AC single-phase input

2. A transformer to step down the voltage

3. A rectifier to convert AC to DC

4. A capacitor to smooth the voltage

5. A means of pulsing the DC supply to the green compact

6. A means of transferring the generated pulsed DC through the green compact

The assembly of the above system would result in high current, low voltage, smoothed, pulsed DC to the titanium compact. However, the same effect may be achieved through applying continuous DC to the compact (i.e. through excluding component 5 above), or indeed through applying high current, low voltage AC to the compact (i.e. through excluding components 3 – 5 above).

Simulink was the modelling software used for the design and simulation of the electrical circuit for the SPS system.

## 4.3. Rolling Mill Simulation (MATLAB)

This section will record the results of the simulations of the rolling mill using Johanson's model and MATLAB software.

Johanson [36] emphasises the importance of considering the actual powder to be rolled when designing of the mill, due to the dependence of the mill output on the powder properties, as reviewed in Section 2.3.2. The powder to be rolled in this mill was thus selected and tested as described in Chapter 3. The results of the powder testing were used to build up the MATLAB model. The results of the MATLAB model were in turn used to build up the FEA models in Siemens NX, as described in Section 4.5.

### 4.3.1 Powder Properties

As per the experimental chapter, the properties of the 100 mesh HDH titanium powder to be rolled through the mill are as follows:

1.  Compressibility: $K = 5.62$

2.  Internal friction angle: $\delta = 46.91°$

3.  Wall friction angle: $\phi' = 20.91°$

### 4.3.2. Mill Properties

The rolls designed in 2017 [70], which were used in this mill, are as follows:

1.  Roll diameter: $D = 350mm$

2.  Roll width: $W = 50mm$

### 4.3.3. Additional Input Parameters for the Model

Further parameters which are needed for the simulation are as follows:

1.  Feed pressure: $P_0 = 196\ 000$ Pa (estimated [5] [71])

2.  Minimum desired density: $\rho_{rel} = 59\%$ (from observation of the uniaxial pressure test samples)

### 4.3.4. Building the MATLAB Model

The equations prescribed in the Johanson model [36] were used to build MATLAB model. The first step was defining all the known parameters as above – the powder parameters were determined from experimentation as described in Chapter 3, and the mill parameters were given by the dimensions of the existing rolls manufactured, as discussed in Section 4.1.2.

Next, the nip angle was determined. This was a critical step in the process as much of the mill behaviour depends on the angular position at which the powder begins to compact (i.e. the nip angle).

The nip angle was determined graphically by equating the pressure differential in the nip and slip regions, as shown in Figure 60.
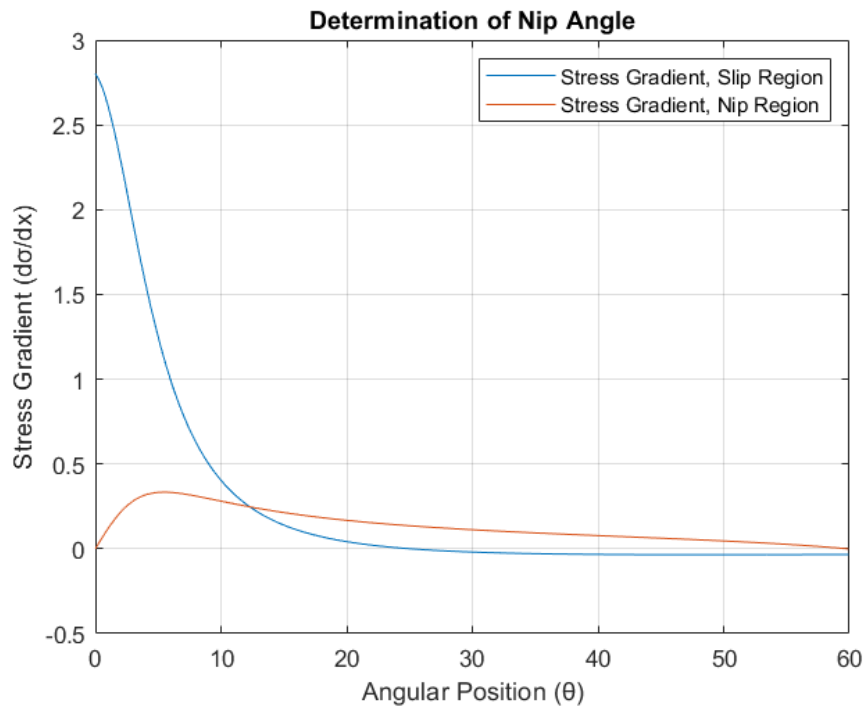


*Figure 60: Determination of nip angle (MATLAB model)*

To confirm that the nip angle was independent of the roll gap [36], the simulation was run at varying roll gaps. The results are shown in Figure 61.
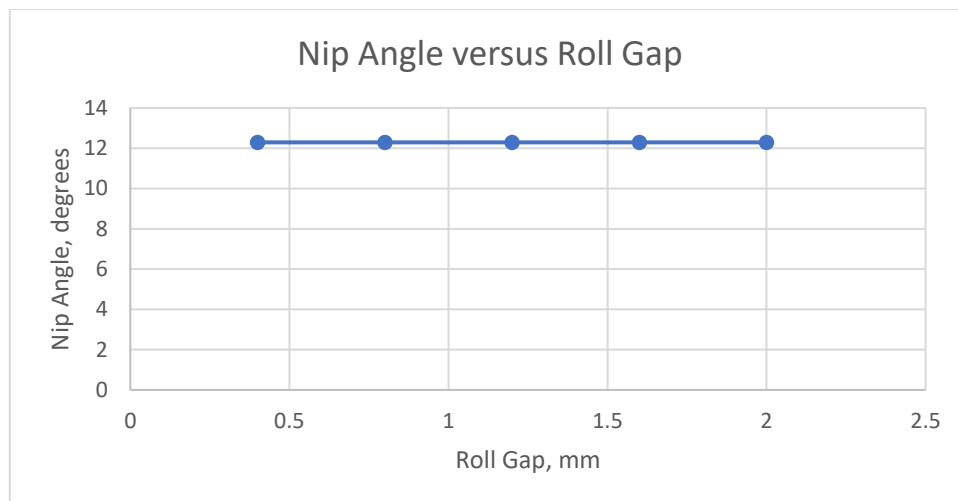


*Figure 61: Nip angle versus roll gap (MATLAB model)*

This is important to note, as during the testing described in Section 6 the powder characteristics remained constant, but the roll gap was varied. If the nip angle was influenced by the roll gap, the pressure distribution would need to be recalculated for each proposed roll gap.

The next step was to determine the mean normal stress in the feed and nip regions. The stress is relatively low in the feed region, and remains constant throughout this region (i.e. from the feed angle to the nip angle). The stress is higher in the nip region, as the rolls start to compact the powder, and increases from the nip angle to a maximum value at the minimum roll gap, after which the material is ejected from the rolls.

The stress distribution in the nip region is shown in Figure 62.
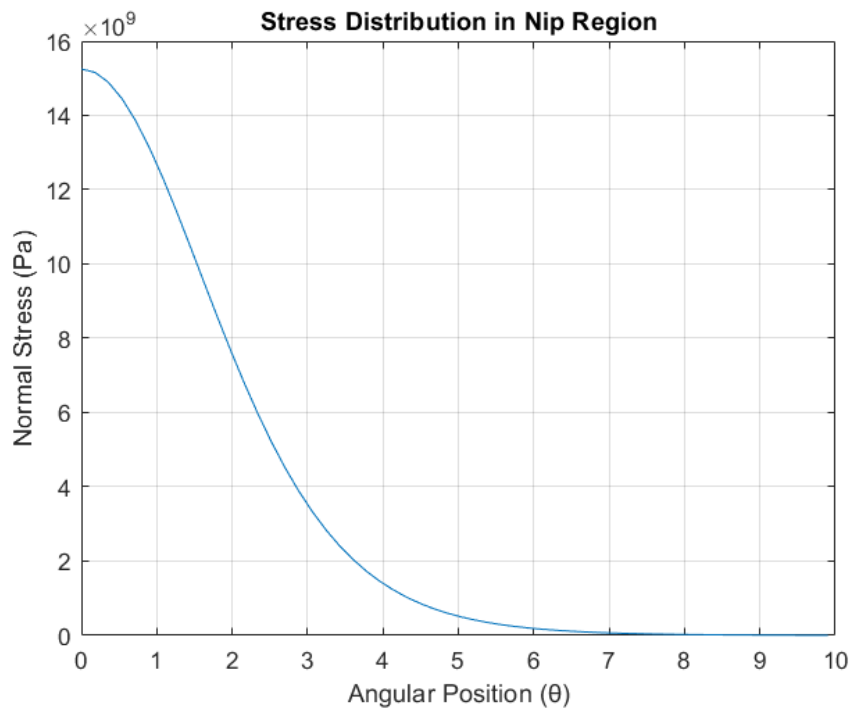


*Figure 62: Stress distribution in nip region (MATLAB model)*

The stress distribution in the nip region was then used to calculate the roll separating force and the roll torque by integrating the pressure on the roll surface from the nip angle to the minimum roll gap. These outputs were important as they formed the basis of the loading conditions for the FEA model in Section 4.5. They are summarised in Section 4.3.5.

Finally, the torque and speed required from the motor were determined, as was the expected relative density of the compact. The acceptance criteria for the motor torque and speed were that they fall within the motor's ratings; the maximum rated torque of the motor is 61Nm, and the maximum speed of the motor (as measured using a tachometer during testing of the motor, described in Section 5.2.2.) is 841 rpm. Additionally, the range of rolling speeds fell within the linear speed range at which it was expected that reasonable consolidation would occur [66]. The density of the green compact after a single pass through the rolls should also be higher than 65% in order to be easy to handle for subsequent processing, as determined during the uniaxial compression testing on the powder in Section 3.2.2. The torque and speed requirements are summarised in Section 4.3.5.

To determine the effect of varying roll gap on the maximum pressure applied to the compact, as well as the density of the compact formed, the simulation was then run with varying roll gaps to determine the influence on these two outputs. This was useful during testing of the mill as described in Chapter 6. The results are shown in Figure 63.
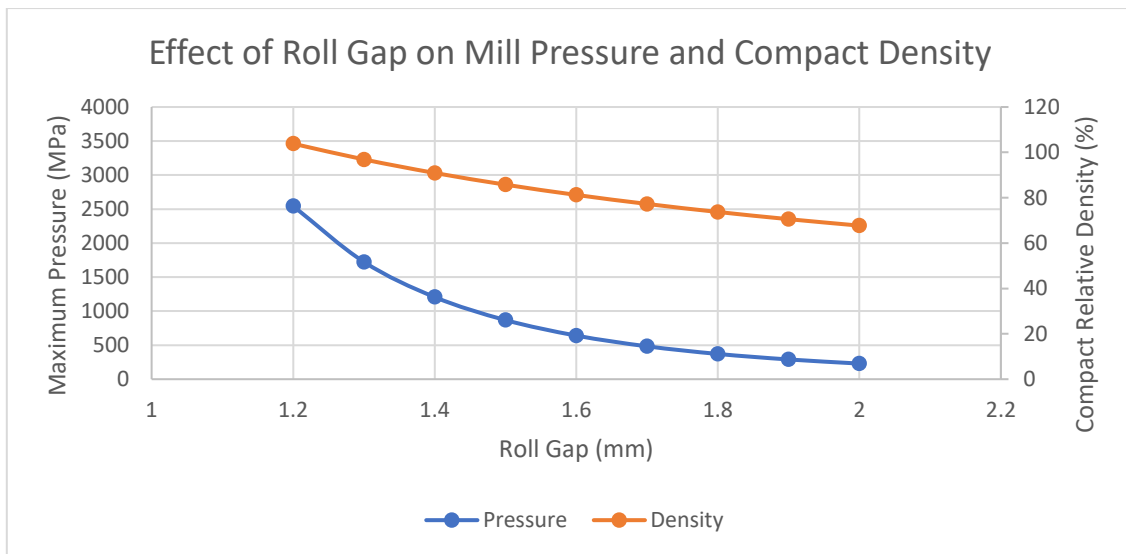


*Figure 63: Maximum pressure and density versus roll gap (MATLAB model)*

As expected, the smaller the roll gap, the higher the pressure applied to the powder, and the greater the density of the compact formed. As can be seen, the maximum pressure required in the mill increases exponentially as the compact reaches theoretical full density; this is expected from the pressure-density relationship, and is perhaps better viewed by directly plotting the simulated values of pressure against density, as shown in Figure 64.
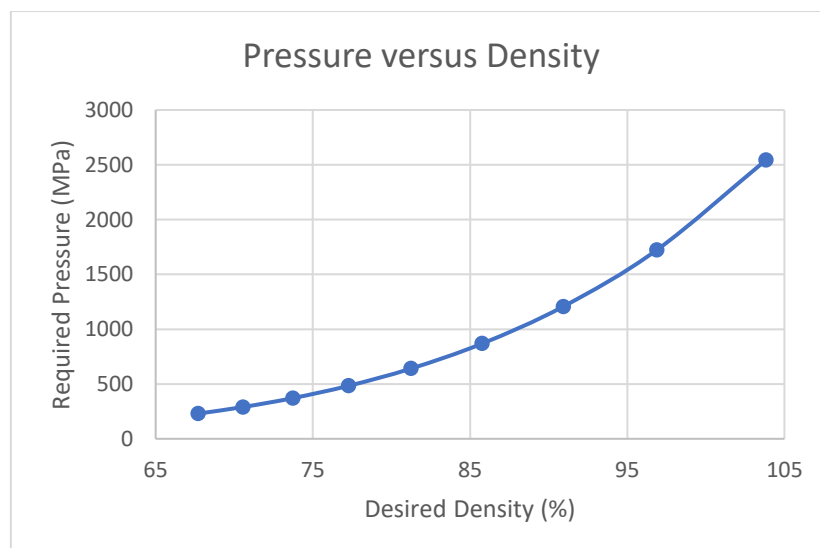


*Figure 64: Required pressure versus desired density (MATLAB model)*

The correlation between these graphs, as generated from the MATLAB code written by the student, and the mill behaviour as described by the Johanson model, validates the MATLAB simulation. It was thus accepted that the MATLAB model is representative of the actual rolling mill behaviour during the DPR process.

The full code written by the student for the MATLAB simulation is shown in Appendix A.

### 4.3.5 Simulation Results and Discussion

For the MATLAB simulation, conducted on a roll gap of S = 1.6mm, the following behaviour was observed:

1. Nip angle: $\alpha = 12.29°$; nip height, $h_n = 37.25$mm

2. Feed angle: $\theta_f = 25.08°$; feed height: $h_f = 74.18$mm

3. Mean normal stress at the nip angle: $\sigma_\alpha = 0.73$ MPa

4. Mean normal stress at the minimum roll gap: $\sigma_{max} = 15.3$ GPa

5. Maximum horizontal pressure (at minimum roll gap): $P_m = 641.2$ MPa

6. Roll separating force: $F = 214.5$ kN per roll

7. Roll torque required: $T = 963$ Nm per roll

8. Motor torque required: $T_{motor} = 37$ Nm (acceptable as it is below the maximum rated motor torque of 61Nm)

9. Motor speed required: $n_{motor} = 179 – 593$ rpm (based on previous research [66], which prescribes linear roll speeds equivalent to a rotational roll speed range of 3.4 – 11.4 rpm)

10. Expected compact density: $\rho_{rel} = 81.25\%$ (acceptable as it is above 65%)

These results are used in further design of the mill. The nip and feed heights are used as reference points when determining the required height of the cheek plates and the expected point of application of the loading thereon. The roll separating force is used in determining the magnitude of the loads to be applied to the 3D model during the finite element analysis. The motor torque and speed required are used as a double-check to ensure that the existing motor is suitable for the application. And the expected compact density is used to ensure that, within the design parameters chosen for the mill (notably the characteristics of the selected powder and the dimensions of the mill, including its roll gap), the compact formed will be sufficiently dense for further handling.

## 4.4. 3D Design and Modelling (Siemens NX and OnShape)

### 4.4.1. 3D Model Overview

The design of the 3D model began with the design of a suitable frame. The frame needs be sufficiently strong and rigid to handle the loads expected during the rolling process without appreciable deflection, while providing suitable mounting points for all components such as the drive system (motor, worms, gears, rolls, and associated bearings), cheek plates, powder hopper, exit slide, and SPS system. For the 3D model, it was necessary to incorporate the rolls and gears designed and manufactured in 2017 [70], as well as the additional components as described above. As discussed in Section 4.4.4., the counter-rotating rolls should be positioned such that they allow for gravity feeding of the powder, with a mechanism of roll gap adjustment incorporated into the design. Finally, it was important to consider suitable electrical isolation of the SPS circuit from the frame for safety reasons.

The initial modelling of the mill was done using Siemens NX. However, several months of design time were lost in the course of the research due to remote access to this modelling software coupled with COVID-19 lockdown measures. The final design was thus done using OnShape, a cloud-based 3D modelling platform.

With a view to designing a simple yet elegant solution for the rolling mill, there were several things to consider for each of the components and how they interact with one another. These considerations will be discussed for each sub-section below.

### 4.4.2. Rolling Mill Frame

The rolling mill frame must conform to the following specifications:

1. It should provide the strength required during mill operation without yielding, and without excessive deformation – particularly in the radial direction as this will affect the consistency of the compacted strip thickness along its length

2. It should provide all mounting points necessary for the individual components

3. It should allow easy access to the formed strip

4. It should be cheap and easy to manufacture, with a design that is easy to scale up in future

5. It should allow for easy reconfiguration during testing, such as:

    a. Adjustment of the roll gap

    b. Removal of the powder hopper

    c. Removal of the cheek plates

    d. Removal of the SPS system

The design of the rolling mill frame was an iterative process, as the proposed model for the frame needed to be strength-tested using finite element analysis, with necessary adjustments being made accordingly, before finalising the model.

The final 3D model of the frame is shown in Figure 65.
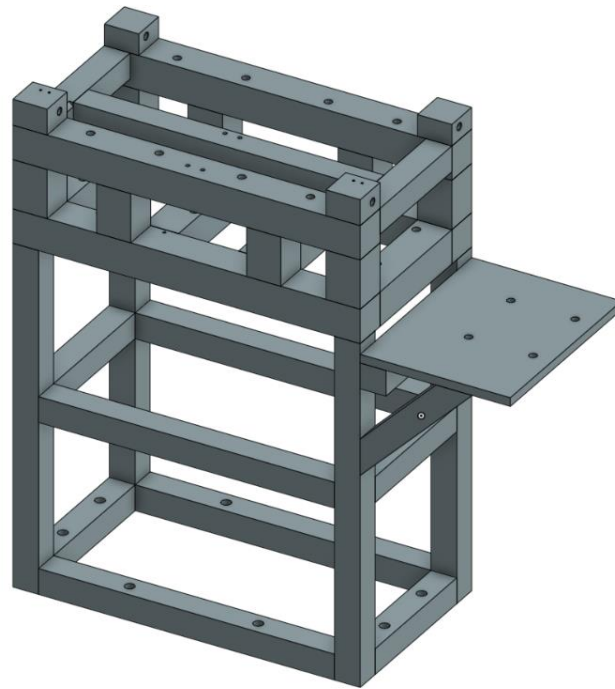


*Figure 65: 3D model of the rolling mill frame (OnShape model)*

This model consists of 60mm and 80mm solid square bar, joined together by 10mm all-round bevel-groove welds – the size of which were determined by referring to the AWS D1.1:2020 standard [72] – and a 20mm-thick plate for mounting the motor.

### 4.4.3. Powder Feed to the Rolls

Powder can be fed into the space between the mill rolls either by gravity feed (where particles are allowed to flow freely under the influence of their own weight) or force feed (usually via a screw-feeding mechanism) [34]. The selection of the feeding mechanism is usually based on the properties of the powder and the desired compact density. Upon review of the relevant literature, it was expected that a force fed system will introduce unnecessary complexity into the mill (due to the fluctuating feed pressure) which would not be present with a gravity fed system [34] [41] [71].

The Johanson model [36] was one of the most relevant sources for this project with respect to the theory behind direct powder rolling. This model assumes the material is fed to the rolls via gravity [39] (without considering the additional complexity from a screw fed system mentioned above). However, it does not explicitly investigate the effect of powder feed rate on the rolling process; it is merely assumed that sufficient powder is supplied to the rolls to yield a homogeneous compact [73]. There are fortunately other sources [5] [66], which have determined that the density of the compact formed is proportional to the powder feed rate. This is however only possible up to a certain critical feed rate, after which the rolling mill will be overloaded (this is because the compact density is also proportional to the pressure applied to the rolls, which is limited by the mechanism providing torque to the system).

To ensure consistent process flow, it was determined that the mass flow rate required from the hopper must equal the mass flow rate of the material being compacted through the rolls. This will ensure mass flow equilibrium, i.e. the mass of powder fed into the rolls will equal the mass of the compact exiting the rolls (plus any powder leakage). The mass flow rate of the material through the roll is given by the equation below.

$$\dot{m} = \rho\dot{V} = \rho \times W \times S \times \frac{\pi D n}{60}$$

This mass flow rate was calculated at a relative compact density of 81.25%, roll gap of 1.6mm, and rolling speed range of 3.4 – 11.4 rpm, as used during the MATLAB simulation described in Section 4.3. The roll width and diameter used are 50mm and 350mm respectively. The result was that 18 – 61 grams of powder per second must be fed to the rolls by the hopper, dependent on the particular roll speed being used. The upper mass flow rate value was used for subsequent hopper calculations as it represented the highest flow rate that would reasonably be required for this mill.

Using the powder characteristics determined during experiments on the HDH titanium, the critical angle was approximated as 32° [74]. To ensure free flow through the hopper by prevention of arching and ratholing [74], this was rounded down to 30° to be conservative – note that a lower angle with the vertical represents a steeper hopper wall and thus a greater mass flow rate through the hopper.

The cheek plates provide the mounting points for the hopper.

The output of the powder hopper was designed to be adjustable, to enable good control of powder distribution onto the rolls, and to allow for ease of parametric testing as described in Chapter 6. Five identical stoppers were used for this purpose.

The CAD model of the hopper used for powder feed to the rolls is shown in Figure 66.
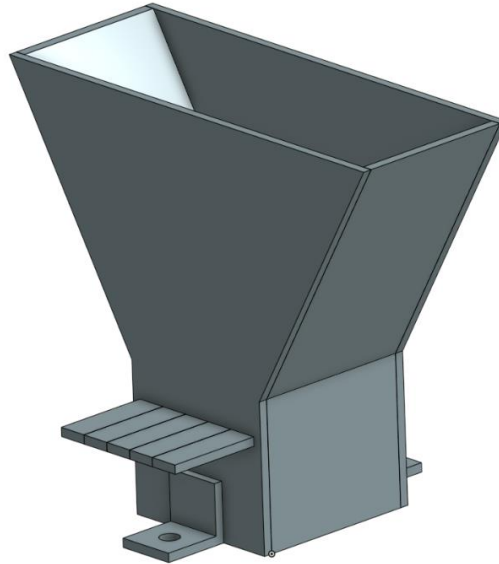


*Figure 66: 3D model of the gravity feed hopper (OnShape model)*

### 4.4.4. Roll Configurations

There are in general three configurations [34] [75] that can be used for the mill rolls in terms of the position of the rolls and the direction of the feed, as shown in Figure 67. These are:

A. A two-wide horizontal set of rolls, fed vertically

B. An angled set of horizontal rolls, fed at a non-zero angle to the horizontal plane

C. A two-high horizontal set of rolls OR a two-wide vertical set of rolls, fed horizontally
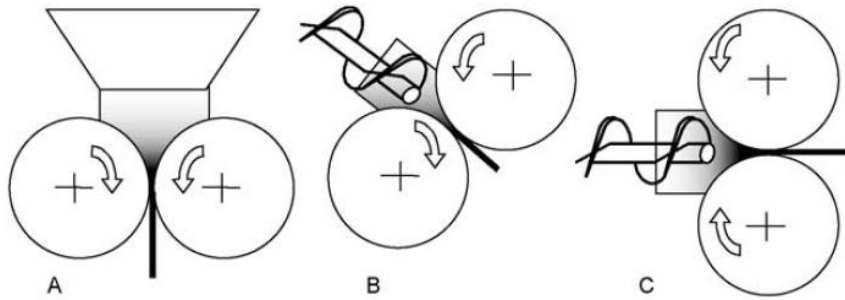


*Figure 67: Rolling mill configurations [34]*

Since it was determined that the hopper design will utilise gravity feed, it was clear that the vertical feeding of the powder (configuration A above) was the most suitable roll configuration, as it takes advantage of the gravitational force on the powder to feed the rolls, without reliance on any further feeding mechanism.

### 4.4.5. Rolls, Edge Control, and Gap Adjustments

The available rolls, manufactured in 2017 [70] were used for the mill. They were arranged as per configuration A of Section 4.4.4. These rolls are 350mm in diameter and 50mm wide. They have been surface-hardened. On inspection of the rolls, they required surface treatment before use as there was a layer of oxide on the rolling surface.

For edge control, it was decided to use cheek plates instead of the existing rolls collars due to them being easier to remove during the sintering process. In the case that they are not removed during sintering, one of the considerations for the material in contact with the roll should be its electrical conductivity, as this is expected to heavily influence the results of the SPS process; this has been reviewed in Section 2.4.3.

A previous DPR mill project [76] described a few issues encountered when testing their direct powder rolling mill, namely powder adherence to the rolls, and unwanted curving of the strip.

For the first issue, that of powder adherence to the rolls, it was decided that loose powder could easily be dealt with by strategic placement of the carbon brushes, since this would not affect the actual rolling process. A means of removing stubbornly-adherent powder without damaging the roll surfaces would be considered if this was found to be a problem during testing.

In terms of preventing the strip from curving, special attention was paid to ensuring synchronous roll speed, identical roll diameters, and prevention of undue forces on the strip from the cheek plates (through good control of flow from the hopper). Note that in certain cases, such as [15], bent strip is produced intentionally by using different roll diameters; however, this was not the intention here.

The cheek plate used for edge control is shown in Figure 68.
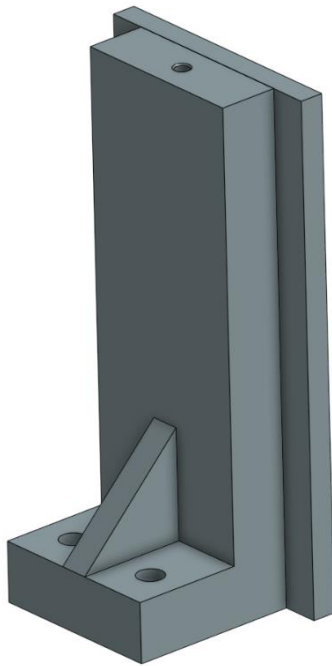


*Figure 68: 3D model of the cheek plate (OnShape model)*

Design of a mill with a fixed roll gap would not have be suitable for the purposes of parametric testing. The mill gap was thus designed to be adjustable, through use of a screw mechanism on one of the rolls. The adjustment mechanism for the roll gap is shown in Figure 69.
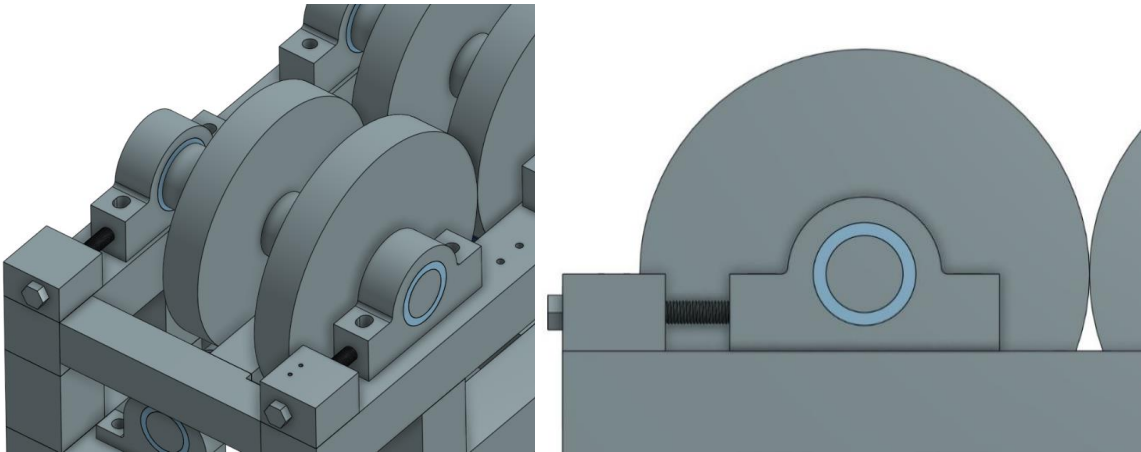


*Figure 69: 3D model of the screw mechanism for roll gap adjustment (OnShape model)*

### 4.4.6. Couplings and Bearings

The couplings used to transmit power from the AC motor to the worm shafts were selected such that they are robust, easy to install, dimensionally compatible with the existing drive system, and allow for electrical isolation of the motor. Due to the low cost and ease of availability of existing coupling systems which meet these requirements, an off-the-shelf solution was selected for this purpose. The solution selected was the Timken QF25R coupling; this is shown in Figure 70.
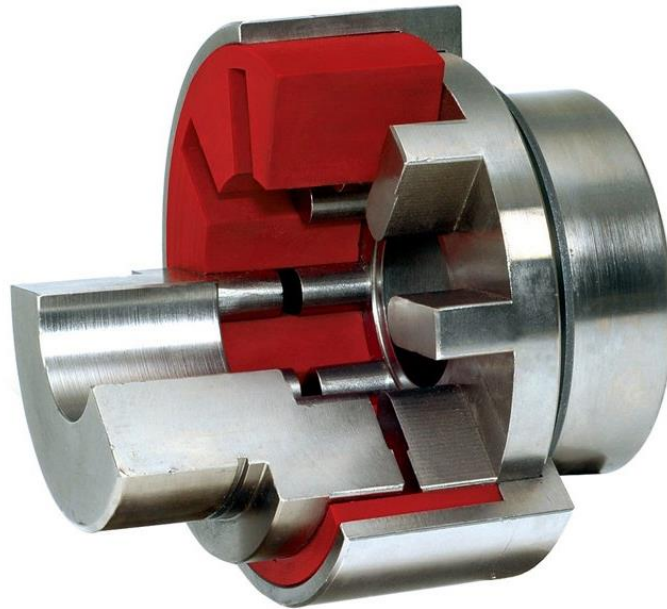


*Figure 70: Sectioned view of flexible coupling [77]*

The bearings chosen for this system must provide bearing support in all three directions (i.e. radial, axial and tangential), as well as allow for electrical isolation of the worm and rolls shafts from the frame. It was determined that the off-the-shelf solutions available for this application would have been prohibitively expensive (not least because of the number of bearings required for the mill). The bearings were thus designed specifically for this application.

The adjustable bearing housing and vesconite bushing for the roll shafts are shown in Figure 71. The worm shafts employ a similar solution with a slightly different geometry.
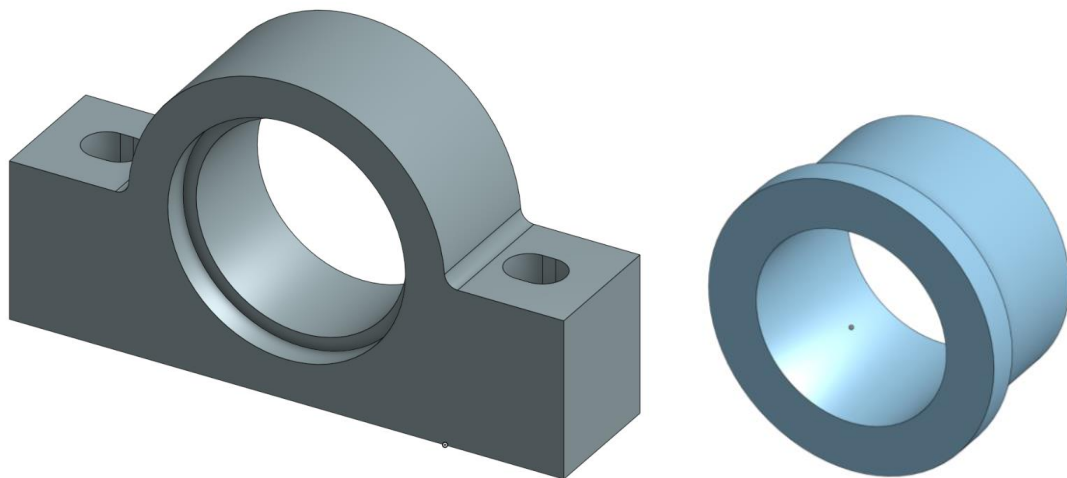


*Figure 71: 3D models of the roll shaft's adjustable bearing block and bushing (OnShape model)*

The bushes expected to be subjected to the stresses most likely to cause failure are those supporting the roll shafts, with the force most likely to cause failure being the roll separating force due to the powder rolling process. This force will induce a stress in the bush tending to crush it against the bearing housing, as shown in Figure 72.
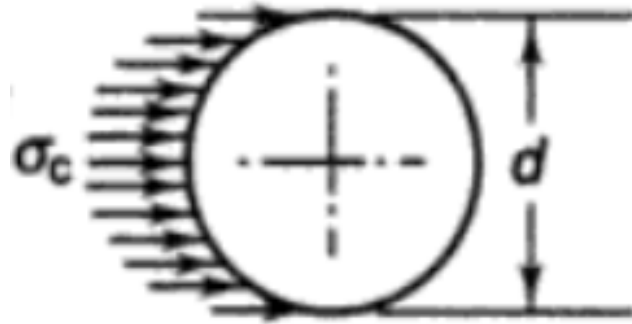


*Figure 72: Bearing stress on the roll shaft bush caused by the roll separating force [78]*

The stress on each roll shaft bush is given by the equation below.

$$\sigma_{bearing} = \frac{F_{roll\ separating}}{A_{projected}} = \frac{214500N/2}{(0.08mx0.05m)} = 26.8MPa$$

The stress in the bearing material is less than the strength of the vesconite from which it is machined (i.e. 30MPa) – the bearing design is thus deemed suitable.


### 4.4.7. Drive System

The worm and gear system designed and manufactured in 2017 [70] was used for this mill. The drive system assembly, including the AC motor, worms, gears, rolls (on the same shafts as the gears), bearings, and couplings, is shown in Figure 73. This design will be reviewed in Section 4.5.3.
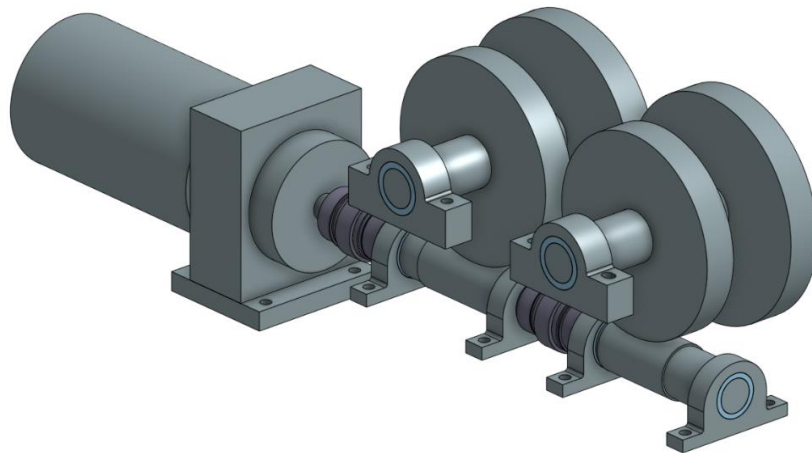


*Figure 73: 3D model of drive system assembly (OnShape model)*

### 4.4.8. SPS System

*Process sequencing*

Since the project combines two distinct processes, it was important to determine the proper sequencing of each of these processes. The best process continuity would have been achieved if the electric current for SPS was applied while the powder was being consolidated into strip through DPR (i.e. simultaneous DPR and SPS via a one-step process). Powder welding to the surface of the rolls if DPR and SPS were performed simultaneously was of some concern. It was also expected that the rolling speeds required for efficient DPR would be higher than those required for effective SPS. This is because relatively high roll speeds are required for wider strips formed during DPR, while relatively low speeds are required to allow for sufficient time for consolidation during SPS. This is discussed further in Section 4.6.4. and Chapter 6. The system was thus designed such that, as an alternative to the one-step process above, the powder can be first rolled into a green strip, then sintered via SPS (i.e. sequential DPR and SPS via a two-step process). This can be done through two separate sets of rolls, but the use of a single set of rolls for both DPR and SPS was more cost effective during this experimental work, and allowed for testing of both processes simultaneously as discussed above. Initial testing of the mill sought to first ensure that each of the processes could be conducted independently, thereafter attempted simultaneous (one-step) application of the processes.

As this project was successful with the sequential process flow, it forms a good foundation for a process utilising two separate sets of rolls, thus potentially forming a completely continuous two-step industrial process for the rolling and sintering of titanium sheet.

*Carbon brush design*

A carbon brush is a sliding contact which can be used to transmit electricity from a static part (the SPS supply circuit) to a rotating part (the compacting rolls). There are certain considerations to be made when designing selecting a suitable carbon brush – these include mechanical, electrical and environmental considerations.

The chief mechanical consideration was that of proper contact between the carbon brush and the rotational element. Naturally, the behaviour at this interface should be well managed to prevent damage to the brush or the rolls while ensuring good transmission of electricity across the contact area. A spring is usually used to ensure good seating of the brush, with a recommended spring pressure in the order of a few hundred grams per square centimetre. The clearance between brush holder and brush should also be carefully designed to ensure the brush does not get stuck nor come loose during operation.

Electrical considerations include the electrical resistivity of the carbon (which in turn contributes to the voltage drop across the brush), as well as the carbon density and distribution within the brush. The resistivity should be low enough to ensure good electrical conduction through the brush without a sizeable voltage drop. The current density should be controlled to ensure operation within the specifications of the particular material being used. For a given total current to be transmitted and electrical resistivity of the brush material, this control can be achieved through brush sizing and number of brushes.

The current density is given by the following equation, where J is the current density, I is the total current being transmitted, A is the cross-sectional area per brush and N is the number of brushes per roll:

$$J = \frac{I}{A \times N}$$

Dust is one of the most important environmental factors to be controlled, as it can cause premature damage to the carbon brushes and the rolls. Between powder compaction and electrical sintering, it is of utmost importance to ensure that all powder is cleaned from the machine, especially the roll surfaces, and that the carbon brushes are well placed to avoid premature wear to their surfaces.

There are several different carbon brush grades available, with each manufacturer using custom material blends and processes to provide optimal solutions for a variety of applications.

When selecting a material for the brushes, the following criteria was used:

1. Low hardness/abrasiveness (to prevent damage to the rolls)

2. Low surface friction (to limit wear of the brushes and rolls, and heat generation)

3. Low resistivity (as we are working with low voltages and wish to reduce voltage drops)

4. High current density (due to the high total current being transmitted)

5. Low cost (to limit cost of the overall system)

Several available materials met these criteria. A local manufacturer capable of machining the carbon brushes to specification was selected, and a suitable material from their product offering chosen. The properties of this material are shown in Table 10.

*Table 10: Carbon brush material properties, grade CG3355, ElectroGraphite*

| PROPERTY | VALUE | | | |
|---|---|---|---|---|
| MATERIAL CLASSIFICATION | CARBON-BONDED METAL GRAPHITIC | | | |
| SPECIFIC RESISTANCE | 800 | | | $\mu\Omega.cm$ |
| CURRENT DENSITY | 12 | | | A/cm² |
| PERIPHERAL SPEED | 35 | | | m/s |
| SHORE HARDNESS | 22 | / | 25 | Module D |
| MICA UNDERCUT | YES | | | Yes/No |
| COEFFICIENT OF FRICTION | 0.15 | ~ | 0.20 | $\mu$ |
| VOLTAGE DROP | 1.8 | ~ | 2.5 | mV |
| SPECIFIC DENSITY | 2.25 | | | g/cm³ |
| METAL CONTENT | 30 | | | % |

Since the compaction and sintering may be carried out in two separate steps, the interface of the SPS system with the DPR system was designed such that the SPS system can be easily removed from and reconnected to the DPR system as necessary. The pathway connecting the current supply to the compact should provide as little resistance as possible. To this end, contrary to the SPS-DPR system design in 2017 [70] which applied current to the roll shafts (and encountered resistance between the couplings connecting the rolls to the roll shafts), this system was designed to apply current directly to the rolls. The carbon brushes are mounted on the flat surface of the rolls.

The large current generated by the supply required a large cross-sectional area for conveyance, to avoid cable damage. Multiple cables were used for transfer of the electric current from the supply to the rolls, in order to avoid having to use very thick cables which would have been unwieldy. A suitable general welding cable of 95mm² cross-sectional area was selected for this purpose. Two of these cables were connected in parallel to a single carbon brush on each roll.

The carbon brush assembly mounted on each roll for transmission of the SPS current, and its position on the mill, is shown in Figure 74. Note that the cables connected to the brushes are not shown here.
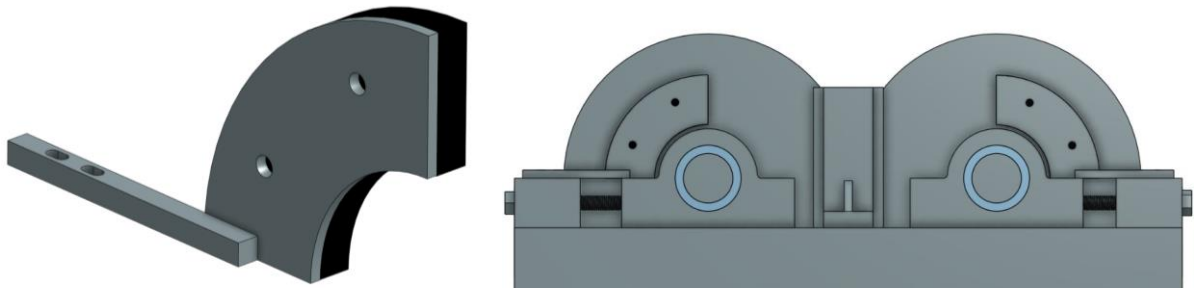


*Figure 74: 3D model of carbon brush assembly and its position (OnShape model)*

### 4.4.9. Design Iterations

The design of the frame was iterative in that as the finite element analysis was performed, areas of weakness were identified and corrected in order to arrive at an acceptable solution. Other aspects were also changed as the design matured, to optimise it electrically and improve usability of the mill. A very early iteration of the mill was characterised by the following:

1. The frame design consisted of 50mm square billet for all frame members

2. The frame was to be mounted on an existing platform above the ground.

3. The cheek plates had corresponding wear surfaces mounted onto the rolls.

4. The carbon brushes used for application of the SPS current to the rolls were placed radially on the rolls.

The 3D model of this early iteration is shown in Figure 75.
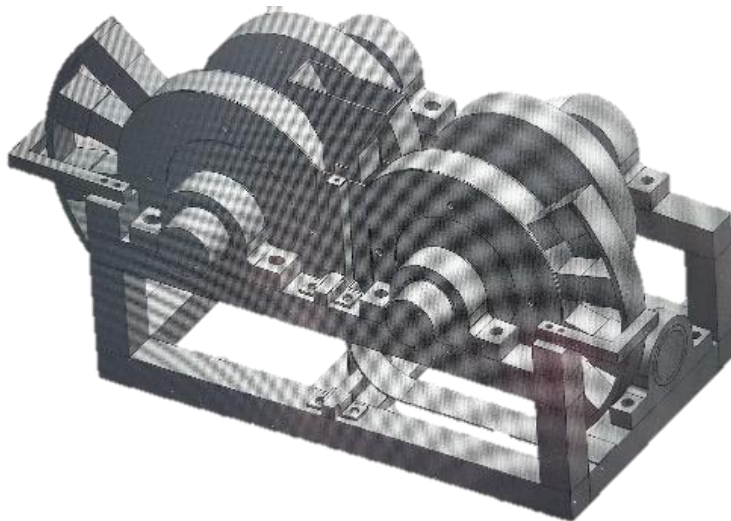


*Figure 75: An early version of the rolling mill design (Siemens NX model – higher resolution image no longer available)*

The following changes were made to this early iteration to arrive at the final solution:

1. To ensure that the frame stress and deformation did not exceed the yield strength of the material and the desired deformation thereof (respectively), the model was subsequently modified, based on FEA analysis discussed in Chapter 4, to use 80mm and 60mm square frame members, with additional members being added.

2. The frame was changed such that the mill would be a standalone unit, placed directly on the ground.

3. The wear plates on the rolls for the cheek plates were removed as they added complexity to the mill and would not be required for the duty cycle expected of the mill.

4. The position of the carbon brushes for application of the SPS current was changed such that the current would be applied to the flat surface of the roll, and not the actual rolling surface, due to premature wear issues expected from any titanium powder residue present on the rolling surfaces. The result of this decision is discussed in Section 6.3.1.

### 4.4.10. Final 3D Model

Once the preliminary design was completed, the frame of the mill was strength tested using Siemens NX, as will be described in the Section 4.5. Changes to the design were made as necessary, and the final model was thus developed.

Renderings of the final fully assembled 3D model are shown in Figure 76. These renderings illustrate all components as modelled using OnShape, including the frame, the drive system (most of which had already been manufactured but had to be drawn in to confirm all positions and ensure the mounting points were correct), the bearings, the screw adjustment mechanism for the rolls, the auxiliary mechanical components such as the cheek plates, hopper and exit slide, and the carbon brush assemblies.
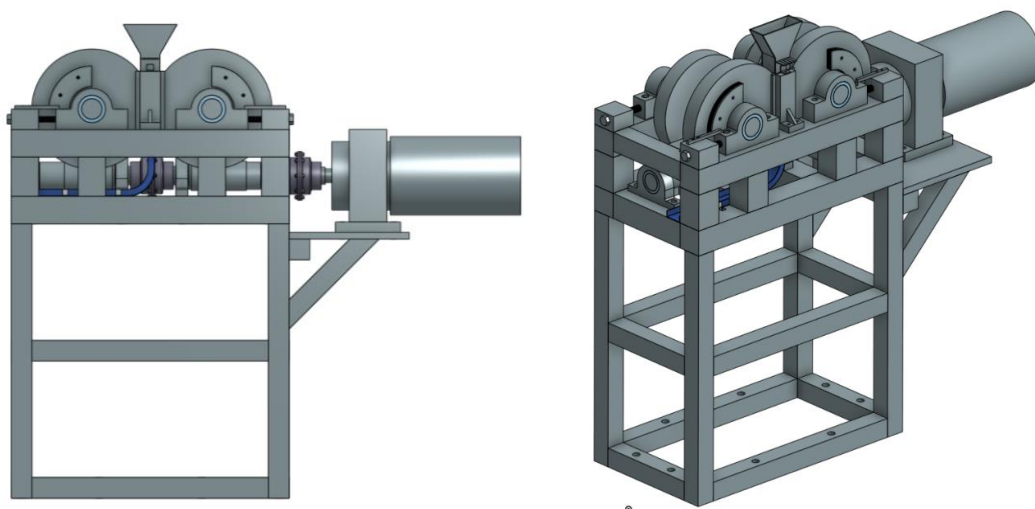


*Figure 76: Renderings of the SPS-DPR mill assembly (OnShape model)*

A full set of manufacturing drawings is available in digital form on the CD submitted together with this dissertation.

## 4.5. Finite Element Analysis (Siemens NX)

This section will describe the modelling of the structural behaviour of the rolling mill components under load. This is done to ensure that the stresses and deformation of the frame and its components are within acceptable limits, and that mechanical failure does not occur during operation.

### 4.5.1. Overview

Linear static finite element analysis has been used to simulate the behaviour of the mill during operation. Three models were used in this analysis. The first model consists of the various members which make up the frame. The second model consists of the rolls with shafts, bearing blocks supporting the roll shafts, and bushings located between the roll shafts and bearing blocks. The third model is of the cheek plates situated on either side of the roll gap. These three completely separate models were selected for analysis as they represented the only components expected to experience appreciable loading during operation.

The frame was constructed from EN8 steel. The rolls have been manufactured from EN19 carbon steel. The bearings blocks, roll shafts and cheek plates are mild steel. The bushings are to be machined from vesconite. The weight of the frame is 570kg; reduction of the machine weight through optimisation of material usage was not a consideration for this particular design.

### 4.5.2. Rolling Mill Frame Model

*Boundary conditions*

The frame was fixed to the ground via high tensile fasteners at eight points along the frame members in contact with the ground. Initially, boundary conditions at these points were approximated as fixed constraints. Since the simulations indicated that they were far enough away from the loading to not have an appreciable effect on the results (as evidenced by the stresses in the regions surrounding the constraints), this approximation was used in the final model. The points at which the model is fixed are shown in Figure 77.
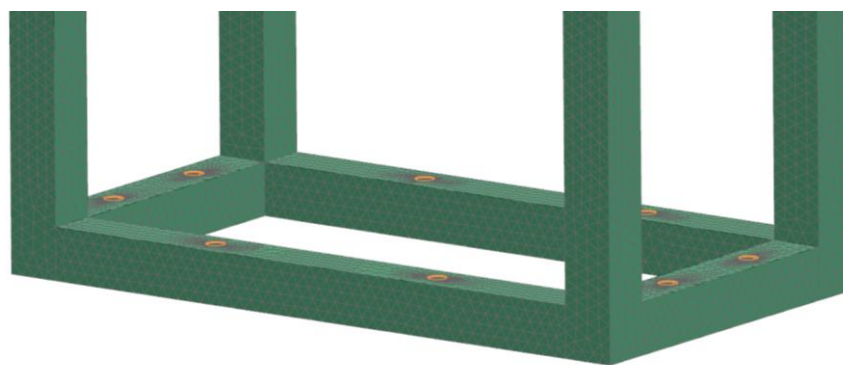


*Figure 77: Frame boundary conditions (Siemens NX model)*

To model the welded connections between the frame members, each member to be welded was first sectioned such that only the area to be welded was in contact with the face to which it is welded (via 10mm all-round bevel-groove welds). Mesh mating was then applied to all coincident faces of the frame members. This should give a reasonable approximation of the welded connections in the model. Advice on this method of modelling the welded connections was sought from an expert in the field of finite element modelling.

*Loading conditions*

The primary loading on the frame is from the roll separating force which tends to push the rolls apart during operation of the mill, which is a direct reaction to the force compacting the powder during rolling. This force was determined through simulation of the rolling behaviour in MATLAB using the Johanson model, as described in Section 4.3.5. The variables required for the rolling behaviour simulation included the titanium powder characteristics of compressibility, internal friction angle, and wall friction angle, all of which were determined experimentally using equipment at UKZN's Civil Engineering Lab as described in Section 3.

It was determined through the MATLAB model in Section 4.3.5. that the roll separating force is 214.5 kN and the roll torque is 963 Nm (per roll), for a maximum desired density of 81.25% in a single pass – these applied loads were used in the FEA model as they represent the worst case loading scenario that is expected for the mill.

The load distribution to each bearing point was then determined based on the distance of each bearing to the point of application of the roll force, as per the equations listed below, and the loads were applied accordingly as forces at the bearing positions.

*Equation 17: Bearing reaction force [79]*

$$F = \frac{Pab^2}{L^2}$$

*Equation 18: Bearing reaction moment [79]*

$$M = \frac{Pb^2(3a+b)}{L^3}$$

The other loading elements on the frame are the weight of the frame and mounted components, which were applied as a gravitational load and vertical forces, respectively; the output torque from the motor transferred to the motor mounting points; the force tending to push the cheek plates apart during rolling when the strip width equals the roll width; and the worm and gear forces (axial, tangential and radial), which were calculated using gear equations and transferred as forces on the worm and gear bearing mounting points accordingly. The equations used to calculate the gear forces are listed below. For the equations below, $T_w$ is the input torque to the worm in Nm, $d_w$ is the worm diameter in metres, $\phi_n$ is the normal pressure angle in degrees, $\lambda$ is the lead angle in degrees, and f is the coefficient of friction between the worm and gear. All forces calculated below are in Newtons.

*Equation 19: Worm tangential force; gear axial force*

$$F_{wt} = F_{ga} = \frac{2T_w}{d_w}$$

*Equation 20: Worm axial force; gear tangential force [80]*

$$F_{wa} = F_{gt} = F_{wt} \frac{\cos\phi_n \cos\lambda - f\sin\lambda}{\cos\phi_n \sin\lambda + f\cos\lambda}$$

*Equation 21: Worm radial force; gear radial force [80]*

$$F_{wr} = F_{gr} = F_{wt} \frac{\sin\phi_n}{\cos\phi_n \sin\lambda + f\cos\lambda}$$

Based on the maximum torque that the motor can output, the following worm and gear forces were calculated:

1. $F_{wt} = F_{ga} = 1.7$ kN

2. $F_{wa} = F_{gt} = 7.0$ kN

3. $F_{wr} = F_{gr} = 2.6$ kN

The application of all expected loading on the model is shown in Figure 78.
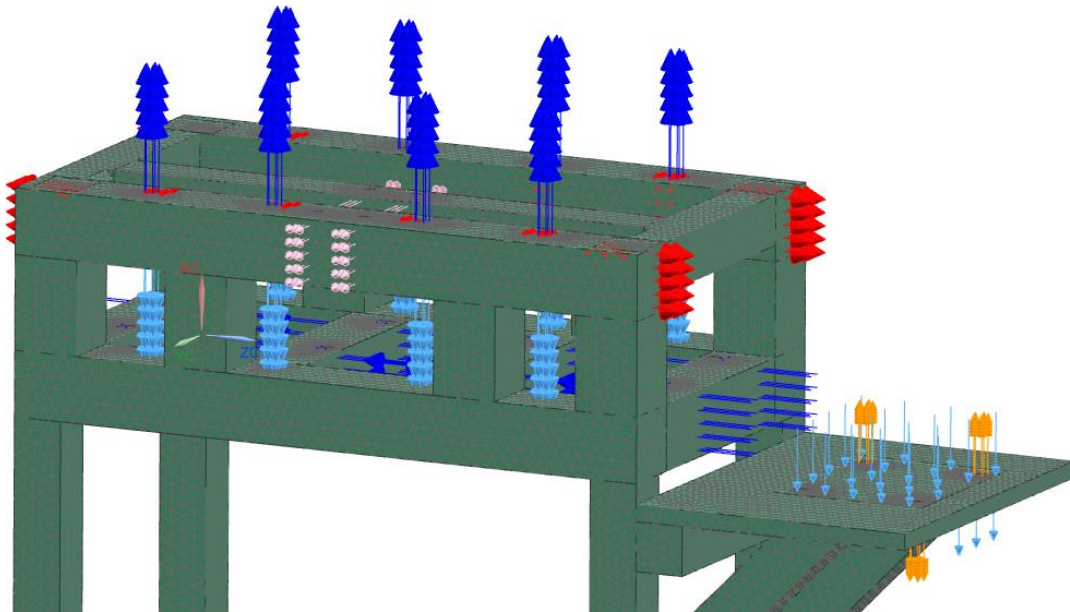


*Figure 78: Frame loading conditions – loading not shown to scale (Siemens NX model)*

As discussed, this loading on the frame model includes:

1. The roll separating force (shown in red on the figure above)

2. The weight of all components (shown in light blue on the figure above)

3. The weight of the frame itself (not shown on the figure above)

4. The torque from the motor (shown in orange on the figure above)

5. The force of the powder on the cheek plates (shown in pink on the figure above)

6. The worm and gear forces (shown in dark blue on the figure above)

As noted in Section 4.3.5., the actual torque expected for compaction of the titanium powder was 963 Nm per roll, which equated to 37 Nm output torque from the motor (the motor torque is equally spilt between the two rolls, with a worm/gear ratio of 52:1). The use of the maximum torque output from the motor when calculating the worm and gear forces was thus conservative as this loading is unlikely to occur during normal compaction. It can also be seen that the effect of the loading due to the worms and gears is far less than that due to the roll force from the powder compression.

*Running the simulation*

The FEA model was set up with the 3D solid model of the frame generated in Siemens NX. Rolled steel was selected as the material used for the model, and the boundary and loading conditions were set up as described above.

The simulation was conducted with gradually finer meshing until mesh independence of the model was found. Upon mesh independence, the finest mesh size was used due the model running efficiently at that size. In order to achieve the desired results efficiently, a large mesh size was initially used for the entire model, to identify areas of interest (typically areas of high stress concentrations, such as the bolt holes and sharp edges). The relatively coarse mesh was then kept for the bulk of the model, with areas of interest refined for accurate results. This allowed for a good balance between accuracy of results and amount of time taken to solve each simulation.

The fully meshed frame, and the refined mesh at the bolt holes, are shown in Figure 79.
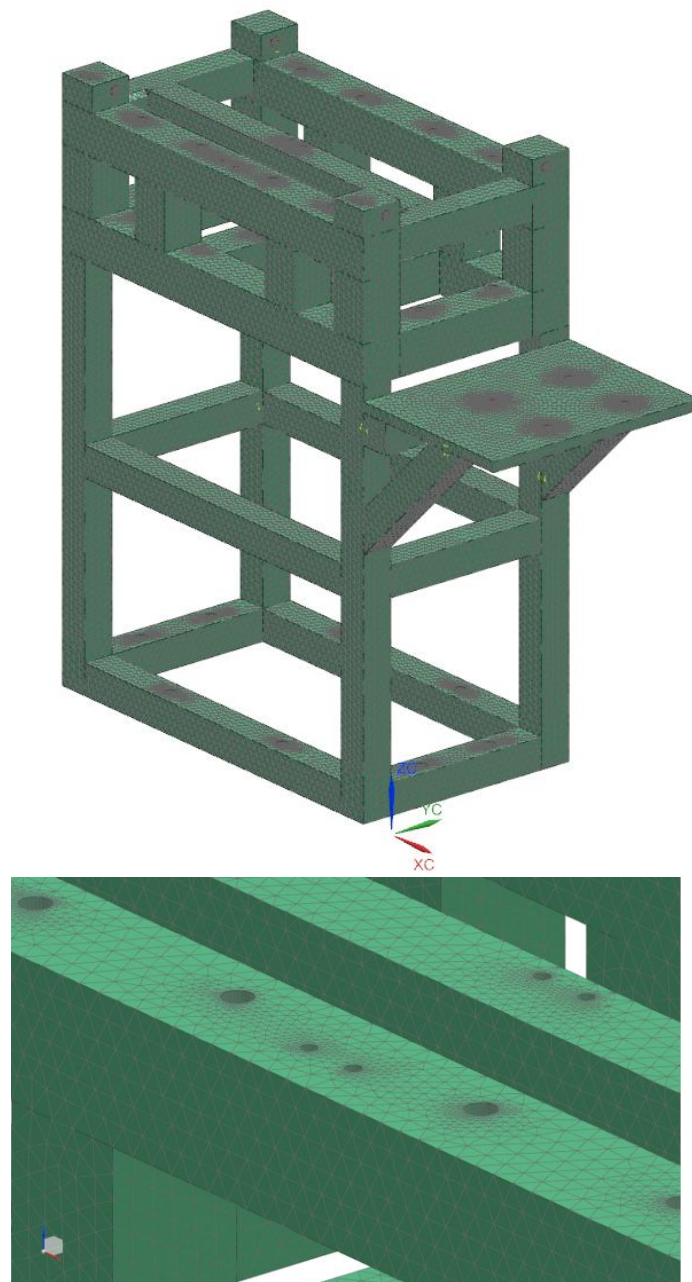


*Figure 79: Refined mesh on frame (Siemens NX model)*

87

*Results*

When the frame was modelled on its own (with all loading transferred to the bearing points), the result was a maximum stress of 189 MPa, and a maximum deformation in the roll gap dimension of 0.08 mm.

The stress on the frame under expected loading during mill operation is shown in Figure 80.
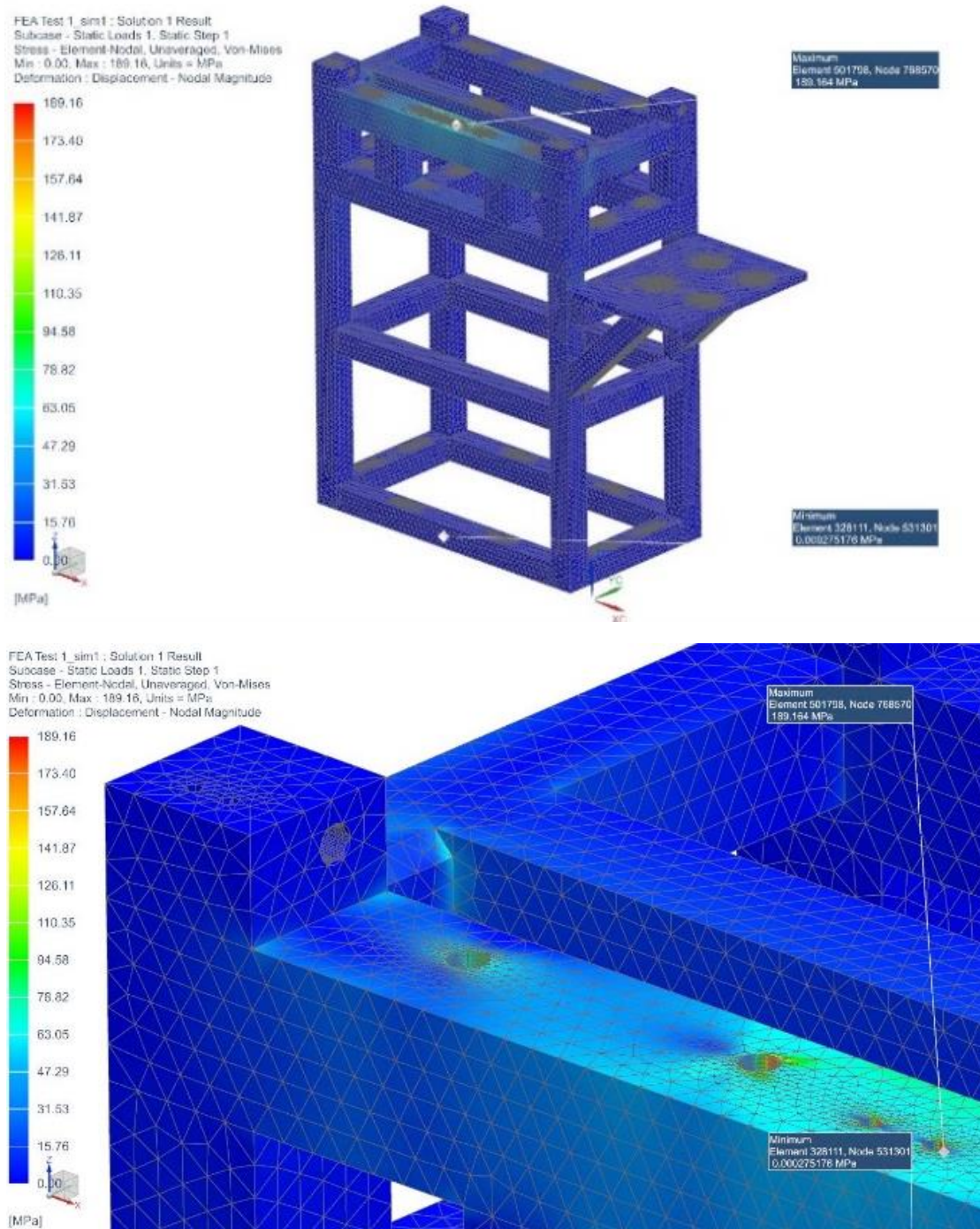


*Figure 80: Simulated stress on frame (Siemens NX model)*

The deformation of the frame under expected loading during mill operation is shown in Figure 81.
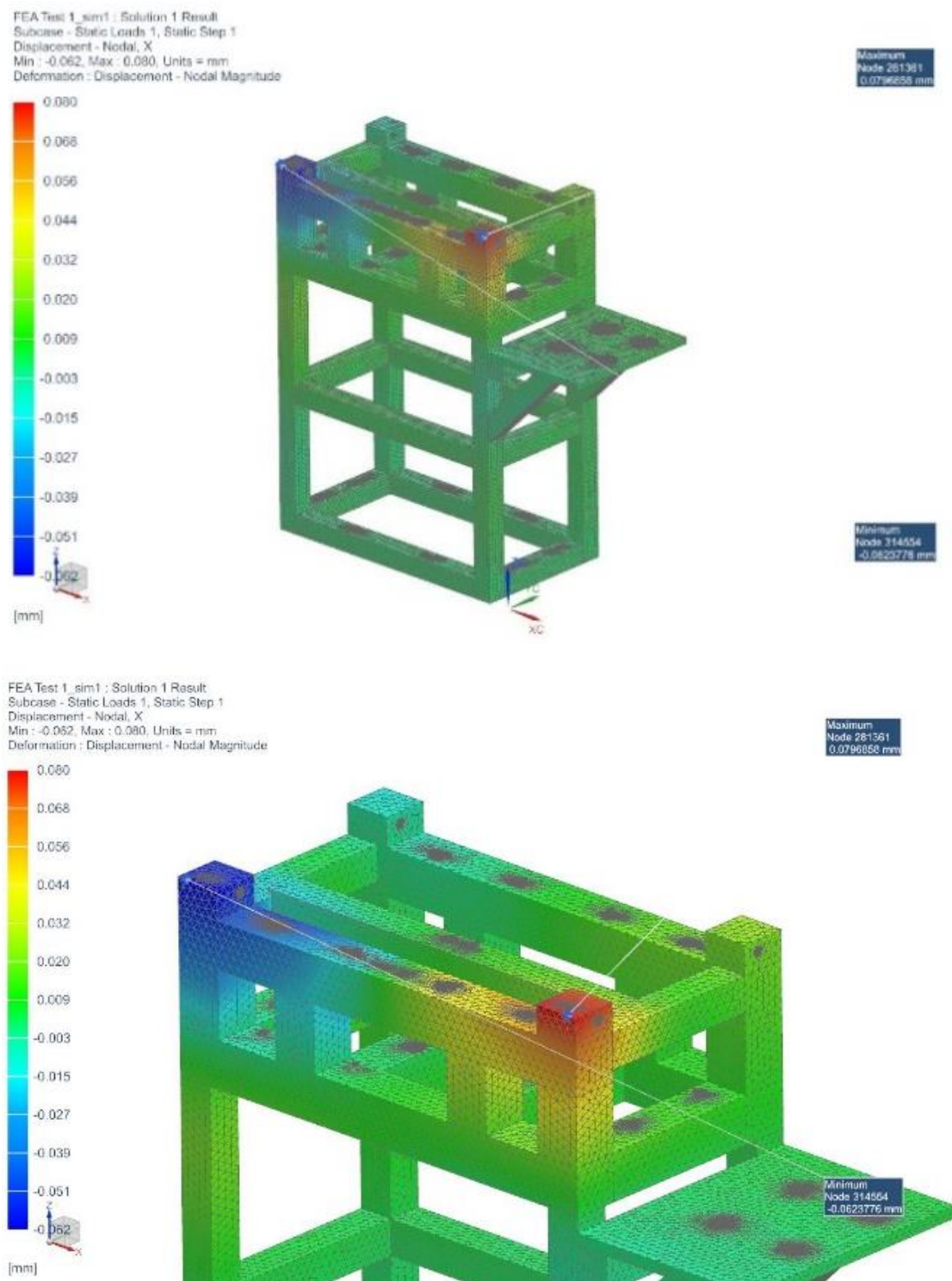




*Figure 81: Simulated deformation on frame (Siemens NX model)*

### 4.5.3. Rolls, Shafts and Bearings Model

To ensure that the rolls, shafts and bearings were suitable for the application, these were modelled separately.

For this model, the boundary conditions were applied as fixed constraints at the bearing housing bolt holes, and the roll separating force was applied at the minimum roll gap in the direction tending to push the rolls apart.

The mesh refinement followed the same process as for the frame. The fully meshed model is shown in Figure 82.
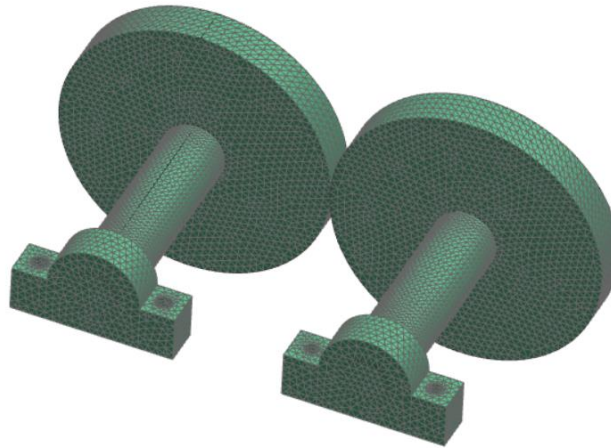


*Figure 82: Refined mesh on rolls, shafts and bearings (Siemens NX model)*

The simulation was solved, and the components then isolated to better view the stresses and deformation of each. When these components were modelled, the result was a maximum stress of 193 MPa, and a maximum deformation in the roll gap dimension of 0.121 mm. The maximum stress on the model was on the shafts at the position where the rolls are attached, and the maximum deformation was on the rolls. The stress and deformation of each of the components of this model are shown in the figures below.

The stress and deformation on the rolls are shown in Figure 83.

Frame for FEA Copy 1_step_sim1 : Solution 2 Result
Subcase - Static Loads 1, Static Step 1
Stress - Element-Nodal, Unaveraged, Von-Mises
Min : 0.01, Max : 192.59, Units = MPa
Deformation : Displacement - Nodal Magnitude

Maximum
Element 63875, Node 44016
111.853 MPa

111.85
102.63
93.40
84.18
74.96
65.73
56.51
47.28
38.06
28.84
19.61
10.39
1.16
[MPa]

Minimum
Element 58824, Node 102717
1.16363 MPa

Frame for FEA Copy 1_step_sim1 : Solution 2 Result
Subcase - Static Loads 1, Static Step 1
Displacement - Nodal, X
Min : -0.120, Max : 0.121, Units = mm
Deformation : Displacement - Nodal Magnitude

Maximum
Node 90301
0.12065 mm

0.121
0.101
0.081
0.061
0.041
0.021
0.001
-0.019
-0.039
-0.060
-0.080
-0.100
-0.120
[mm]

Minimum
Node 125671
-0.119552 mm

*Figure 83: Top to bottom: Stress and deformation on rolls (Siemens NX model)*

The stress and deformation on the roll shafts are shown in Figure 84.

Frame for FEA Copy 1_step_sim1 : Solution 2 Result
Subcase - Static Loads 1, Static Step 1
Stress - Element-Nodal, Unaveraged, Von-Mises
Min : 0.01, Max : 192.59, Units = MPa
Deformation : Displacement - Nodal Magnitude

192.59
176.56
160.53
144.50
128.47
112.44
96.41
80.39
64.36
48.33
32.30
16.27
0.24
[MPa]

Maximum
Element 44388, Node 67449
192.589 MPa

Minimum
Element 47749, Node 88455
0.24041 MPa

Frame for FEA Copy 1_step_sim1 : Solution 2 Result
Subcase - Static Loads 1, Static Step 1
Displacement - Nodal, X
Min : -0.120, Max : 0.121, Units = mm
Deformation : Displacement - Nodal Magnitude

0.113
0.094
0.075
0.056
0.038
0.019
0.000
-0.019
-0.037
-0.056
-0.075
-0.094
-0.113
[mm]

Maximum
Node 43857
0.112665 mm

Minimum
Node 70336
-0.11252 mm

*Figure 84: Top to bottom: Stress and deformation on roll shafts (Siemens NX model)*

The stress and deformation on the bushings are shown in Figure 85.
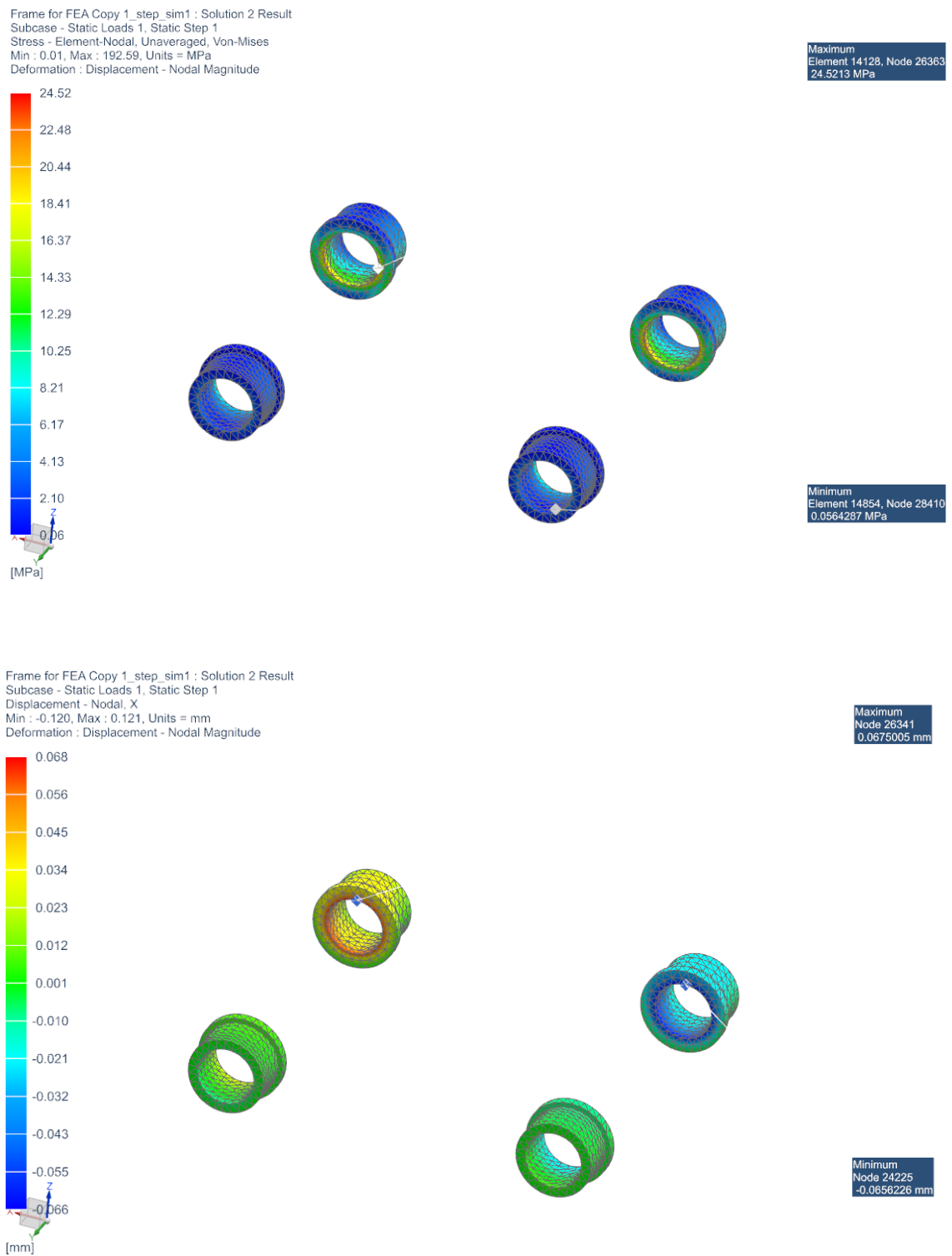


Figure 85: Top to bottom: Stress and deformation on roll shaft bushings (Siemens NX model)

The stress and deformation on the bearing housings are shown in Figure 86.
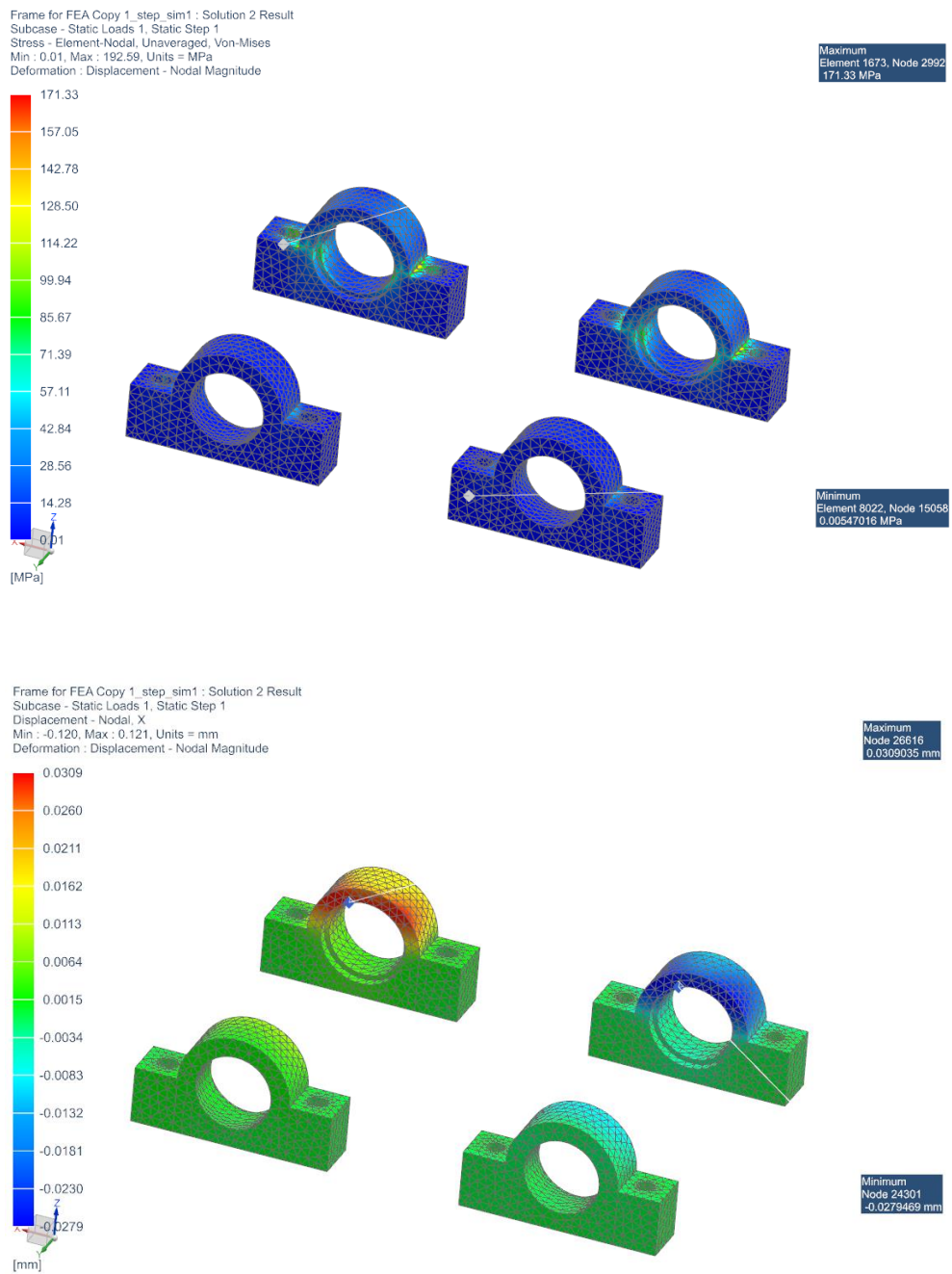


Figure 86: Top to bottom: Stress and deformation on roll shaft bearing blocks (Siemens NX model)

### 4.5.4. Cheek Plate Model

The cheek plates were modelled separately as there are significant forces expected on them during rolling when the strip width equals the roll width.

The cheek plate analysis was performed with fixed constraints modelled at the bolt holes, and a force applied horizontally, at the level of the minimum roll gap. The boundary conditions and loading conditions for the model are shown in Figure 87.
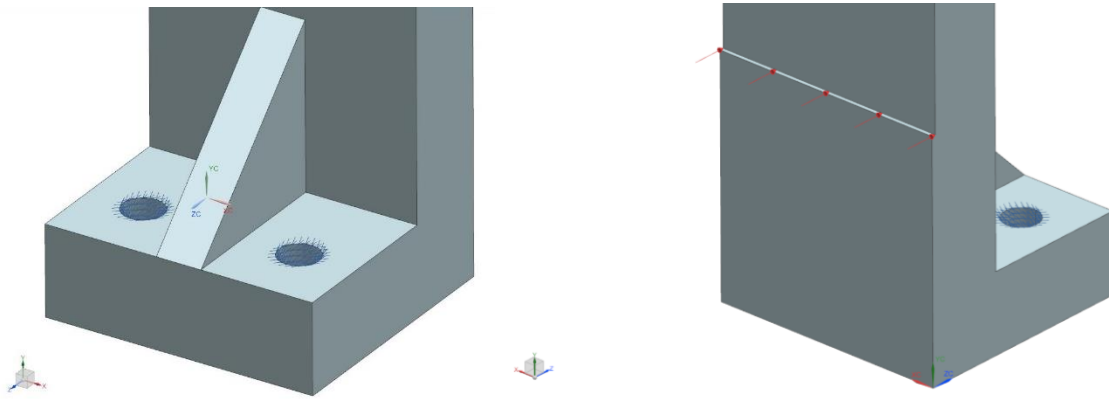


*Figure 87: Boundary and loading conditions on the cheek plate (Siemens NX model)*

The cheek plate design was modified subsequent to the initial analysis thereof, until the expected stress and deformation on these components was at an acceptable level. The initial design indicated a maximum stress of 2433 MPa, and a maximum deformation of 12.06mm, which were clearly far beyond the capabilities of the material and the desired point of operation. This initial model is shown in Figure 88.
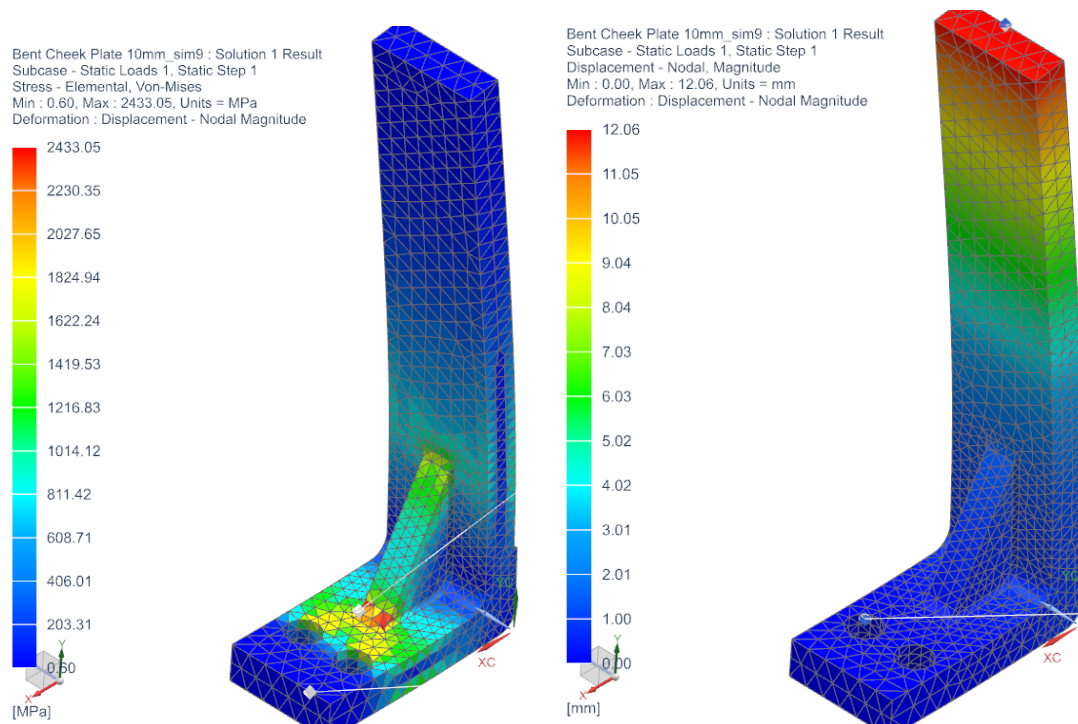


*Figure 88: Left to right: Stress and deformation of initial cheek plate design (Siemens NX model)*

With the final iteration of the cheek plate design, incorporating thicker material and better placement of the strut for stiffening, the result is a maximum stress of 200 MPa and a maximum deformation of 0.216 mm. This is shown in the following figures.

The stress on the cheek plate is shown in Figure 89.
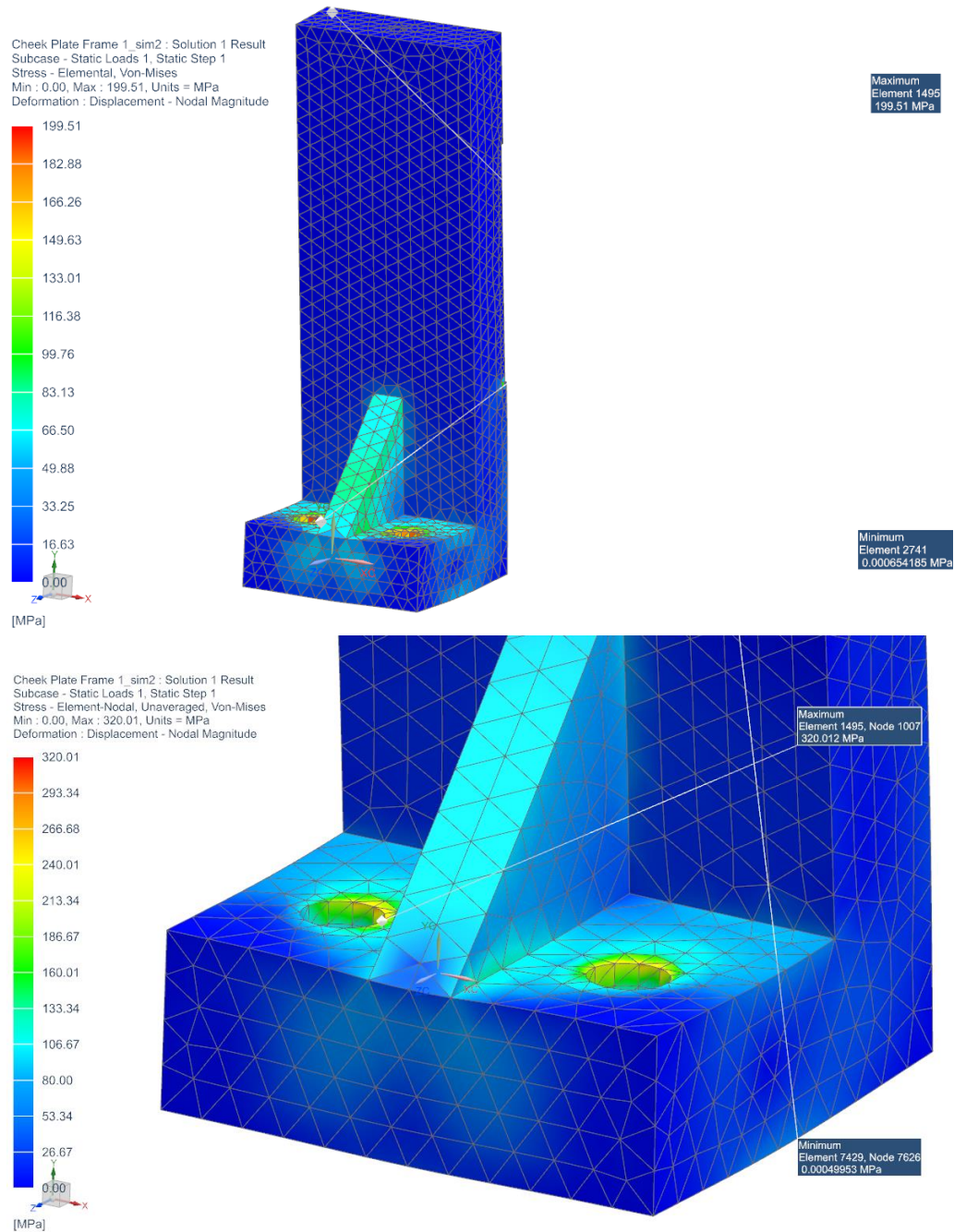


*Figure 89: Stress on final cheek plate design (Siemens NX)*

The deformation of the cheek plate is shown in Figure 90.
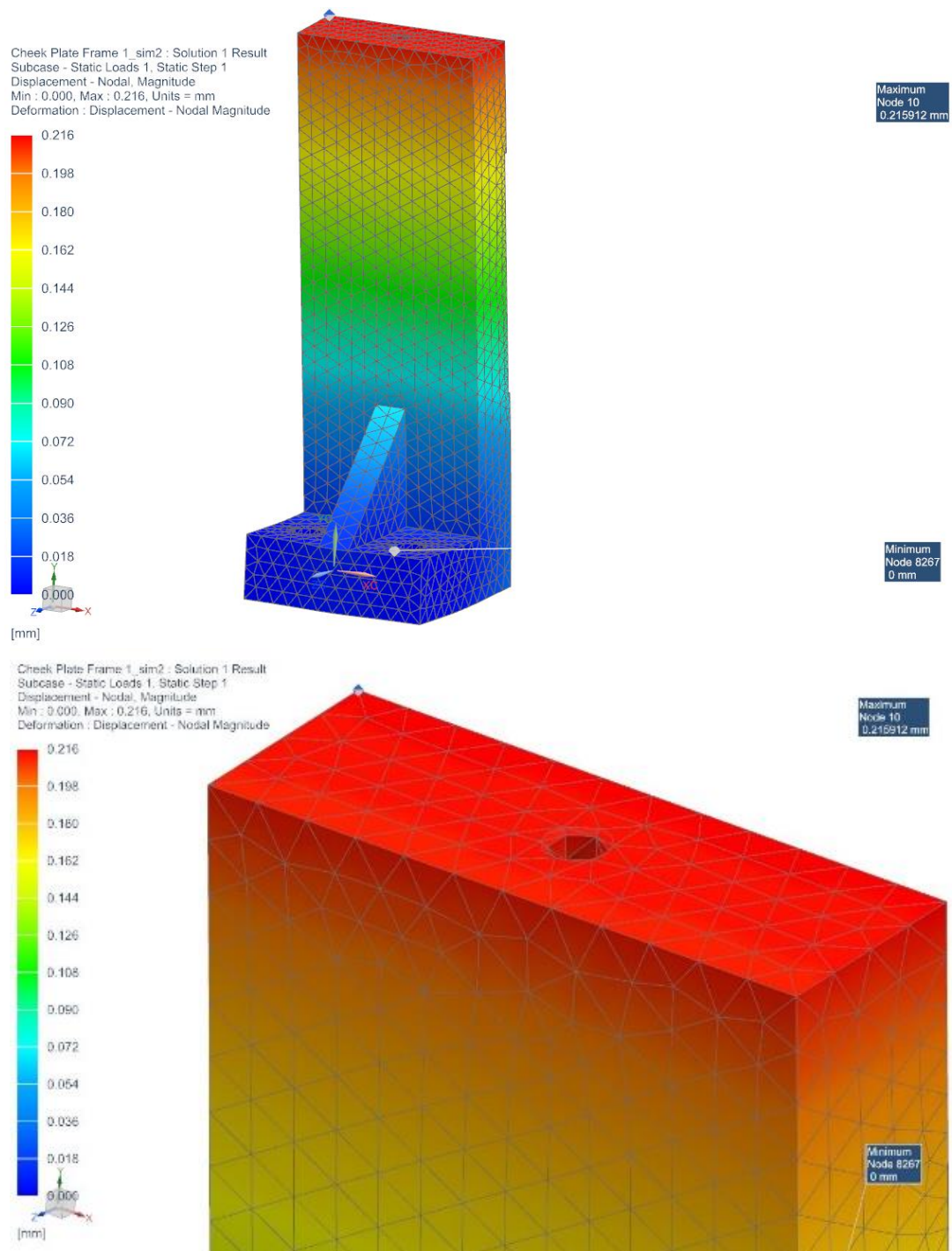


*Figure 90: Deformation of final cheek plate design (Siemens NX model)*

Once again, the maximum stress occurred at the bolt holes, and the stress on the bulk material was far below the material's yield strength. At the level of the minimum roll gap, the deflection was less than 0.1mm, which will result in some material loss from the sides of the rolls, but is considered acceptable for the intended purpose.

### 4.5.5. Discussion

Simulations were all performed using mesh densities that were gradually refined until mesh independence was observed. To reduce computing times and increase efficiency of the solution, higher density meshes were applied to the areas which were noted in initial simulations to have higher stresses than the bulk of the model, notably the bolt holes.

The maximum Von Mises stress of 189 MPa on the frame model, 193 MPa on the rolls, shafts and bearings model, and 200 MPa on the cheek plate model were all below the 250MPa yield strength of the respective materials. These maximum stresses were also highly localised – for the frame, localised to the bearing housing bolt holes; for the rolls, shafts and bearings model, localised to the contact area between roll shafts and rolls; and for the cheek plates, localised to the bolt holes where the cheek plates are fixed to the frame. These localised stresses are to be expected as they are stress concentration points. The bulk of the stress in all three models remained far below the relevant materials' yield points.

The main consideration for the roll deformation was that this deformation should not adversely affect the rolling process. Thus, the displacement in the direction tending to push the rolls apart was the primary concern. This displacement was found to be minimal (at well under 10% of the target roll gap of 1.6mm), which was important as a significantly varying roll gap during operation would result in a strip with an inconsistent thickness along its length, though this variation would be expected to be only a fraction of the total displacement.

The maximum stress and deformation on these models were thus deemed acceptable.

## 4.6. Spark Plasma Sintering Circuit (Simulink)

This section will explore the various circuits considered for providing a sintering current to the sample, discuss the merits of each circuit, and determine the optimal circuit for the application.

### 4.6.1. Expected Circuit Resistance

In designing the SPS circuit, one of the experiments conducted for the 2017 SPS-DPR project [70] was referred to. In this experiment, the group used a transformer to step down an AC voltage source, then applied this voltage to the mill rolls using carbon brushes connected to the roll shafts. The rolls were stationary during the experiment, and a metal test piece was inserted into the roll gap to simulate a compacted strip. The current and voltage on the primary and secondary of the transformer were recorded. Using their recorded values for voltage and current on the secondary, and the relationship below, the minimum and maximum circuit resistance were calculated as 3 mΩ and 4 mΩ respectively.

*Equation 22: Relationship between resistance, voltage and current*

$$R = \frac{V}{I}$$

The experiment conducted by the group in 2017 will not give an exact value for the expected resistance in our circuit, as the point of application of the current will differ, and because they did not use a titanium compact in their experiment. However, the experiment was expected to give a reasonable approximation of the resistance.

For the purpose of this design, a value of 5 mΩ was used. This was 25% higher than the maximum resistance measured by the 2017 project team. Using this expected load resistance of 5 mΩ and the required current of 1000 A allowed for calculation of the voltage supply necessary for the circuit, i.e. 5 V. It was expected that these would form reasonable baseline values for the design, with the understanding that any significant differences from the expected current of our system (resulting from differences in the actual value of resistance in our circuit) could be corrected through adjustment of the applied voltage to the compact by:

1. Adjustment of the transformer turns ratio (and thus the voltage on the secondary) for an AC input

2. Adjustment of the number of cells in series for a DC input

It is important to note that the value modelled for the resistance across the sample is supported by research conducted previously [81]. The results of this research indicate that the resistance across the sample at the beginning of the SPS process is higher than at the end of the sintering process; interestingly, this resistance was then observed to drop to a constant value of 3 mΩ for different metals by end of the sintering process [81].

### 4.6.2. Circuit Elements

As has been discussed in the literature review chapter, pulsed DC is the most commonly used waveform for SPS. Although the prevalence of pulsed DC in the literature is not proof of superiority over AC, it does at least provide a certain level of security of its efficacy. There is, additionally, sufficient literature available on the parameters governing the use of pulsed DC to enable design of a suitable system for this application.

For the application of pulsed DC to the sample, it was expected that the following elements would be required in the circuit. As will be discussed, a suitable SPS circuit may designed which does not include all these elements.

*Voltage source*

According to the literature reviewed [9] successful SPS can be achieved with direct current or alternating current being applied to the sample. There are thus a few options for the input and output of the SPS circuit: using an AC input and output; using an AC input and converting this to a DC output; or using a DC input and output. For an AC input, 220V single-phase alternating-current power outlets are widely available at the campus. For a DC input, a battery system will need to be sourced.

*Step-down transformer*

Typical SPS systems apply low voltage (and high current) across the sample being sintered. If a high voltage AC power supply is being used, this will need to be stepped down to a lower voltage before being applied to the sample.

Based on the resistance values expected across the load, the exploration of previous research papers on this topic [62] [32], and the requirement for this circuit to be built and tested in a laboratory environment, baseline values of 5V and 1000A were selected for the secondary of the transformer, which equates to a power transmission of 5kVA.

A transformer was designed to convert the input of 230 V, after losses through the diode and a correction factor applied for half wave rectification, to an output of 5 V. A windings ratio of 28 was used (i.e. 28 times as many windings on the primary side of the transformer as on the secondary side). The turns ratio required to achieve this output voltage is calculated as shown below:

$$n = \frac{V_1}{V_2} = \frac{230V}{\left[(5V + 0.8V) \times \sqrt{2}\right]} = 28$$

This means that the windings on the primary side of the transformer must be greater than the windings on the secondary side by a factor of 28.

The size of the transformer core must also be specified in order to ensure that the power being transmitted through it is not high enough to result in saturation. The dimensions of the core proposed for this application are shown in Figure 91; the depth is 100mm.
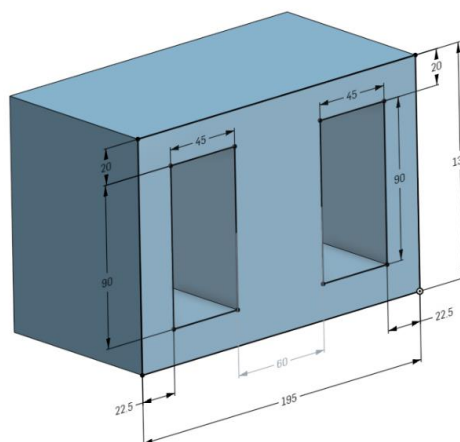


*Figure 91: Transformer core dimensions OnShape model)*

To ensure the core was large enough for the desired power transmission without the core becoming saturated, a calculation was performed to determine the allowable power through the core, as shown below.

*Equation 23: Power handling capacity, transformer core [82]*

$$VA = 10.5 \times J \times B_m \times f \times GF \times A_{Cmin} \times 10^{-7}$$
$$= (10.5)\left(\frac{1.5A}{mm^2}\right)(1.5T)(50Hz)(45mm \times 90mm \times 2)(60mm \times 100mm)(10^{-7})$$
$$= 5.7kVA$$

This value is greater than the power expected to be transmitted across the core (i.e. 5kVA), which means that the designed transformer core may be used without the risk of core saturation.

*Rectification*

Rectification is the process of converting alternating current to direct current. A simple component which can be used for this purpose is a diode, which allows current applied to its input terminal to flow only in a single direction from its output terminal. This results in a single-directional sinusoidal output (i.e. a DC output), if a bidirectional sinusoidal input is applied (i.e. an AC input). For a single diode, the resultant waveform is half-wave rectified DC.

Full-wave rectification can be achieved through the use of a combination of diodes, for example a four-diode bridge.

When using a transformer, there are two options for the circuit rectification – rectifying the current on the primary, or on the secondary. Full wave rectification is more efficient (by a factor of √2), if rectification is done on the secondary. However, if rectification is done on the primary, it is recommended that the current be half wave rectified, since saturation problems are expected if full wave rectified DC is supplied to the primary side of the transformer. It is expected that half wave rectification on the primary will be more cost-effective than full wave rectification on the secondary; from a procurement perspective, rectifiers capable of handling the high current on the secondary are expected to be more expensive and more difficult to source than those rated for the lower current present on the primary. Additionally, more of these high-cost components would be required for full wave than for half wave rectification. Finally, diodes are subject to a voltage drop across them, the effect of which is greater on the low voltage side of the transformer (i.e. the secondary, in this case).

*Smoothing*

The output voltage of the transformer will be sinusoidal. If the effect of pulsed versus continuous smoothed DC on the SPS process is to be observed, a capacitor should be connected in parallel with the circuit load (i.e. the titanium sample) to provide smoothing of the voltage. This will be achieved through the capacitor alternately charging and discharging via the sinusoidal voltage output from the transformer, resulting in a smoothed supply to the load.

*Pulsing*

One of the contributors to the effectiveness of SPS in producing a fully-sintered compact in a short period of time is believed to lie in the pulsing of the current to the compact being sintered. This may be achieved through the use of alternating current, or through on-off switching of direct current. If the effect of pulsed DC on the SPS process is to be observed, a mechanism of switching the current on and off should be implemented. This pulsing mechanism should be placed in the circuit after the current has been smoothed, so as to provide pulsed, smoothed current to the compact.

A gate turn-off (GTO) thyristor is recommended for control the voltage to the compact, with the pulsing governed by an Arduino connected to the gate of the thyristor, which will be programmed using a blink function.

*Application of current to the compact*

A set of carbon brushes was used to transfer the current from the designed SPS supply to the rolls. The green test piece being sintered will be compacted between the rolls during application of the current, as one of the aspects of successful spark plasma sintering is the application of pressure during sintering. The design of the carbon brushes has been discussed in the SPS portion of the 3D design and modelling section, i.e. Section 4.4.8.

### 4.6.3. Proposed Circuits

*Circuit A*

Circuit A employed all the circuit elements discussed above. The circuit diagram as modelled in Simulink is shown in Figure 92.



*Figure 92: Electrical schematic, proposed circuit A (Simulink model)*

The input to this circuit was high voltage AC. The input voltage waveform is shown in Figure 93.
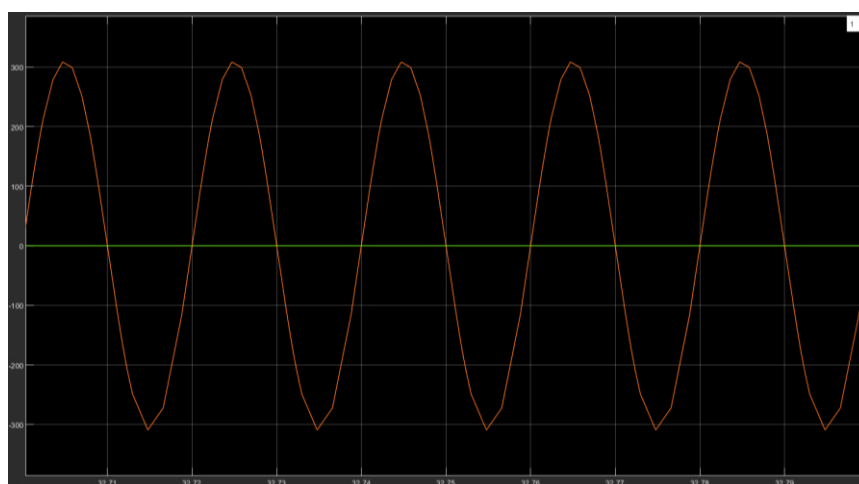


*Figure 93: Input voltage waveform, 50Hz AC (Simulink model)*

The output from this circuit was low voltage, pulsed, smoothed, half-wave secondary-rectified current.

The output current waveform generated from the Simulink simulation for proposed circuit A at a pulsing period of 1s is shown in Figure 94.
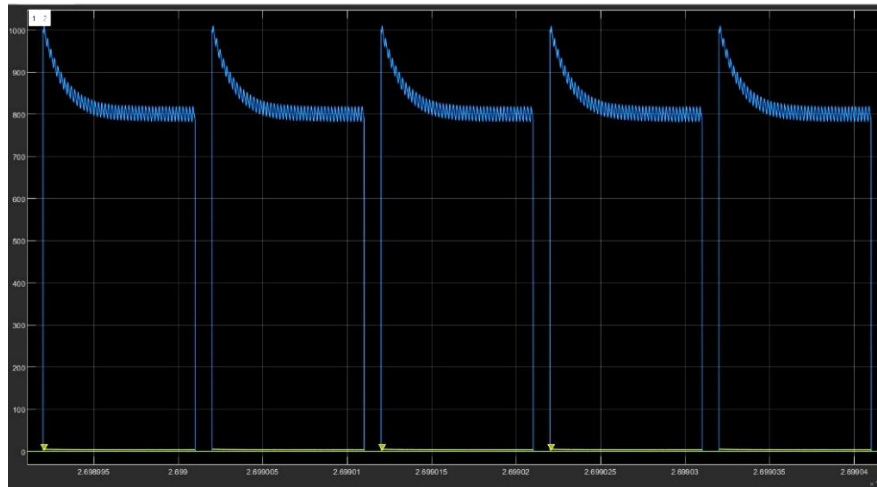


*Figure 94: Output current waveform, proposed circuit A; period 1.0s (Simulink model)*

To determine the effect of the period (the inverse of the wave frequency) of the pulsing on the output waveform, the simulation was run with different frequencies modelled. The results of this are shown in the following figures.

The output current waveform generated from the Simulink simulation for proposed circuit A at a pulsing period of 0.3s is shown in Figure 95.
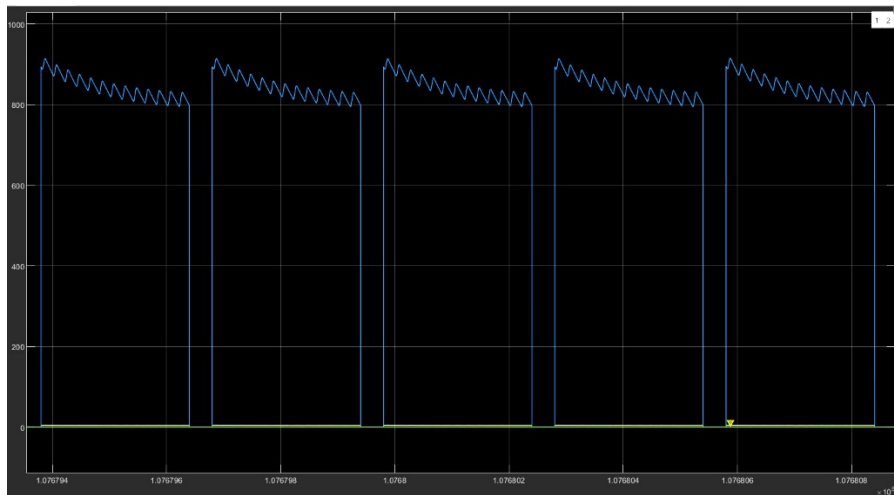


*Figure 95: Output current waveform, proposed circuit A; period 0.3s (Simulink model)*

The output current waveform generated from the Simulink simulation for proposed circuit A at a pulsing period of 0.03s is shown in Figure 96.
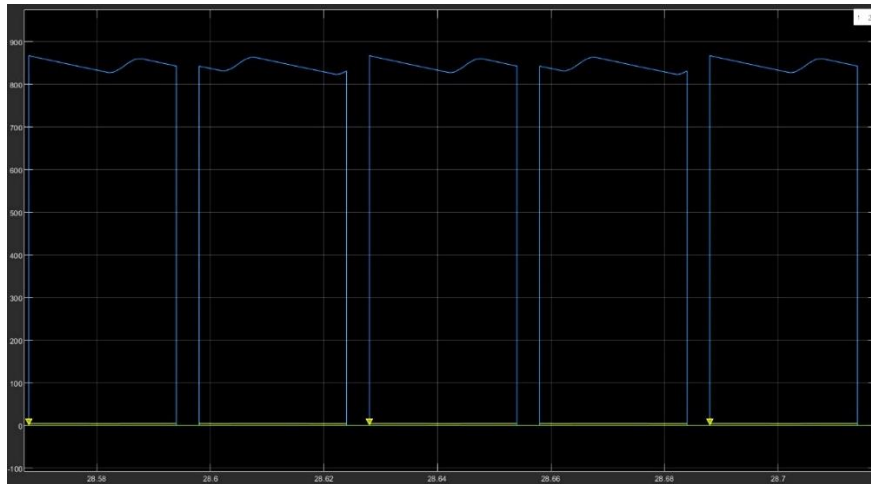


*Figure 96: Output current waveform, proposed circuit A; period 0.03s (Simulink model)*

The output current waveform generated from the Simulink simulation for proposed circuit A at a pulsing period of 0.02s is shown in Figure 97.
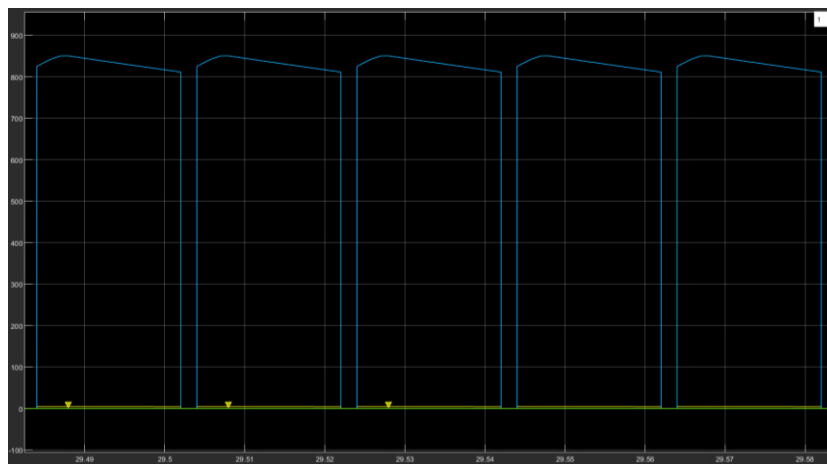


*Figure 97: Output current waveform, proposed circuit A; period 0.02s (Simulink model)*

The voltage waveform followed the current waveform, as was expected, and differed by a factor of the circuit resistance.

The output voltage waveform generated from the Simulink simulation for proposed circuit A at a pulsing period of 0.02s is shown in Figure 98.
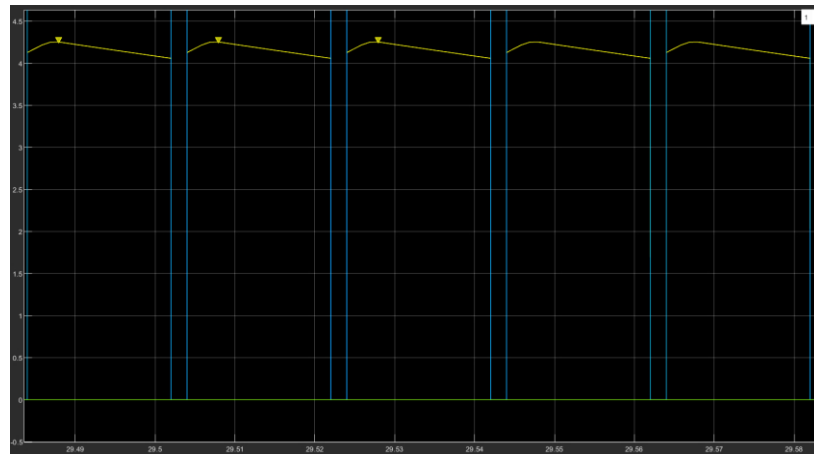


*Figure 98: Output voltage waveform, proposed circuit A; period 0.02s (Simulink model)*

The output current waveform was observed to flatten as the period was decreased (i.e. the frequency of pulsing was increased). This occurred only up to the frequency of the input (50Hz, or 0.02s) – beyond this, the output waveform could not be flattened further with all other circuit elements kept constant. To illustrate this, output current waveform generated from the Simulink simulation for proposed circuit A at a pulsing period of 0.01s is shown in Figure 99.
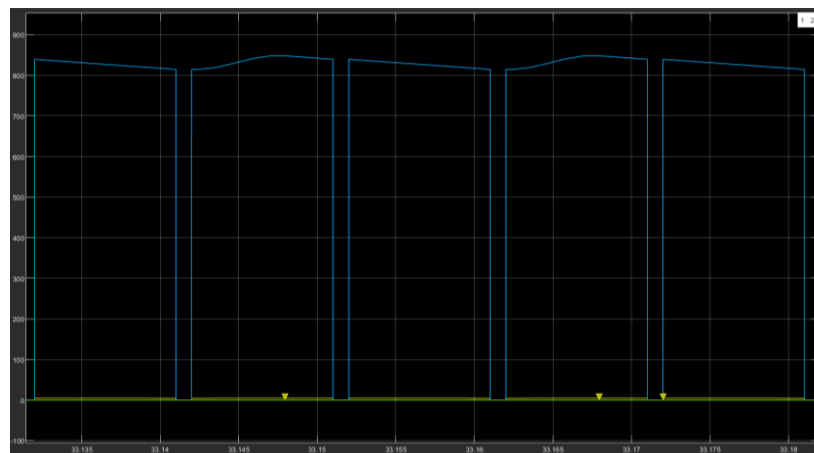


*Figure 99: Output current waveform, proposed circuit A; period 0.01s (Simulink model)*

*Circuit B*

Circuit B used all the circuit elements as employed in circuit A; the only difference is that the rectification was done on the primary instead of the secondary. The circuit diagram as modelled in Simulink is shown in Figure 100.
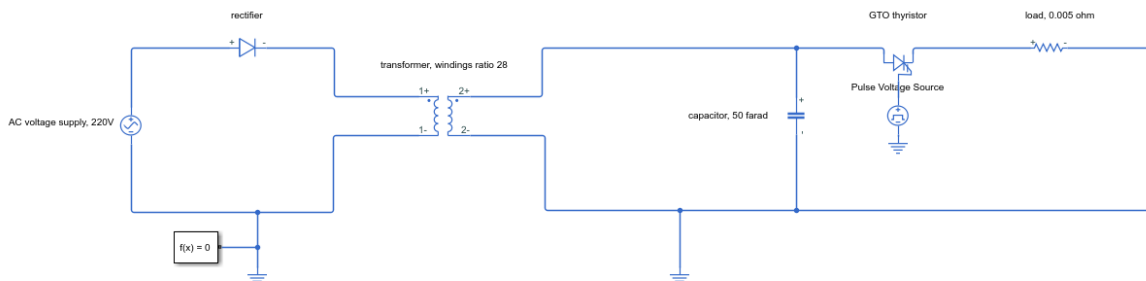


*Figure 100: Electrical schematic, proposed circuit B (Simulink model)*

The input to this circuit was high voltage AC.

The output from this circuit was low voltage, pulsed, smoothed, half-wave primary-rectified current.

The output current and voltage waveforms generated from the Simulink simulation for proposed circuit B at a pulsing period of 0.02s are shown in Figures 101 and 102 (respectively).
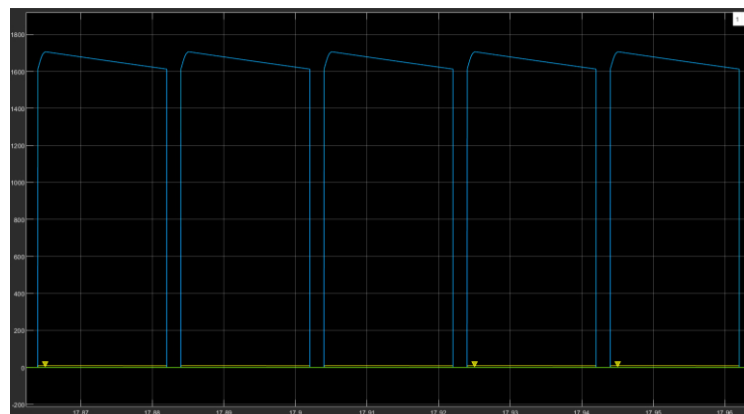


*Figure 101: Output current waveform; proposed circuit B; period 0.02s (Simulink model)*
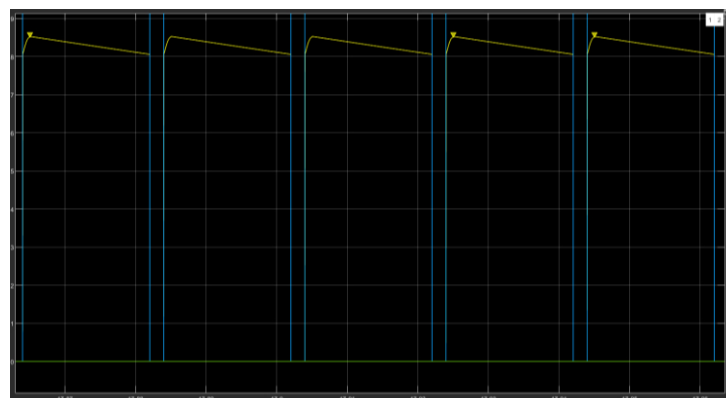


*Figure 102: Output voltage waveform; proposed circuit B; period 0.02s (Simulink model)*

Comparing the output waveforms for circuits A and B, it is clear that it is more favourable to rectify on the primary than the secondary, due to the higher voltage (and thus current) available to the load when rectifying on the primary. Note that the only change which has been made from proposed circuit A to proposed circuit B was the movement of the rectifier from the secondary to the primary – the transformer, capacitor, GTO thyristor and load remained unchanged. This behaviour was to be expected, and was attributable to the voltage drop across the rectifier, which had a greater impact on the circuit when placed on the low voltage side, i.e. the secondary.

*Circuit C*

Circuit C used all the circuit elements as employed in circuit B, except for the pulsing mechanism, which was omitted. The circuit diagram as modelled in Simulink is shown in Figure 103.
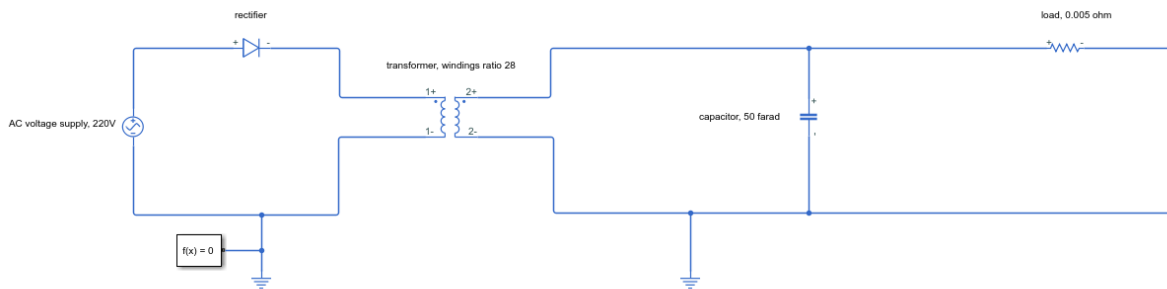


*Figure 103: Electrical schematic, proposed circuit C (Simulink model)*

The input to this circuit was high voltage AC.

The output from this circuit was low voltage, continuous, smoothed, half-wave primary-rectified current.

The output current and voltage waveforms generated from the Simulink simulation for proposed circuit C are shown in Figures 104 and 105 (respectively).
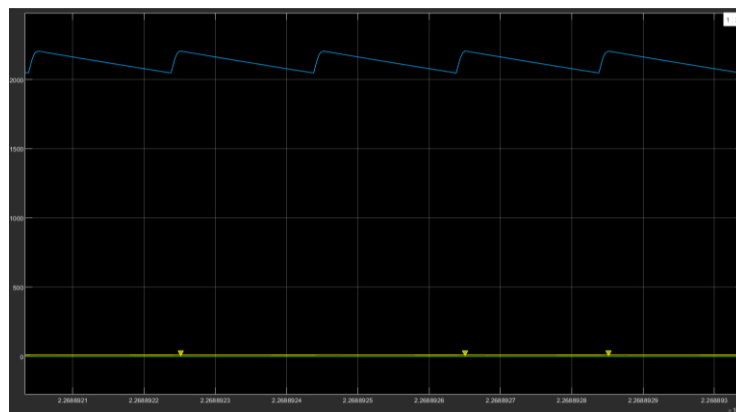


*Figure 104: Output current waveform; proposed circuit C (Simulink model)*
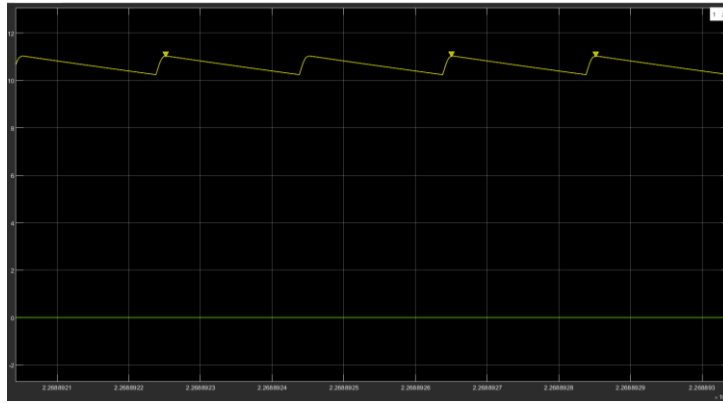
*Figure 105: Output voltage waveform; proposed circuit C (Simulink model)*

Comparing the output waveforms for circuits B and C, a marked improvement was noted in value of the voltage (and thus current) available to the load upon removal of the GTO thyristor used for pulsing the supply to the load. Note that the only change which has been made from proposed circuit B to proposed circuit C is the removal of the GTO thyristor and its associated control circuit for pulsing – the transformer, capacitor and load remained unchanged. This behaviour was once again expected, and was once more attributable to the voltage drop across the thyristor, which had a greater impact on the circuit due to it being on the low voltage side, i.e. the secondary.

*Circuit D*

Circuit D used all the circuit elements as employed in circuit C, except for the capacitor, which was omitted. The circuit diagram as modelled in Simulink is shown in Figure 106.
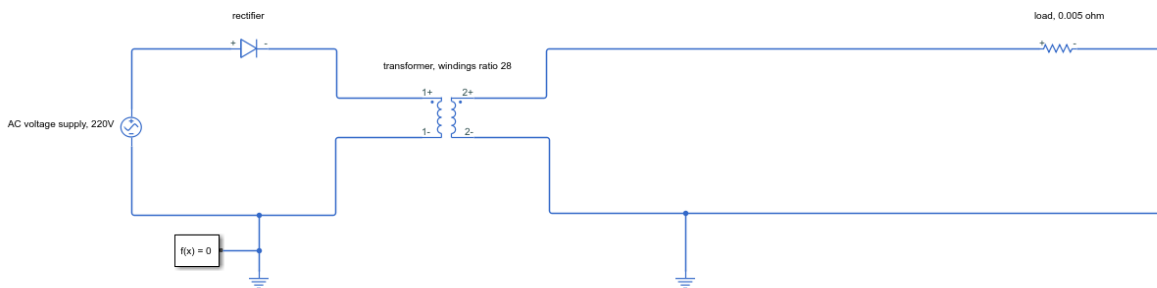


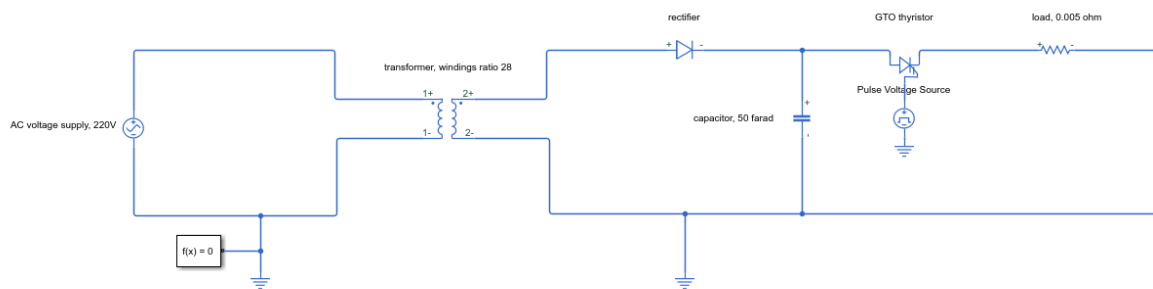*Figure 106: Electrical schematic, proposed circuit D (Simulink model)*

The input to this circuit was high voltage AC.

The output from this circuit was low voltage, continuous, unsmoothed, half-wave primary-rectified current.

The output current and voltage waveforms generated from the Simulink simulation for proposed circuit D are shown in Figures 107 and 108 (respectively).
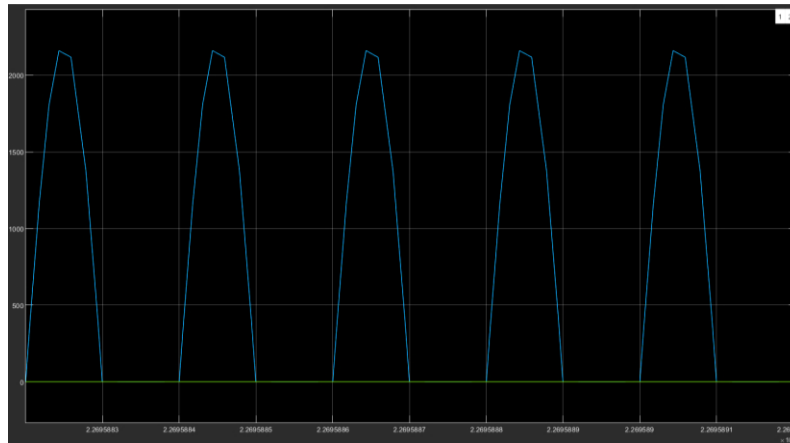


*Figure 107: Output current waveform; proposed circuit D (Simulink model)*
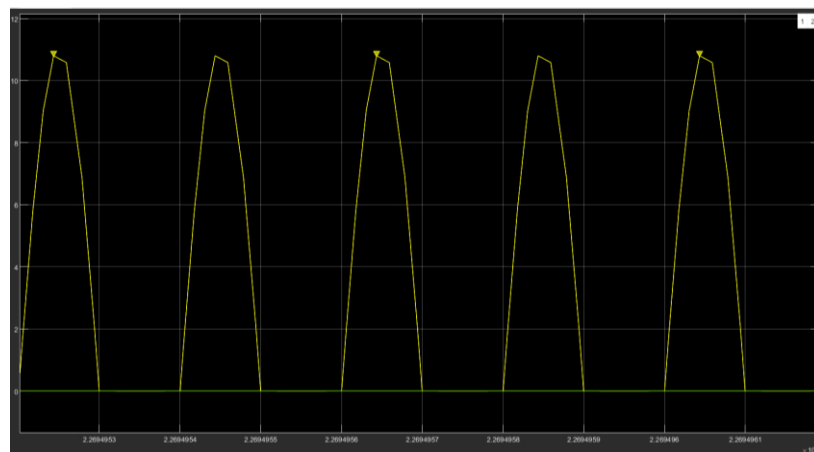


*Figure 108: Output voltage waveform; proposed circuit D (Simulink model)*

Comparing the output waveforms for circuits C and D, it was noted that the peak current and voltage values were unchanged. This behaviour was expected, as the capacitive element in circuit C should not result in any voltage drop; it merely functioned as a mechanism for smoothing the peaks to provide a continuous value.

*Circuit E*

Circuit E used all the circuit elements as employed in circuit D, except for the rectifier on the transformer primary, which was omitted. The circuit diagram as modelled in Simulink is shown in Figure 109.
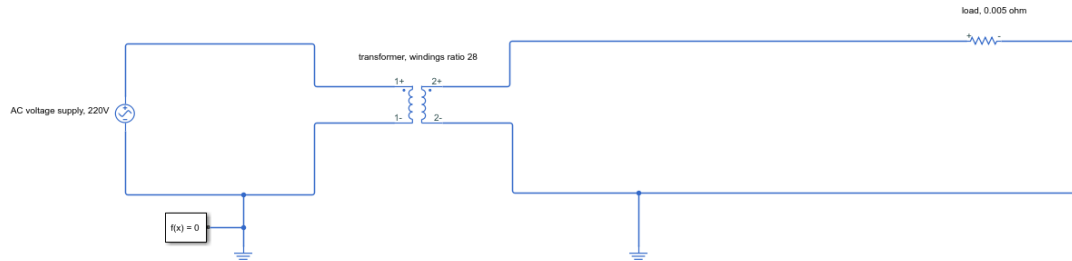


*Figure 109: Electrical schematic, proposed circuit E (Simulink model)*

The input to this circuit was high voltage AC.

The output from this circuit was low voltage AC.

The output current and voltage waveforms generated from the Simulink simulation for proposed circuit E are shown in Figures 110 and 111 (respectively).
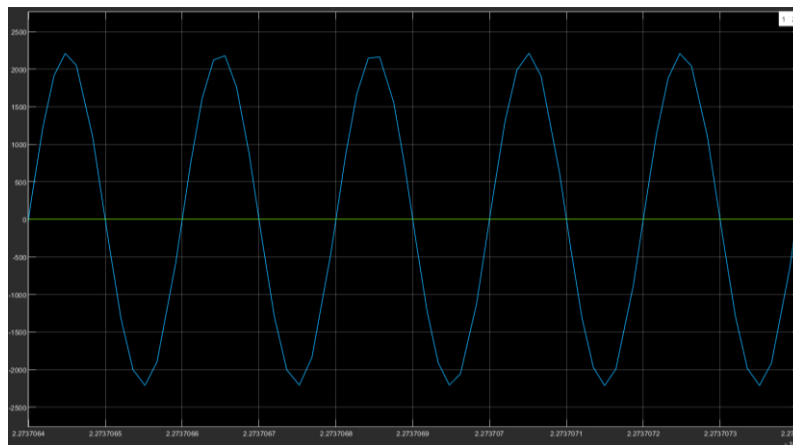


*Figure 110: Output current waveform; proposed circuit E (Simulink model)*
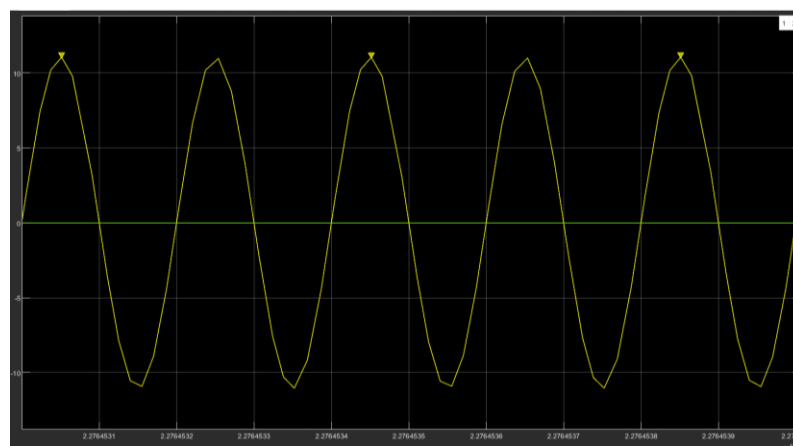


*Figure 111: Output voltage waveform; proposed circuit E (Simulink model)*

*Proposed Circuit F*

Circuit F employed direct current as the power source. The circuit diagram as modelled in Simulink is shown in Figure 112.
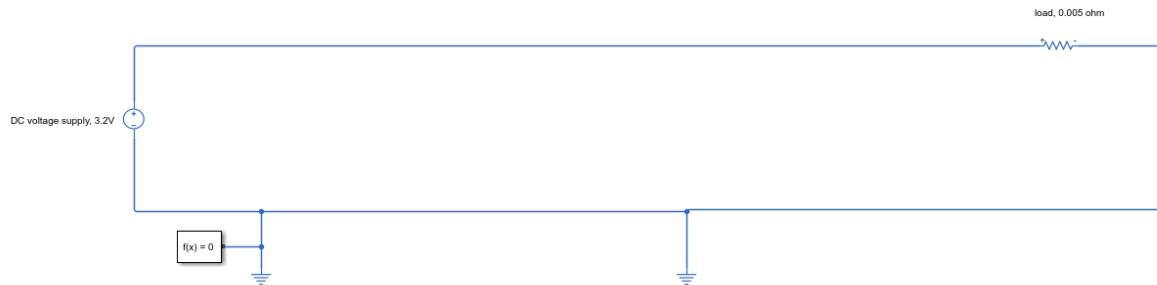


*Figure 112: Electrical schematic, proposed circuit F (Simulink model)*

The input and output of this circuit were continuous DC.

The output current and voltage waveforms generated from the Simulink simulation for proposed circuit D are shown in Figures 113 and 114 (respectively).
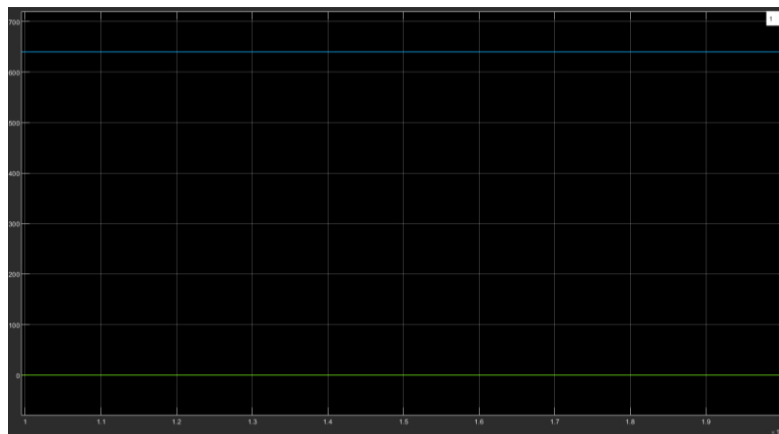


*Figure 113: Input/output current waveform; proposed circuit F (Simulink model)*
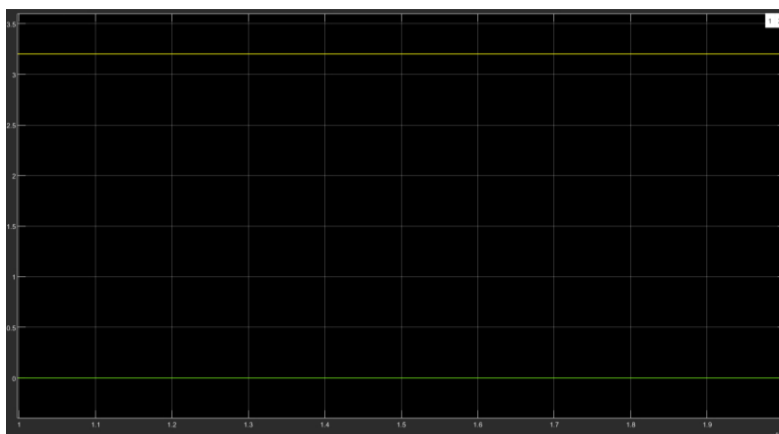


*Figure 114: Input/output voltage waveform; proposed circuit F (Simulink model)*

*Discussion*

Various circuits were explored for the purpose of provision of a spark plasma sintering current to the titanium sample. Any of these circuits should fulfil the intended purpose of forming a base circuit with which to sinter the titanium sample in the mill.

It is out of the scope of this research to build up all proposed circuits for testing, but it is recommended to do so for further research and development, with a view to comparing the effect of each waveform on the SPS process and the sintered compact produced.

### 4.6.4. Expected Resistive Heating

For a nip angle of 12.29°, the powder spends 0.6s in the nip region at the minimum roll speed for reasonable compact consolidation of 3.4rpm [66] (as determined in Section 4.3.5.), i.e. 0.6s where it will be at a suitable level of compaction between the rolls to conduct electric current, as given by the equation below.

*Equation 24: Dwell time in the nip region*

$$t_{nip} = \frac{\alpha}{360°/rev} \times \frac{60s/min}{3.4rev/min} = \frac{12.29° \times 60}{360° \times 3.4}s = 0.6s$$

The expected temperature change across the sample is given by the equation for resistive heating, as discussed in the literature review, Section 2.4.1. The specific heat of titanium is 0.544284 J/(g.K), and the duty cycle was modelled as 90% (i.e. using a 9:1 on-off pulse sequence). The source of the values for current and resistance used here is explained in Section 4.6.1. Using the expected minimum mass flow rate discussed in the hopper design Section 4.4.3. of 18g/s (ensuring mass equilibrium through the rolls at a roll speed of 3.4rpm), and as per Johanson's model of the nip angle (reviewed in Section 2.3.2. and simulated in Section 4.3.5., with the dwell time in the nip region calculated above), it may be concluded that the titanium spends 0.6s of every second of operation in the nip region during the simultaneous DPR-SPS process. The temperature change across the titanium sample can thus be calculated as shown below.

*Equation 25: Expected temperature change across the compact*

$$\Delta T = \frac{I^2 \times R \times t_{nip}}{Cv \times m} = \frac{(1000A)^2 \times (0.005\Omega) \times (0.9 \times 0.6s)}{0.544284J/(g.K) \times 18g} = 275K$$

This value of 275K represents the expected bulk temperature change per second across the compact for the operating conditions described above. However, it does not account for the much greater temperature change at the contact surfaces of the powdered material particles, which is significant in the SPS process, as reviewed in Section 2.4.1. Full thermal modelling of the powder, specifically with regard to the temperature at the powder contact surfaces, is unfortunately out of the scope of this work. As discussed in Section 2.4.1., titanium may be sintered at temperatures as low as 700°C. If the SPS process depended on resistive heating only, it would be concluded that the minimum rolling speed required for consolidation of the titanium powder is too high for the titanium sintering process (and thus that the simultaneous DPR-SPS process was not feasible, as per the hypothesis in Section 4.4.8. that different rolling speeds would be required for the DPR process and the SPS process). However, it must be noted that if the above temperature rise of 275°C is achieved for the bulk of the material, a much greater temperature rise would be achieved at the particle contact points, which may be sufficient for sintering the material at the minimum prescribed rolling speed of this mill of 3.4rpm (described in Section 4.3), thus allowing for successful application of a simultaneous DPR-SPS process. This is best explored through further research.

# 5. Commissioning the SPS-DPR Mill

With the mill fully modelled and tested using numerical methods, the next step was to build and commission the resulting design. This chapter details the components procured, the full manufacturing and assembly process, and the lessons learned during commissioning.

## 5.1. Procurement of Components

As stated in the introduction and design chapters, one of the criteria for the SPS-DPR mill is the cost-effectiveness of its implementation. This is an important aspect of the research, as one of its objectives is to decrease the cost of titanium processing. Throughout the procurement process, the student was thus conscious of the cost implications each of the components.

Certain components were already available from the 2017 project [70], notably the bulk of the drive system. The steel required for fabrication of the frame, and the hopper and exit slide, were donated to the student for the project. The rest of the components were sourced using funding allocated to UKZN for titanium research.

A breakdown of the costs of the components sourced by the student is summarised in Table 11.

*Table 11: Components sourced for the DPR-SPS mill*

| Item | Quantity | Supplier | Actual Cost | | Estimated Value | |
|---|---|---|---|---|---|---|
| Steel billet for frame, 1 ton | | ArcelorMittal SA | -- | | R | 16 000.00 |
| Machining and assembly of mill, machining of couplings, machining of worm and gear shafts, machining of bearing block housings | 1 | Fountain Industries | R | 37 583.15 | R | 37 583.15 |
| Cheek plates and carbon brushes | 2 | Fountain Industries | R | 14 951.44 | R | 14 951.44 |
| Flexible Couplings, Timken, QF25 | 2 | BMG | R | 7 793.25 | R | 7 793.25 |
| Vesconite bushings | 8 | DEMS | R | 7 552.74 | R | 7 552.74 |
| Cables, capacitors and 5pin plug | 1 | DIY Electronics | R | 9 248.30 | R | 9 248.30 |
| Miscellaneous tools | 1 | EIS (own card) | R | 1 999.83 | R | 1 999.83 |
| Bootlace crimping tool | 1 | Ron Tomlin | R | 570.72 | R | 570.72 |
| Insulated screwdriver set | 1 | Ron Tomlin | R | 405.38 | R | 405.38 |
| Carbon brush backing plates | 2 | Steelcom Engineering | R | 602.60 | R | 602.60 |
| Exit slide | 1 | Hilliar Engineering | -- | | R | 600.00 |
| Hopper | 1 | Hilliar Engineering | -- | | R | 600.00 |
| Clampmeter | 1 | RS | R | 2 417.30 | R | 2 417.30 |
| Multimeter | 1 | RS | R | 292.10 | R | 292.10 |
| Vernier and micrometer | 1 | RS | R | 3 717.95 | R | 3 717.95 |
| Feeler guages | 1 | RS | R | 316.25 | R | 316.25 |
| Single phase plug for transformer | 2 | RS | R | 41.40 | R | 41.40 |
| Fuse 220V 20A | 5 | RS | R | 204.70 | R | 204.70 |
| Insulation tape | 1 | RS | R | 254.15 | R | 254.15 |
| Cable ties | 1 | RS | R | 143.75 | R | 143.75 |
| Lugs | 15 | Stone-Stamcor | R | 366.22 | R | 366.22 |
| Terminal block (copper block) | 1 | Copalcor | R | 800.00 | R | 800.00 |
| Vesconite sheet | 2 | DEMS | R | 2 151.88 | R | 2 151.88 |
| Toggle switch | 1 | Stone-Stamcor | R | 70.15 | R | 70.15 |
| Total | | | R | 91 483.26 | R | 108 683.26 |

## 5.2. Manufacturing and Assembly

This section will discuss the manufacturing and assembly process of the mill, including the mechanical and electrical components thereof.

### 5.2.1. Materials for Assembly

The steel billet for the rolling mill frame, shown in Figure 115, was donated to the project by a South African steel manufacturer. The rolling mill frame was fabricated locally.



*Figure 115: Steel billet donated for the frame*

The drive components for the mill, including the AC motor, worms, gears, rolls, bearings and couplings were then assembled to the frame by the same company which fabricated the frame. The bulk of the drive components or input materials thereof are shown in Figure 116.
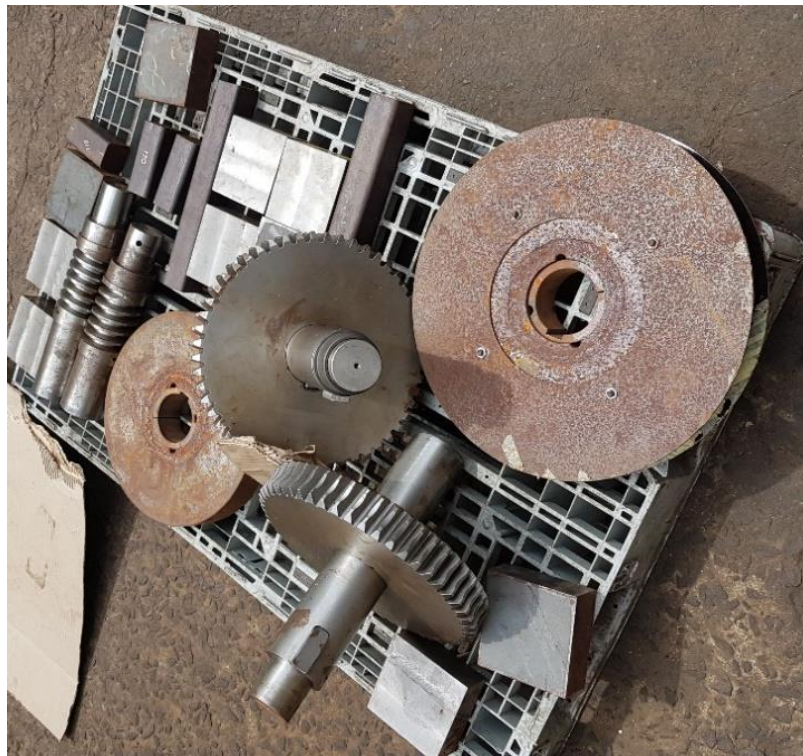


*Figure 116: Rolling mill drive components produced in 2017*

114

### 5.2.2. AC Motor and Electric Drive

Before mechanically coupling the motor to the mill, the motor was electrically and mechanically tested. The motor is powered by three-phase AC, with its windings connected in a delta configuration. The voltage and current on all three phases were checked using a clampmeter, to ensure that there was no earth leakage and that the resistance was constant between the windings. This is shown in Figure 117.



*Figure 117: Measuring the voltage and current on the AC motor*

The motor output speed was then tested using a tachometer, as shown in Figure 118.
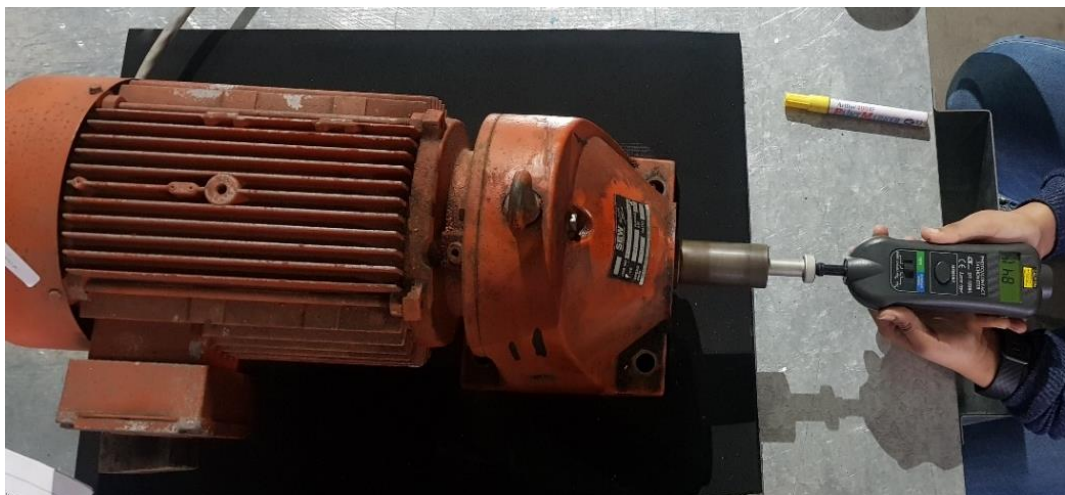


*Figure 118: Measuring the motor speed on the output shaft using a tachometer*

The motor was found to be in good working order. The rated and measured specifications of the motor are listed in Table 12.

*Table 12: AC motor specifications*

| Specification | Value | Unit | Rated/Measured |
|---|---|---|---|
| Power | 5.5 | kW | rated |
| Output Shaft Speed | 803.0 | rpm | rated |
| Output Shaft Speed | 841.4 | rpm | measured |
| Output Torque | 65.0 | Nm | rated |
| Voltage (line-to-line) | 380.0 | V | rated |
| Voltage (line-to-neutral) | 220.0 | V | rated |
| Current (line) | 11.4 | A | rated |
| Voltage (line-to-line) | 412/408/413 | V | measured |
| Voltage (line-to-neutral) | 236/236/237 | V | measured |
| Current | 7.1/8.1/7.1 | A | measured |
| Power Factor | 0.85 | | rated |

The start-up guide for the VSD was used to guide the electrical connection thereof to the motor, as shown in Figure 119.
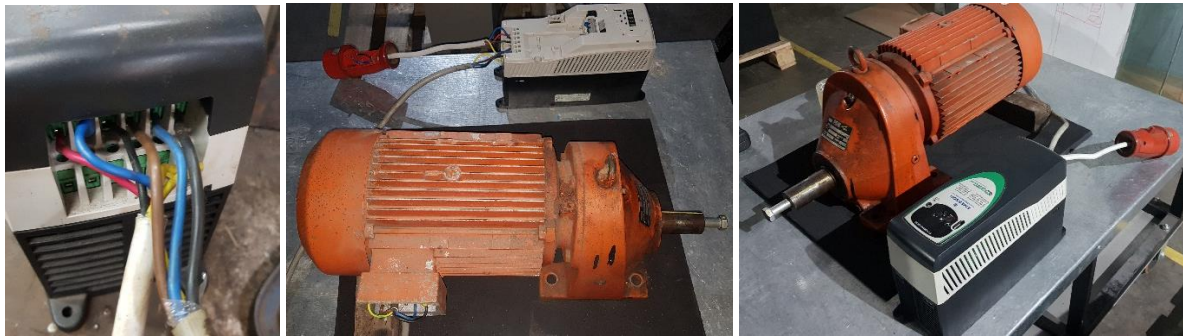


*Figure 119: Connecting the VSD to the AC motor*

The start-up guide was also used to parametrise the VSD. A list of the parameters used to set up the VSD is shown in Table 13.

*Table 13: VSD parameter setup*

| Parameter | Description | User Input Value |
|---|---|---|
| Pr 01 | Minimum Speed (Hz) | 0.00 |
| Pr 02 | Maximum Speed (Hz) | 50.00 |
| Pr 03 | Acceleration Rate (s/100Hz) | 5.00 |
| Pr 04 | Deceleration Rate (s/100Hz) | 10.00 |
| Pr 05 | Drive Configuration | PAd |
| Pr 06 | Motor Rated Current (A) | 11.40 |
| Pr 07 | Motor Rated Speed (rpm) | 839.00 |
| Pr 08 | Motor Rated Voltage (V) | 230.00 |
| Pr 09 | Motor Rated Power Factor (cosφ) | 0.85 |
| Pr 10 | Parameter Access | L1 |

Parameters Pr 01 – Pr 04 are the default values for the drive. Pr 05 is used to control the VSD using the keypad – the up and down arrows on the VSD control panel can thus be used to adjust the speed on the mill. Pr 06 – Pr 09 are based on the specific motor being used, and were found on the motor datasheet. Pr 10 grants lower level access to the parameters (i.e. access to Pr 01 – Pr 10 only). L1 is the default for the VSD, and it was not deemed necessary by the student to access any parameters other than these for the purpose of the motor control required.

The output rotational speed of the AC motor was measured for varying frequencies on the VSD, using the VSD control pad to adjust the motor shaft speed, as shown in Figure 120.



*Figure 120: Varying the motor speed using the VSD*

The results of the speed testing are shown in Figure 121.
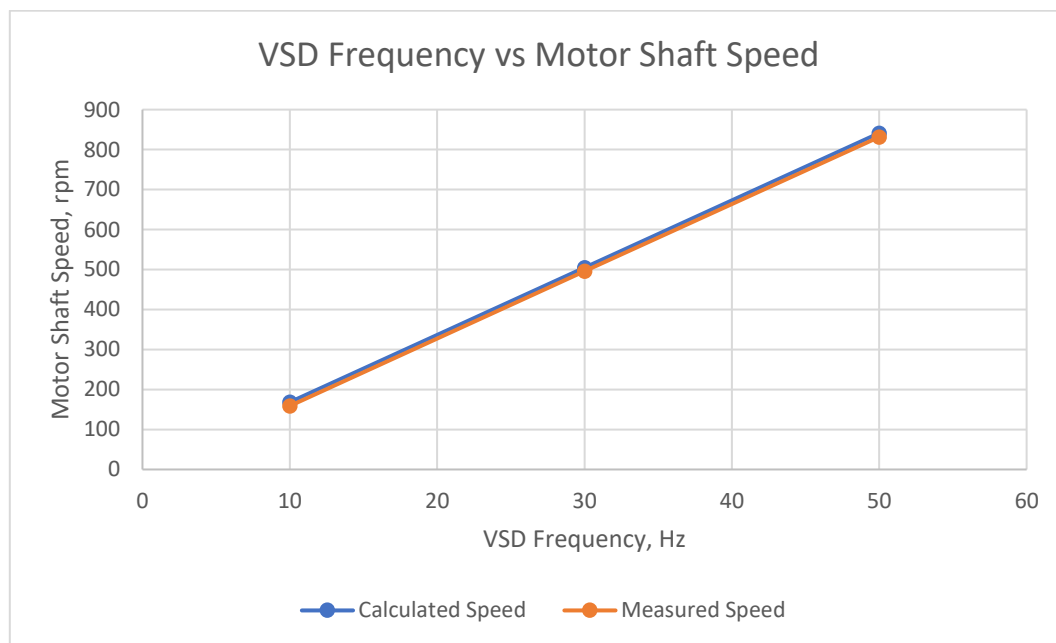


*Figure 121: VSD frequency versus motor shaft speed*

The VSD and motor behaved as expected, with the motor rotational speed varying proportionally with the VSD frequency. It was thus confirmed that the VSD could be used to control the output speed of the motor during operation of the mill.

For the rolling speeds required as discussed in Section 4.3.5 of 3.4 – 11.4 rpm, the frequency range for the VSD is 10 – 35Hz.

A new three phase plug was added to the motor and drive assembly with an extended cable, to ensure that distance from three-phase power would not be an issue when the mill was being operated.

### 5.2.3. DPR Mill Assembly

For the full assembly of the mill, the frame members were first cut to length using a bandsaw, then machined at either end in preparation for V-groove welding. The frame members were then assembled and tack welded, as shown in Figure 122.



*Figure 122: Tack welded frame*

The bearings were machined, and the interface between the bearing housings and the vesconite bushings refined to ensure a good sliding fit between the two components. The partially-machined bearing housing with vesconite bushing installed is shown in Figure 123.
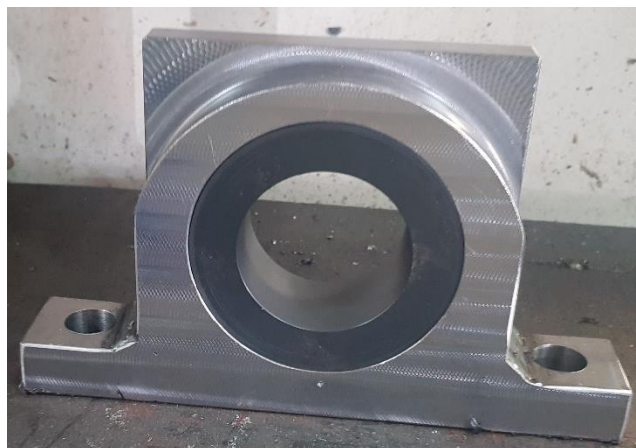


*Figure 123: Partially machined bearing housing, with vesconite bushing inserted*

The drive components were then positioned onto the tack welded frame before final welding, as the alignment of drive components it critical in this application, and only minor adjustments to the alignment would be possible once the frame was fully welded.

The assembly of the drive components onto the frame is shown in Figure 124.



*Figure 124: Positioning of drive components on the frame*

Once all components were suitably positioned, the welding was completed, the alignment of the drive components was checked, and the frame was painted for corrosion protection. The assembled and painted mechanical assembly (before fitment of the hopper) is shown in Figure 125.



*Figure 125: Assembled and painted mechanical assembly*

The sheet metal for the hopper was then laser cut and welded. The laser cutting process is shown in Figure 126.



*Figure 126: Laser cutting of hopper sheet metal*

The assembled hopper is shown in Figure 127.



*Figure 127: Hopper assembly*

### 5.2.4. SPS System Assembly

The SPS system assembly consists of the power source for sintering, the carbon brushes for transmitting current from this power source to the rotating compacting rolls, a backing plate for each carbon brush, the cables connecting the power source to the brushes via the backing plate, and the brackets used to fix the backing plates to the frame. The carbon brushes were manufactured locally. The machined brushes are shown in Figure 128.



*Figure 128: Machined carbon brushes for SPS system*

The first step in the SPS assembly was preparing the connecting cables by cutting the cables to size and crimping lugs onto either end of each cable. The lugs were then connected to the carbon brushes and the backing plates using bolts threaded into the carbon brushes. The backing plates were then fixed to the brackets – an insulating material was fixed between each backing plate and its bracket to ensure the SPS current would not be transmitted to the frame. The carbon brush assembly, and the installation of these onto the rolls, is shown in Figure 129.



*Figure 129: Assembly and installation of carbon brushes for SPS system*

### 5.2.5. DPR-SPS Mill Assembly

As a final step, the electrical power source was connected to the SPS circuit. The fully assembled DPR-SPS mill is shown in Figure 130.
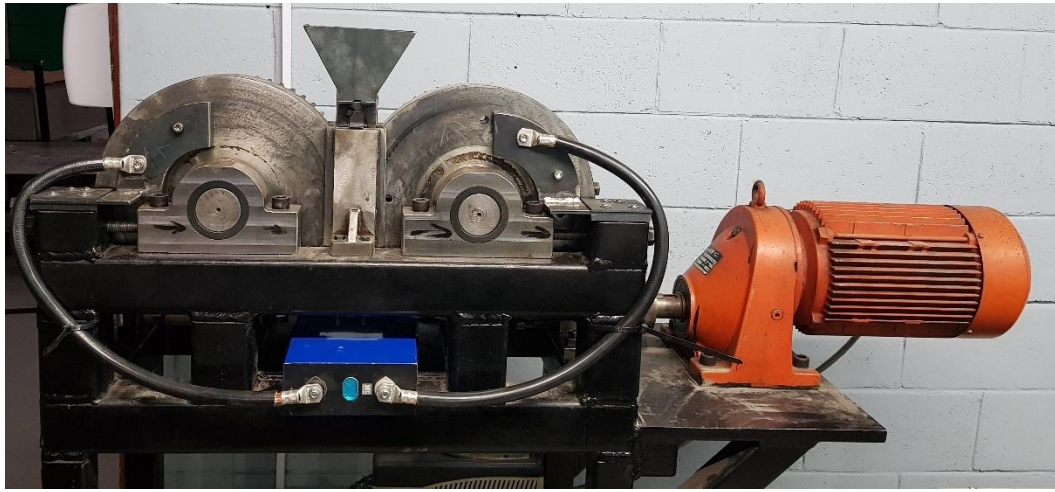


*Figure 130: Fully assembled DPR-SPS mill*

## 5.3. Lessons Learned

This section is a discussion of the issues identified during the course of commissioning the mill, as well as details on how they were corrected, or suggestions on how they may be rectified in future development of the mill.

### 5.3.1. Drive System Clearances

The initial design of the worms and gears, and the coupling thereof, allowed only 10mm of clearance between the coupled worm shafts. A different coupling was selected in this design (for reasons including ease of assembly and electrical isolation). This coupling required 30mm between the worm shafts, and in order to maintain the correct distance between the rolls (which are on the same shafts as the gears), the gears meshed with the worms at different points along the shaft than originally expected, resulting in insufficient clearance between the worms and gears at the ends of the toothed portions of the worms, as shown in Figure 131.



*Figure 131: Interference between worms and gears*

This was corrected by machining the toothed ends of the worms to provide sufficient clearance between the components.

There was also insufficient clearance between the gears and the bearings supporting the worm shafts. This was corrected by slight machining of the tops of the worm shaft bearing housings to provide sufficient clearance between the components.

### 5.3.2. Drive System Alignment

During commissioning of the mill, when the motor was coupled to the worm shafts and tested without load, the drive to the motor displayed an overcurrent error, as is shown in Figure 132.



*Figure 132: VSD current limit error*

This error code indicated that there was mechanical overload on the mill. During fault-finding it was determined that there was misalignment on the worm shafts due to slight warping on the frame which occurred during welding. This was not entirely unexpected given the size of the welded components and the welds. The alignment of the worms was corrected by adjusting the seating of the worm shaft bearing blocks, and the system subsequently functioned correctly under the no load condition.

### 5.3.3. Roll Gap Adjustment

The screw mechanism can be used as is for adjustment of the roll gap. The process of roll gap adjustment is as follows:

1. The bolts on the adjustable bearing blocks are loosened

2. The screw mechanism is used to adjust the gap

3. The roll gap is checked with a shim

4. The bolts on the adjustable bearing blocks are tightened

This process is time consuming when frequent gap changes are required and could be modified to be more user friendly in future, for example with the use of handles on the screw mechanism (removing the need for adjustment with a shifting spanner) and perhaps a digital roll gap display.

### 5.3.4. Carbon Brush Assemblies for SPS Circuit

The carbon brushes appeared to have good seating against the surface of the roll. However, the mechanism of fixing the carbon brushes to the mill should be improved, with an additional applied pressure to ensure the carbon brushes maintain good contact during the rolling process for optimised efficiency of the current transfer process to the rolls. It is expected that this will decrease the resistance across the interface between the carbon brushes and the rolls, and thus increase the current through the compact.

The carbon brushes are currently designed with internal threads on each brush's termination points – the lugs from the SPS power supply are connected to the carbon brushes using bolts through these threaded termination points. However, it was noted during assembly of the SPS system that the carbon brush threads are easily damaged, as shown in Figure 133.



*Figure 133: Damage observed on the internal threads of the carbon brush during assembly*

It is thus suggested that future carbon brush designs use termination points that are tamped into the brushes, instead of the use of tapped holes.

During testing of the SPS system, the resistance across the circuit higher than expected and decreased when a manual force was applied to the brush. In order to correct the seating issue that this was indicative of, a better mounting mechanism for each carbon brush assembly was designed. The carbon brush mounting brackets were widened to improve their stability, as each fully assembled carbon brush assembly was quite heavy. Vesconite sheet was then cut and drilled to form insulating liners on either side of each mounting bracket. The unthreaded portions of the bolts to be used for fastening the mounting brackets to the rolling mill frame were covered with heat shrink to maintain electrical insulation of the steel mounting bracket from the frame. The mounting bracket holes were slotted to allow for adjustment of the carbon brushes (perpendicular to their surfaces) onto the rolls, for better seating. Since the measured current was much lower than expected, one of the cables to each brush assembly was removed.

The initial assembly, and improved assembly, are shown in Figure 134.
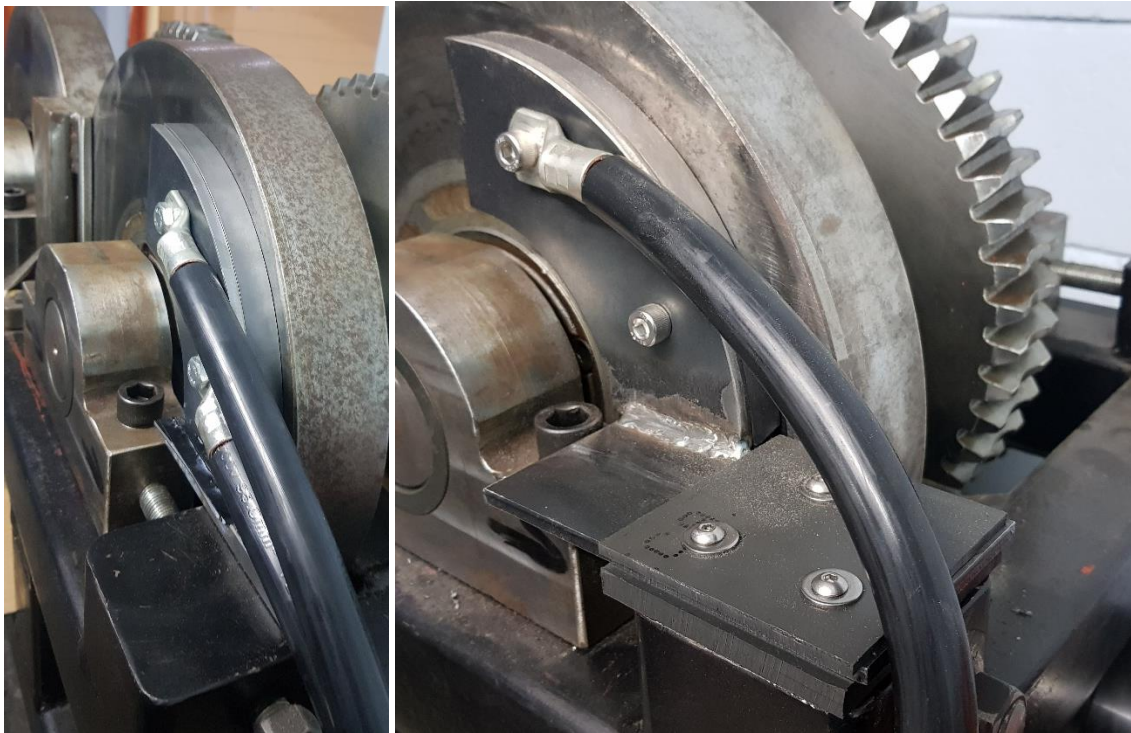


*Figure 134: Initial and improved mounting of the carbon brush assembly to the frame (left to right)*

### 5.3.5. Electrical Isolation of SPS Current from Mill Frame

Each of the flexible couplings selected for this design consist of two hubs, one on each shaft to be coupled, connected by a rigid urethane insert which transmits the torque. Although the flexible coupling used between the motor and the worm gear should have a clearance of a few millimetres between the respective steel hubs due to the urethane insert (which provides the mechanism of electrical isolation of these two components), during final alignment of the drive system the two hubs had to be positioned closer to each other than initially anticipated. When checked with a multimeter, it was confirmed that this alignment issue resulted in electrical continuity between one of the rolls and the frame.

However, it was determined that due to there being no path for the current to flow back to the SPS power supply from the frame (i.e. there is no closed conduction path across the frame), the frame would act as a capacitive rather than a resistive element, which would not result in any electrical conduction, nor in an unsafe condition. For future testing, the motor shaft should be properly electrically isolated from the SPS circuit. This can be done through inclusion of an insulating bushing between the motor shaft and coupling hub, or correction of the motor axial alignment.

The electrical isolation was checked between the shafts and bearing blocks separated by vesconite, and as expected no electrical continuity was measured across these elements. No electrical continuity was noted between the two worm shafts either (separated by an identical flexible coupling as used between the motor and worm shaft).

# 6. Testing the SPS-DPR Mill

The final step in the process of developing this research was the testing of the mill which was commissioned as described in Chapter 5. This chapter begins with an overview of the testing to be performed, then moves on to the details of the testing of both the DPR process, and the DPR-SPS process. It concludes with a summary of the testing performed.

## 6.1. Overview of Testing

For initial testing of the mill, the aim was to test both processes (DPR and SPS), first independently then simultaneously. Initial testing of the DPR process was conducted by feeding titanium powder to the rolls and ensuring a compact was formed. Initial testing was performed on the SPS system by applying a voltage across the rolls and ensuring current flowed through the sample without creating any dangerous conditions on the mill, as proof of the concept of the combination of the two processes (i.e. DPR and SPS).

Parametric testing was then performed on the DPR process of the mill, by varying first the roll speed, then the roll gap, to determine the effect of each of these parameters on the density of the compact formed.

Testing of the DPR process versus the DPR-SPS process was then performed by rolling titanium powder through the mill with and without application of the SPS current, with the resulting densities of the strips compared.

Any discrepancies of the mill's actual behaviour from its expected behaviour were noted, with recommendations given on how to improve the mill performance in future.

## 6.2. Testing the DPR Process

### 6.2.1. Testing Overview and Observations

Once the mill was commissioned and found to be in good working order, the DPR process was tested.

100 mesh HDH titanium powder was used for this testing, as selected in Section 3.2.2. The roll gap was adjusted using the screw mechanism. The motor was started, and the powder was fed to the rolls without the use of a hopper. The roll speed was varied through varying the frequency on the VSD using the keypad.

The following observations were made during initial testing:

1. All compacts formed could be handled reasonably well, but did experience some disintegration at the edges when handled

2. Increasing the roll gap resulted in visually thicker strips

3. Decreasing the roll gap resulted in denser strips being produced

4. Increasing the rolling speed resulted in visually wider strips

5. Increasing the powder feed rate resulted in denser strips being produced

6. A large portion of powder leakage was noted between the rolls; a proportionally higher volume of powder leakage was observed at lower roll speeds, and at larger roll gaps

7. Powder leakage from the sides of the rolls was successfully prevented via the cheek plates

8. There did not appear to be any unwanted roll gap expansion during the rolling process

The increased density at smaller roll gaps (3) or higher powder feed rates (5) was achieved only up to a certain point, beyond which the VSD cut power to the mill. This was expected from the literature reviewed both in Section 2.3.2. (since, per the Johanson model, a higher density requires a higher pressure applied to the powder [13] which requires a greater applied torque from the motor) and in Section 2.3.5 (in which Zhang experienced that the compactor was overloaded when the feeding rate was too high [5]).

The result in (4) was also expected from the literature reviewed in Section 2.3.5., in which Zhang deduced that the strip width is proportional to the roll speed, regardless of the roll face width [5].

Figures 135, 136 and 137 show the first compacts formed through the mill.



*Figure 135: DPR compact, 0.8mm roll gap, 3.4rpm rolling speed (10Hz at the VSD)*



*Figure 136: DPR compact, 0.6mm roll gap, 5.0rpm rolling speed (15Hz at the VSD)*



*Figure 137: DPR compacts formed between 5.0 – 8.2rpm rolling speed (15 – 25Hz at the VSD)*

The mill was initially tested with a roll gap of 1.6mm, as per the design, and a rolling speed of 10Hz. However, no consolidation was observed with this setup. This is assumed to be due to the high volume of powder leakage present at this low roll speed and large roll gap. For further testing, the roll gap was then decreased to between 0.6mm – 0.8mm to limit the powder leakage. This is discussed further in Section 6.2.2.

### 6.2.2. Effect of Powder Leakage on the DPR Process

Since the powder leakage was clearly not negligible, it had an appreciable impact on the pressure distribution between the rolls and thus the density of the compact formed, as reviewed in Section 2.3.2. The MATLAB model built in Section 4.3.4. was thus adjusted to include powder leakage, and the simulation was run at different values of powder leakage to determine its effect on the compact density and the roll separating force. The compact density was plotted since the experimental results must be compared to the simulated results after correcting for powder leakage. The roll separating force as a function of the powder leakage was plotted on the same set of axes, as the density of the compact formed is limited by the strength of the frame, as simulated in Section 4.5.2. The allowable torque of the motor is, of course, also a limitation on the compact density; however, the VSD protects the motor by cutting out when the parametrised limits are exceeded, so the motor cannot inadvertently be overloaded.

The effects of powder leakage on the rolling mill are shown graphically in Figure 138, for a rolling gap of 0.6mm.
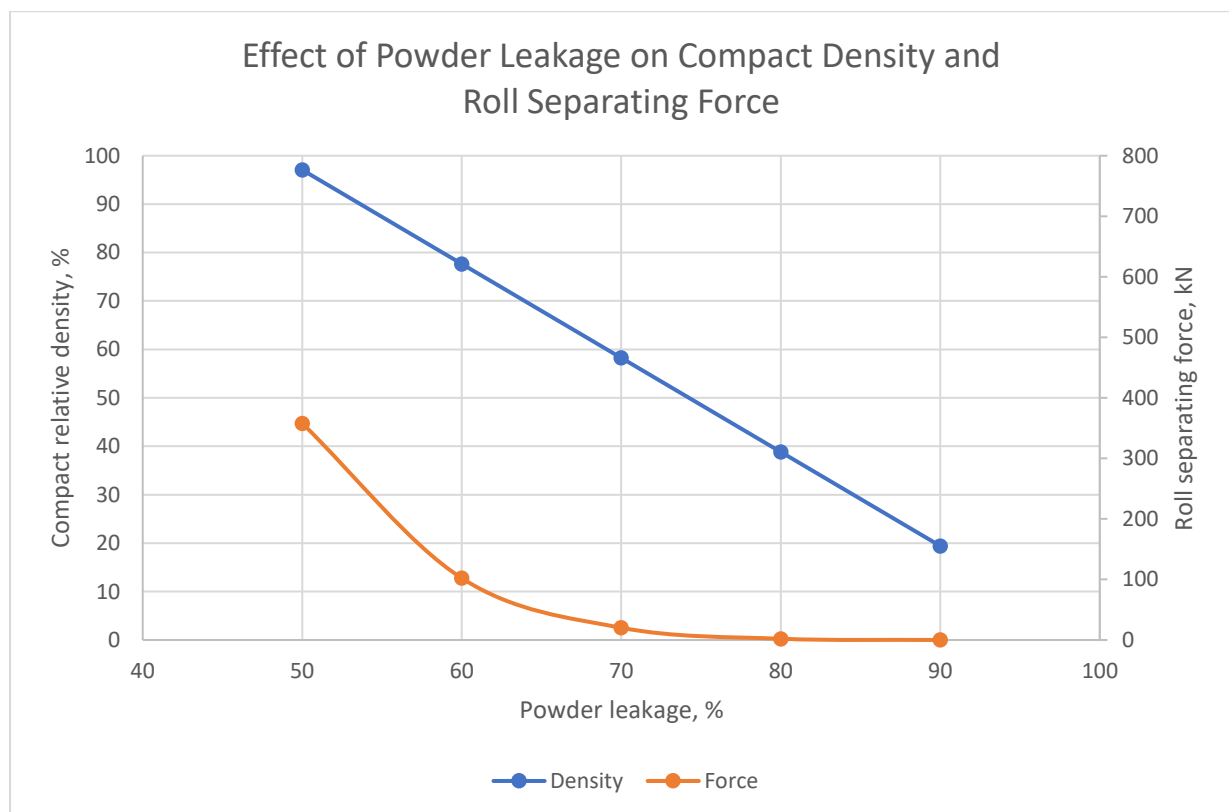


*Figure 138: Effect of powder leakage on the rolling mill, roll gap 0.6mm (MATLAB model)*

The bulk density of the uncompacted powder is 40%, which indicates that at "compact" densities below 40%, no actual consolidation will occur. This is equivalent to powder leakage values of 80% and higher.

Since the testing was to be conducted at different roll gaps, the MATLAB simulation was run at different roll gaps to easily determine the expected compact density with the effect of powder leakage considered. These results are shown in Figure 139.
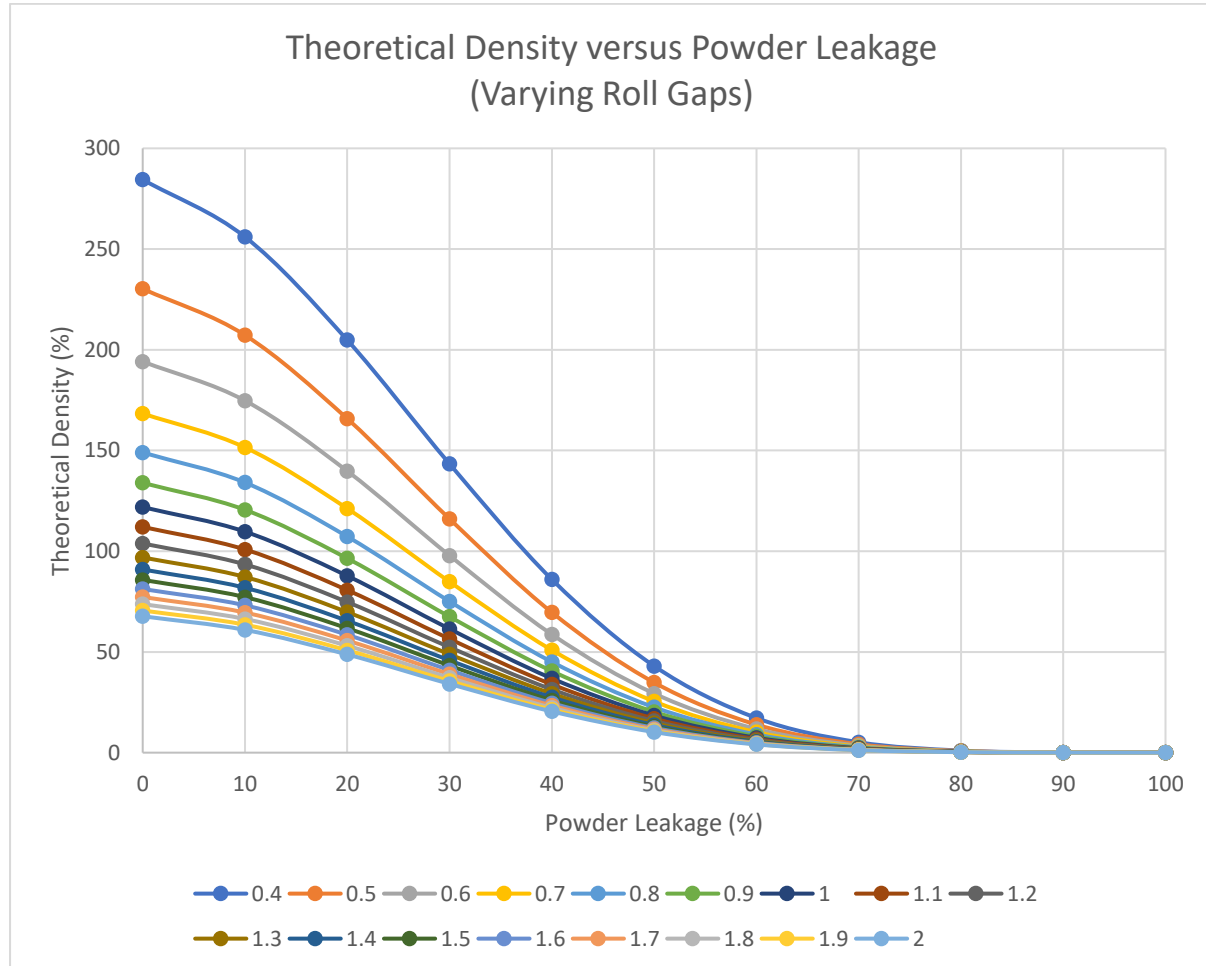


*Figure 139: Theoretical compact density versus powder leakage factor for varying roll gaps (MATLAB model)*

Note that the above figure can be used to determine the maximum density of the sample that is possible for a single pass through the mill, for zero powder leakage, by referring to the y-intercept of each of the graphs. For example, if the initially designed roll gap of 1.6mm is consulted in the figure above, the expected density if 81.25% is noted as the y-intercept.

### 6.2.3. Parametric DPR Testing

Once the mill was commissioned and initial observations made under various operating parameters (including roll speed and roll gap), structured parametric testing was conducted. As discussed, density of the compact was a key consideration for this phase of the project – the objective was to achieve high compact densities of the green compact.

*Roll speed*

The first parameter varied for this testing was the roll speed. 20g samples of powder were measured out for each test point, as shown in Figure 140.
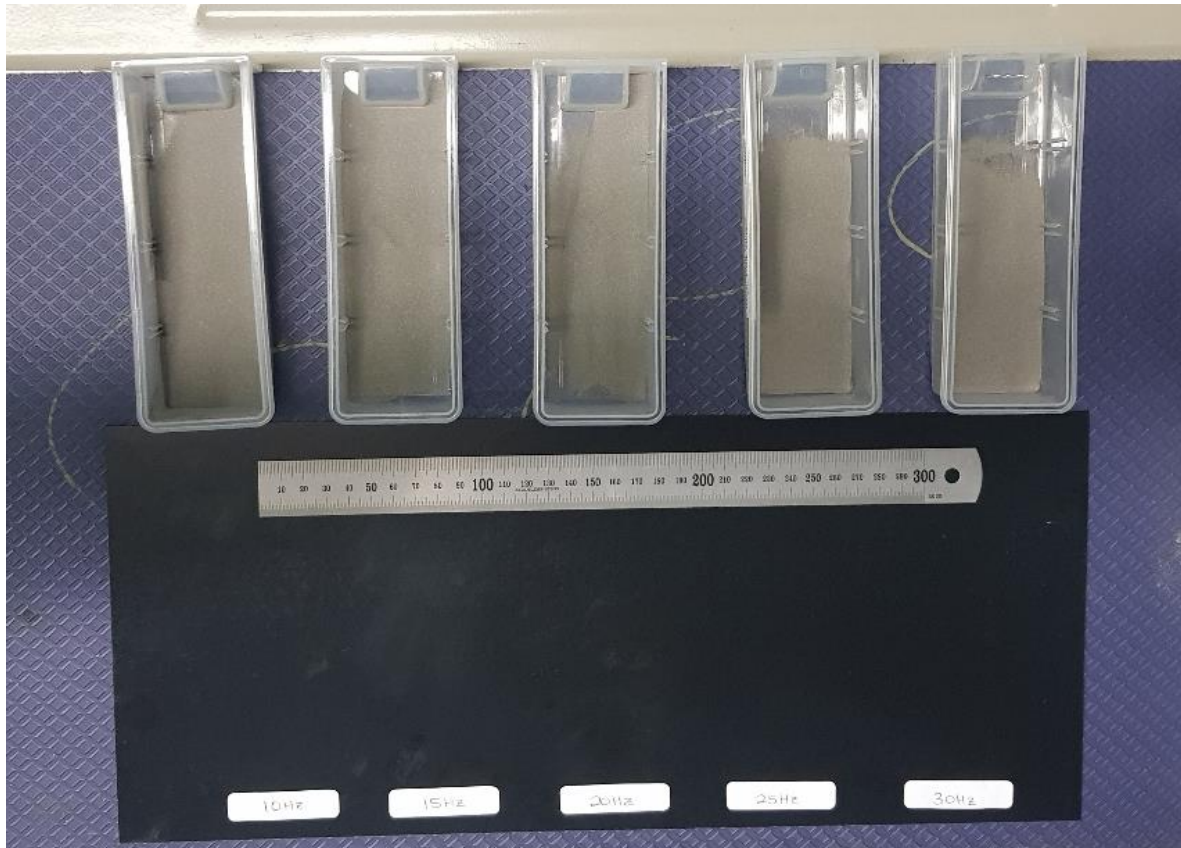


*Figure 140: Measured out powder samples for roll speed testing*

The roll gap was set using the screw adjustment mechanism. The mill was started, and the powder was fed to the rolls. The VSD frequency was varied for each sample to produce varying roll speeds in the mill. The compacts produced during this testing are shown in Figure 141.
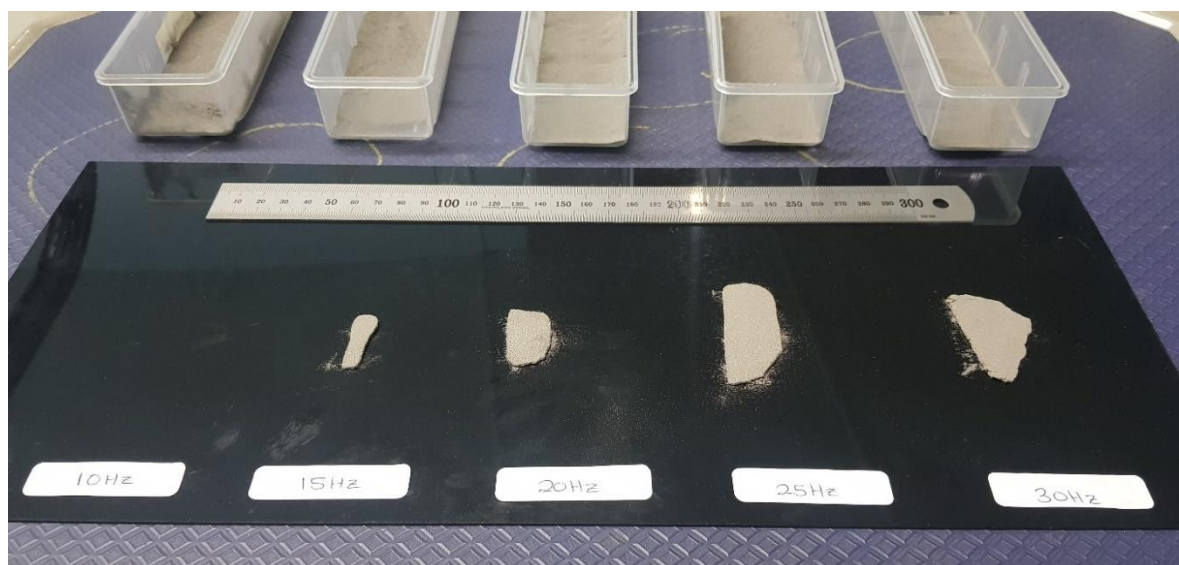


*Figure 141: Compacts produced at varying roll speeds: left to right: 3.4rpm, 5.0rpm, 6.6rpm, 8.2rpm, 9.8rpm (10 – 30Hz)*

Samples were then prepared from the compacts produced at different densities, as shown in Figure 142.
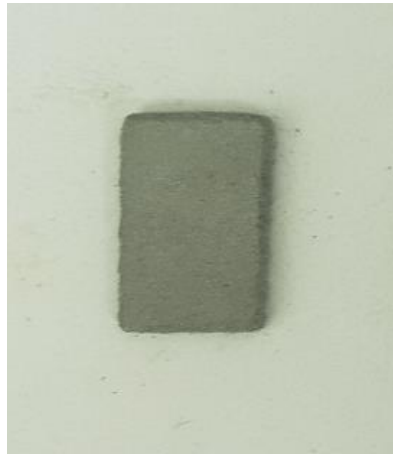


*Figure 142: Sample prepared for density measurements*

This was done to ensure ease and accuracy of density measurements, which as discussed was done using the mass of the compacts produced as well as their physical dimensions [66], since the compacts produced were not consistently sized.

A single sample was used for each data point during this test. This was simply a preliminary test to determine optimal rolling speeds for further testing, and thus did not justify the use of more of the expensive titanium feed material which was better used for further tests.

The results of this testing, for a VSD frequency range of 10Hz – 30Hz are shown in  Figure 143. Note that the roll speed range calculated as per Section 5.2. is 10 – 35Hz (equivalent to 3.4 – 11.4rpm), but a drop off in density was witnessed at speeds above 30Hz during the initial testing. The compacts produced at very high rolling speeds are thus not of much interest for the purposes of this research. This test was performed at a roll gap of 0.6mm.
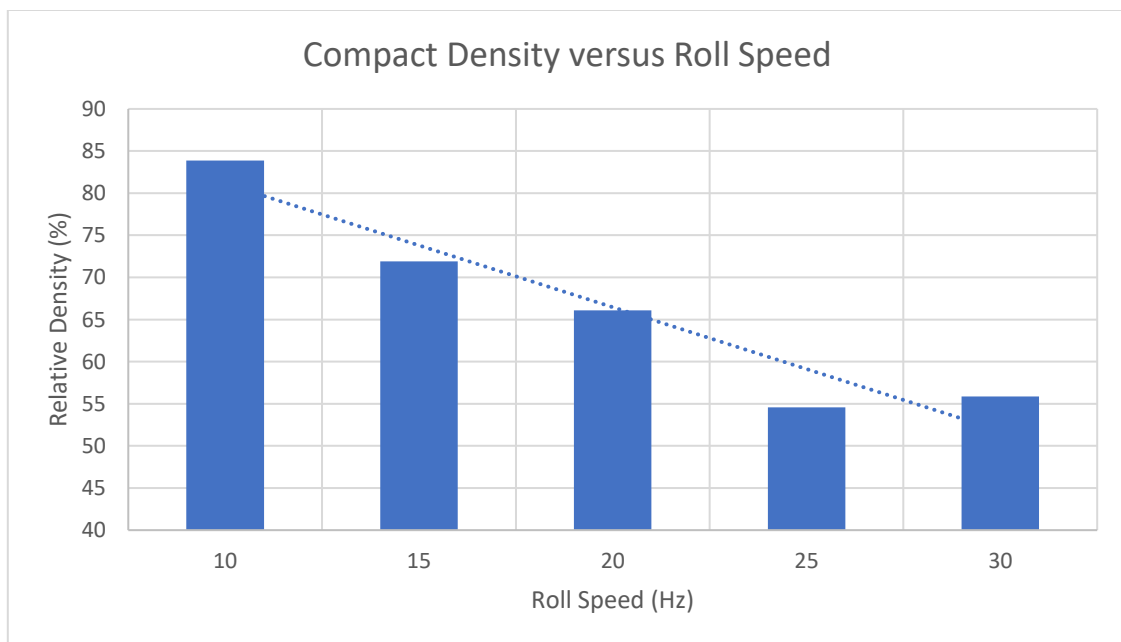


*Figure 143: Compact density versus roll speed, 0.6mm roll gap*

The densities of the compacts formed during this testing ranges from 3783 kg/m$^3$ for DPR at a roll speed of 3.4rpm/10Hz at the VSD to 2462 kg/m$^3$ for DPR with a roll speed of 8.2rpm/25Hz (30Hz at the VSD) (equivalent to 84 – 55% relative density).

As can be seen, the initial testing indicates inverse proportionality between the compact density and the roll speed. This was deduced to be due to:

1. The powder feed rate being constant for all roll speeds, which results in relatively less material being available for the rolling process at higher speeds [5] [66], exacerbated by

2. The higher proportion of powder leakage present at lower roll speeds, as witnessed in the initial testing of Section 6.2.1., and

3. The understanding that roll speeds that are too high allow do not allow for adequate compaction [66].

It hereby becomes apparent that what was initially assumed to be a gap in Johanson's model, of not considering the effect of the powder feed rate on the rolling mill behaviour [36] [73], may actually be a model assumption that for an optimal rolling process, there is always sufficient material available for the maximum calculated compaction.

A roll speed of 5.0rpm (15Hz at the VSD) was selected for further testing as the compacts formed at this rolling speed were dense enough to be handled (greater than the 65% as determined experimentally in Section 3.2.2) and large enough to easily re-feed through the mill and prepare samples for density measurements.

*Number of roll passes*

The method followed for this testing was identical to that of the roll speed testing in the following respects:

1. Preparation of 20g powder samples for each test

2. Adjustment of the roll gap for the testing using the screw mechanism

3. Control of the roll speed using the VSD

4. Preparation of the compacted samples for density measurements

The roll gap for this testing was set to 0.7mm, and the roll speed was set to 5.0rpm (15Hz at the VSD). The roll gap was increased slightly from the previous test due to the VSD cutting out on an overcurrent error when the compacted strips were fed through a roll gap of 0.6mm. However, the roll gap was kept consistent at 0.7mm throughout this test in order to witness the effect of varying only the number of passes through the mill.

The compacts formed from a single pass through the mill are formed directly from powder. The compacts formed at two and three passes through the mill are formed by re-rolling the compact formed through the mill a second and third time (respectively).

Three samples were prepared for each data point to improve result accuracy. The average density of the compacts formed at one pass, two passes, and three passes through the mill were then plotted as shown in Figure 144.
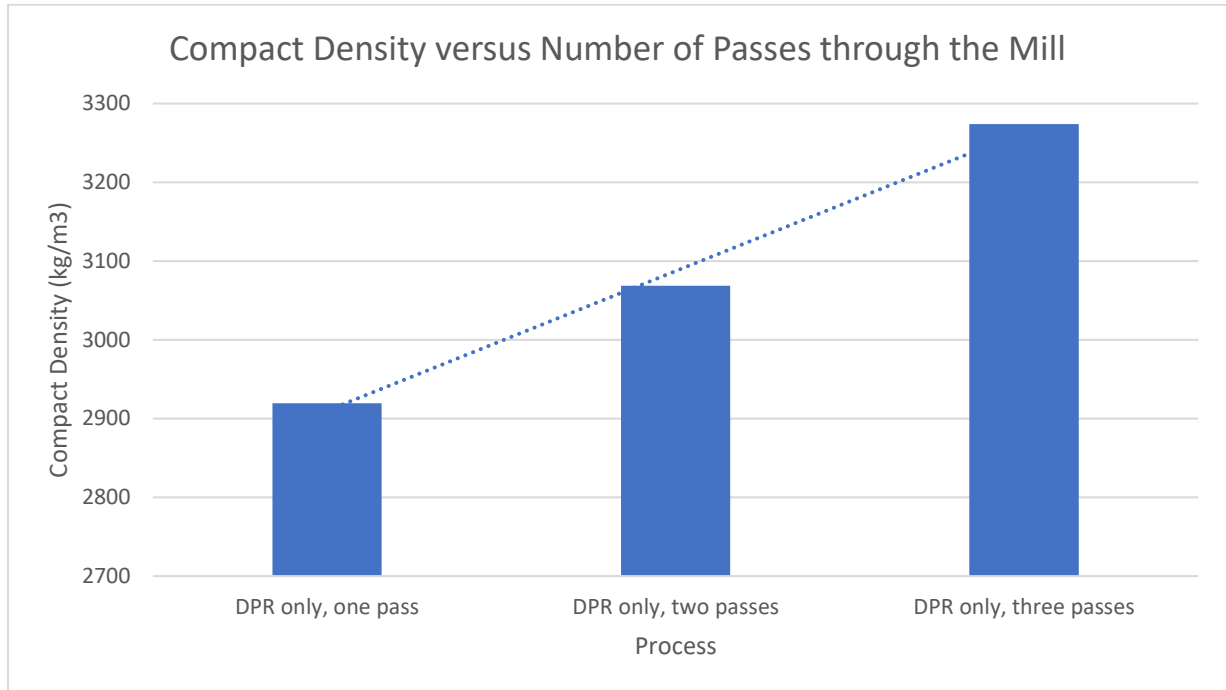


*Figure 144: Compact density versus number of passes, 07mm roll gap, 5rpm roll speed (15Hz)*

The average densities of the compacts formed during this testing ranges from 2919 kg/m$^3$ for DPR with a single pass through the mill to 3274 kg/m$^3$ for DPR with three passes through the mill (equivalent to 65 – 73% relative density).

As expected, the more times the material is fed through the mill, the higher the density of the green compact formed, even though the roll gap is not decreased for consecutive passes though the mill, since the thickness of the compact exceeds the roll gap.

*Roll gap*

The method followed for this testing was identical to that of the roll speed testing in the following respects:

1. Preparation of 20g powder samples for each test

2. Adjustment of the roll gap for the testing using the screw mechanism

3. Control of the roll speed using the VSD

4. Preparation of the compacted samples for density measurements

Three samples were prepared for each data point to improve result accuracy. The average density of the compacts formed at three different roll gaps were then plotted as shown in Figure 145. The roll speed was set to 6.6rpm (20Hz at the VSD) for this test to reduce the risk of the mill being overloaded at smaller roll gaps.
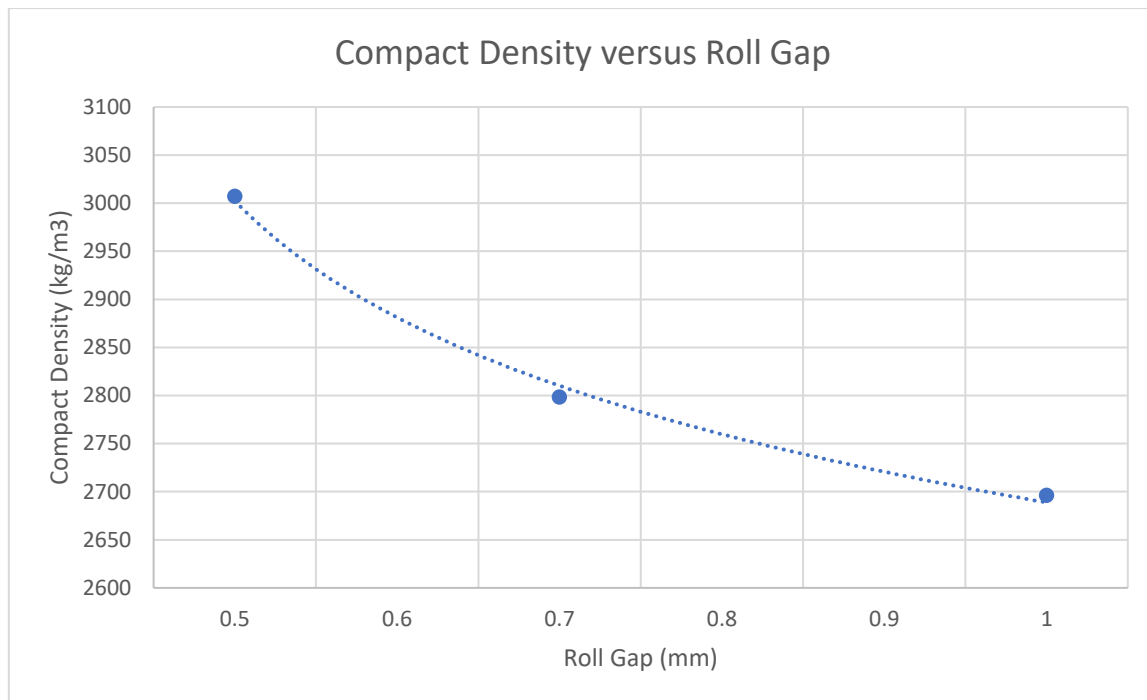


*Figure 145: Compact density versus roll gap,*

Rolling attempts at roll gaps below 0.5mm and above 1.0mm were unsuccessful at the roll speed of 6.6 rpm (20Hz at the VSD) used here. The mill was overloaded at roll gaps below 0.5mm (required torque from motor too high), and no compact was formed at roll gaps above 1.0mm (insufficient applied pressure to the sample).

The average densities of the compacts formed during this testing ranges from 3007 kg/m$^3$ for DPR at 0.5mm roll gap to 2696 kg/m$^3$ for DPR at 1.0mm roll gap (equivalent to 67 – 60% relative density).

The relationship between compact density and roll gap as shown in the figure above follows what is expected from the Johanson model as reviewed in Section 2.3.2.

## 6.3. Testing the DPR-SPS Process

As discussed in the previous chapter, there are many feasible options for supplying the SPS voltage across the compact. In order to test the current flow through the compact as a proof of concept for the SPS process, a lithium ion cell was used to provide the current.

The lithium ion cell has a nominal voltage of 3.2V with a maximum allowable continuous current draw of 280A.

### 6.3.1. Preliminary SPS Testing

In order to independently test the SPS system, a titanium compact which had already been formed through the DPR process was placed between the stationary rolls, as shown in Figure 146.



*Figure 146: Placement of green compact between the rolls for SPS testing*

The cell was then connected across the rolls through the carbon brush assembly. The visual results of the testing are shown in Figure 147.
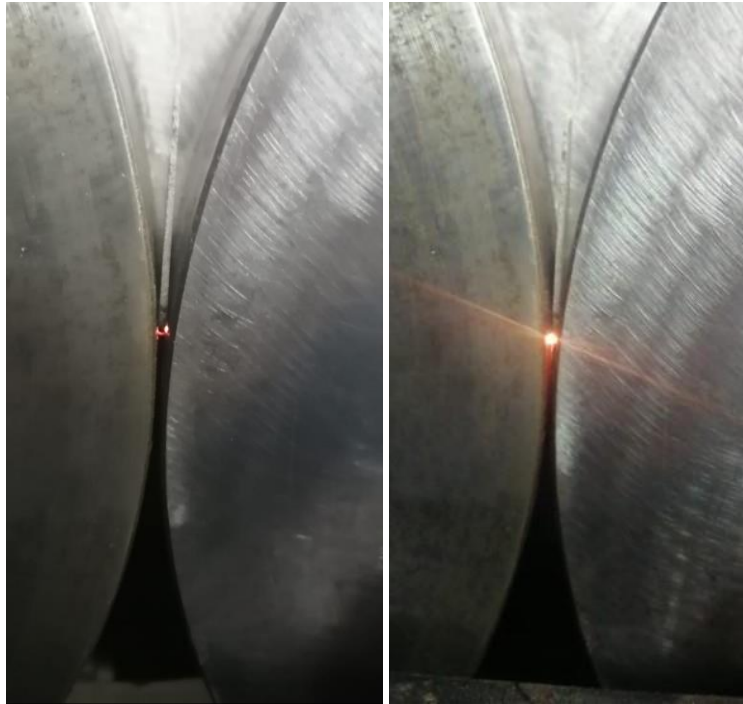


*Figure 147: Apparent sintering witnessed on application of SPS current*

The oxidation apparent on the compact after the application of SPS current is shown in Figure 148.



*Figure 148: Oxidation noted on compact after application of SPS current*

The SPS current through the circuit during sintering was measured using a clampmeter, as shown in Figure 149.



*Figure 149: SPS current measured during sintering, 32A at 3.3V*

The following observations were made during initial testing:

1. Apparent sintering of the compact was visually observed while the compact was between the rolls

2. Oxidation was visually observed on the compact once it was removed from the rolls

3. The current measured during sintering was much lower than that expected, with 30A being measured through the circuit

During fault-finding to determine the cause of the low current through the compact, it was noted that the resistance across the carbon brush interface, as measured by a multimeter, was higher than expected. This resistance was noted to decrease when a force was applied on the brush, towards to roll. This indicated that better seating of the carbon brush on the roll was required. This was achieved as described in Section 5.3.

The sequential DPR-SPS process was then tested by application of SPS into a previously formed green compact while the rolls were turning. Sintering appeared to occur in the DPR compact once it formed an electrical bridge between the rolls.

The simultaneous DPR-SPS process was then also tested by application of the SPS current directly to the powder during initial compaction through the rolls. Sintering was not visually apparent, but a current was measured through the circuit during the rolling process. This indicated that current was flowing through the powdered material during compaction.

The carbon brushes were well-placed; one of the reasons for placing the brushes on the sides of the rolls rather than on the periphery was the concern of powder interference with the brushes. During testing it was noted that there was powder residue on the rolling surfaces, which would have resulted in premature wear of the carbon brushes, as postulated in Section 4.4.9.

### 6.3.2. Testing of DPR versus DPR-SPS

Once the preliminary testing of the SPS system was completed and minor improvements to the system implemented, testing was done on the mill for the comparison of the DPR process to the DPR-SPS process.

For this testing, the roll gap was adjusted to 0.7mm (via the screw and shim mechanism) and the roll speed was adjusted to 15Hz (via the VSD). 20g of powder was used for each sample, and the mass and volume of each compact was measured using a sample prepared for the purpose of determining the compact density.

Four processes were compared here, as listed below:

1. DPR only, one pass: this compact is formed by feeding titanium powder through the mill

2. DPR only, two passes: this compact is formed by re-feeding the compact formed in (1) through the mill

3. DPR-SPS, one pass: this compact is formed by feeding titanium powder through the mill while applying a current across the rolls

4. DPR-SPS, two passes; this compact is formed by re-feeding the compact formed in (1) through the mill while applying a current across the rolls

In order to determine the effect of adding SPS to the process, the results of (1) and (3) should be compared to each other, and the results of (2) and (4) should be compared to each other. In order to determine the effect of applying the SPS process either simultaneously or sequentially with the DPR process, the results of (3) and (4) should be compared to each other.

Three samples were prepared for each data point to improve result accuracy. The average density of the compacts formed using the different processes described above were then plotted as shown in Figure 150.
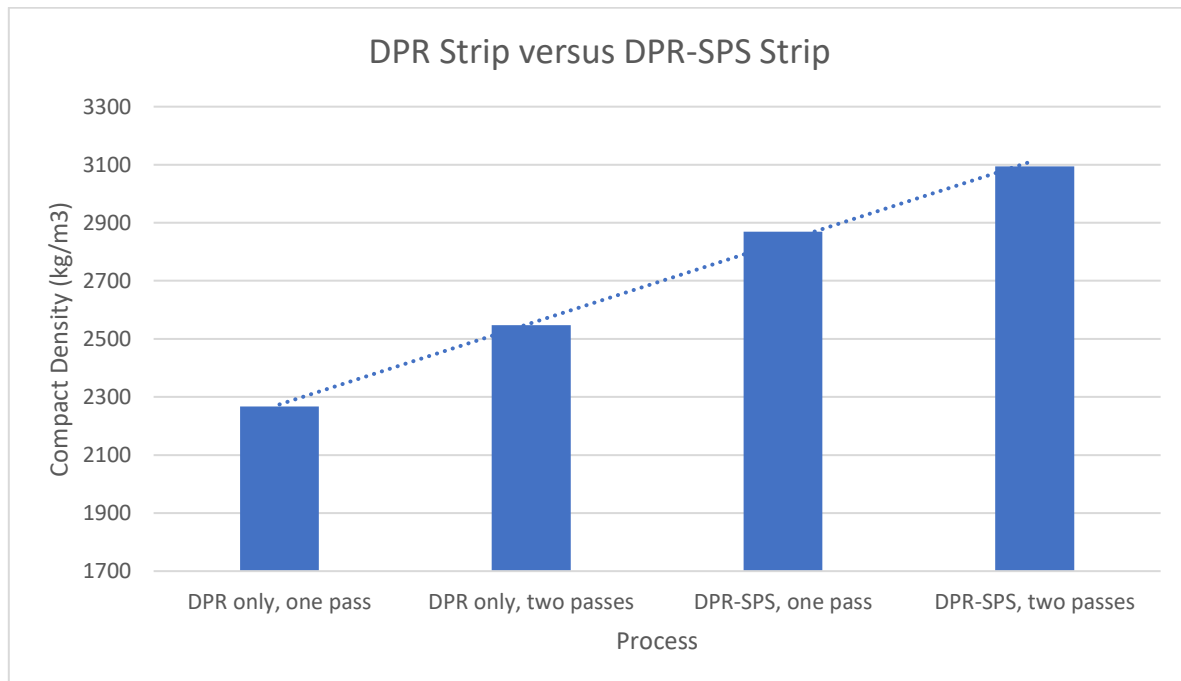


*Figure 150: DPR strip versus DPR-SPS strip*

The average densities of the compacts formed during this testing ranges from 2267 kg/m$^3$ for DPR only with a single pass through the mill to 3094 kg/m$^3$ for sequential DPR-SPR with two passes through the mill (equivalent to 50 – 69% relative density).

The SPS process was observed to have a favourable effect on the density of the compact formed, regardless of whether the process was applied simultaneously or sequentially with the DPR process. This can be seen by the comparison of (1) and (3), and (2) and (4) above, respectively. The improvement in theoretical density of the compact with application of SPS (versus DPR only) was 14% for simultaneous DPR-SPS and 11% for sequential DPR-SPS.

It is also noted that the most dense compact was formed when the SPS process follows the DPR process, as can be seen through comparison of (3) and (4) above. This is to be expected, as a second pass through the mill introduces further densification as discussed in Section 6.2.3.

Finally, it is noted that applying the SPS process to the sample improved the density of a compact formed from one pass through the mill beyond that of a compact formed from two passes through the mill without the application of SPS. This is a significant research observation.

## 6.4. Summary of DPR and SPS Testing

Once the mill was commissioned, initial testing was performed on the mill gain to familiarity with the functionality of the mill, its capabilities, and its limitations. Once the initial testing was completed and relevant observations and adjustments made, the parametric testing of the DPR-SPS mill was then performed, with the DPR and SPS processes being tested independently, sequentially and simultaneously.

The following parametric testing was performed on the DPR-SPS mill.

1. For the DPR testing (without SPS), to determine the effect of each parameter on the density of the compact formed, the following parameters were adjusted:

    a. Roll speed

    b. Number of roll passes

    c. Roll gap

2. For the SPS process, to determine the effect of application of SPS current to the titanium sample during the rolling process, the following processes were tested:

    a. Application of SPS to titanium powder (simultaneous process), and

    b. Application of SPS to titanium green compacts (sequential process

The following observations were made during this testing:

1. The compact density is inversely proportional to

    a. The roll speed

    b. The roll gap

2. The compact density is proportional to the number of passes through the mill

3. The compact width is proportional to the rolling speed

4. A favourable effect on the density was observed with the application of SPS current (compared to control samples which did not have SPS current applied to them), when conducted on

    a. A simultaneous DPR-SPS process

    b. A sequential DPR-SPS process

These results of the DPR testing were all as expected from the literature reviewed in Section 2.3. Although the results of the DPR-SPS testing could not directly be compared to previous literature as this exact process has not been conducted before, it was expected that the SPS process would improve the density of a compact, as reviewed in Section 2.4.

# 7. Conclusions and Recommendations

This is the final chapter of the dissertation, and provides a summary of the work done. The chapter begins with a discussion of the objectives achieved, which follow those as laid out in the first chapter, then provides some recommendations for future work, and finally presents concluding remarks.

## 7.1. Objectives Achieved

The primary objective of this research was to contribute to the development of improved titanium powder processing, which has been achieved through the design, manufacture and parametric testing of an SPS-DPR mill.

The specific research objectives as laid out at commencement of the project, as listed in Section 1.2, have been achieved as follows:

1. As described in Chapter 3, experimental testing was performed on titanium powder samples to determine the powders' properties, namely

   a. The initial density characteristics for seven different powders through preliminary testing

   b. The compressibility factor for the three most suitable powders, as selected from the preliminary testing, through uniaxial compression testing

   c. The effective angle of internal friction and angle of wall friction for the most suitable powder, as selected from the uniaxial compression testing, through shear box testing

2. As described in Section 4.3., numeric computing software was used to model the rolling mill behaviour, based on the properties of the mill and the powder being rolled, to determine

   a. The nip angle of the mill, for the specific powder being rolled

   b. The pressure distribution between the mill rolls

   c. The roll separating force in the mill

   d. The required roll torque for the mill

   e. The theoretical density of the compact formed at various roll gaps

3. As described in Section 4.4., 3D modelling software was used to design and model a rolling mill to be used for titanium powder processing, including

   a. A rolling mill frame, including integration of the mechanical drive system

   b. Bearings used to support the mill drive assembly

   c. A powder hopper for feeding powder to the rolls

   d. Cheek plates for limiting powder leakage from the sides of the rolls

   e. Carbon brushes for application of SPS current to the mill rolls

4. As described in Section 4.5., engineering simulation software was used to conduct finite element analysis on the designed components deemed to be highly stressed or deformed during operation, namely

    a. The rolling mill frame

    b. The rolls, roll shafts, and bearings

    c. The cheek plates

5. As described in Section 4.6., various circuits were designed to provide a suitable electrical current for spark plasma sintering of titanium, including

    a. A low voltage pulsed smoothed DC SPS circuit with secondary rectification

    b. A low voltage pulsed smoothed DC SPS circuit with primary rectification

    c. A low voltage continuous smoothed DC SPS circuit.

    d. A low voltage continuous sinusoidal DC SPS circuit

    e. A low voltage AC SPS circuit

    f. A low voltage continuous DC SPS circuit, from a DC source

6. As described in Chapter 5, the designed direct powder rolling mill and its spark plasma sintering circuit were manufactured and commissioned

7. As described in Chapter 6, parametric testing of the mill was conducted through production of

    a. DPR titanium strip under varying conditions, and

    b. DPR-SPS titanium strip under varying conditions

8. As described in Chapter 6, the DPR process was compared to the DPR-SPS process through determining

    a. The density of the green strip produced (i.e. the DPR titanium strip), and

    b. The density of the sintered strip produced (i.e. the DPR-SPS titanium strip)

During testing of the mill, it was determined that the DPR and SPS processes can successfully be combined and applied to produce titanium sheet. Testing was promising for both a two-step process (sequential DPR and SPS) and a one-step process (simultaneous DPR and SPS); in both cases, improved density was observed compared to DPR only. Higher currents were witnessed using simultaneous versus sequential testing; this is considered to be at least partly due to the variation in width across which the sintering was conducted, as there was a narrower titanium bridge between the rolls when sintering the green compacts compared to when sintering the powder directly. A larger cross-sectional area across which current can flow will result in a lower circuit resistance, and thus a higher magnitude of current at the constant induced voltage.

## 7.2. Recommendations for Future Work

### 7.2.1. Further Design and Testing

It is recommended that the following design aspects of the mill be further explored with a view to improvement of the existing system and its contribution to the field.

1. Expanded modelling of the thermal behaviour of the SPS system, as discussed in Section 4.6.4.

2. Modelling and manufacture of a gas shielding or containment system for the SPS process, as discussed in Section 2.2.1., including (if applicable) simulation of inert gas flow through the nozzles of the shielding system

3. Experimentation with different SPS waveforms and comparison thereof, through manufacture and testing of the range of SPS systems discussed in Section 4.6.3.

### 7.2.2. General Improvements to the Existing Design

As discussed during the lessons learned while commissioning, in Section 5.3., there are certain aspects of the design that can be improved. These are summarised here:

1. The screw adjustment mechanism for the roll gap should be made more user friendly

2. The termination points of the carbon brushes should tamped rather than threaded

3. The motor axial alignment, and thus complete electrical isolation from the SPS system, should be corrected at the motor coupling

### 7.2.3. Comprehensive Testing of the Mill

The mill has been designed such that comprehensive parametric testing of both processes can be easily implemented. Further testing, and verification of data-points via more extensive testing, should be performed. This comprehensive testing may include:

1. For the DPR process
   a. The use of different input powders
   b. Varying the powder feed rate

2. For the SPS process
   a. The use of an inert gas environment during sintering (and varying the parameters thereof)
   b. Varying the parameters of the SPS system, such as
      i. The current waveform (AC vs constant DC vs pulsed DC), and
      ii. The current intensity

During comprehensive testing of the mill, the aim would typically be for the rolled and sintered compact to have the following characteristics:

1. High density

2. High ductility

3. Low oxide level

As has been discussed in detail in both the literature review and design chapters (Chapters 2 and 4), for a direct powder rolling process where both the powder and mill characteristics are known, the density of the rolled strip can be controlled through control of process parameters – the most notable of which is the normal stress created on the powder by the rolling process. This stress is related to the roll gap through the compressibility relationship for the powder. However, the roll gap is easier to measure (and directly control) than the normal stress, and is thus a better process control variable [71].

## 7.3. Concluding Remarks

An SPS-DPR mill was designed, manufactured and parametrically tested using titanium powder.

Parametric testing (conducted as discussed in Chapter 6) indicated good correlation between the actual performance of the mill versus what was expected from literature (as reviewed in Section 2.3 and Section 2.4).

For the DPR only process, the density of the titanium compact was improved through adjustments to the roll speed, number of passes through the mill, and the roll gap, with a maximum density of 84% being achieved for the as-rolled titanium compact.

For the SPS process, the density of the titanium compact was improved through the use of sequential versus simultaneous DPR-SPS, although both sequential and simultaneous application of SPS current notably improved the density of the DPR compact (versus DPR only). The improvement in theoretical density of the compact with application of SPS (versus DPR only) was 14% for simultaneous DPR-SPS and 11% for sequential DPR-SPS.

The results show promise for the DPR-SPS process to significantly contribute to the efficiency of titanium sheet metal production, through a previously unknown continuous method of titanium processing, directly from the titanium powder produced via beneficiation processes (discussed in Section 2.1.). This could have a meaningful benefit for the South African economy.

Significant experience was gained in the knowledge and mastery of engineering in multidisciplinary fields. Insight was gained in experimental powder analysis, numerical modelling, finite element analysis, 3D modelling, electrical circuit simulation, parametric set up of variable speed drives, mechanical and electrical manufacturing processes, parametric experimental testing processes and in analysis.

The project has satisfied the objectives as laid out upon its commencement, and has the potential to make a valuable contribution to the field. There are many possibilities for the improvement of the mill and of the DPR-SPS processes, and significant further testing should be performed. The mill may be used for varied applications in future research work.

# Bibliography

[1]   E. Uheida, D. Dimitrov, G. Oosthuizen, D. Blaine, R. Laubscher, A. Sterzing, P. Blau, W. Gerber and O. Damm, "Manufacturing of High Added Value Titanium Components. A South African Perspective," in *Materials Science and Engineering*, Vanderbijlpark, 2018.

[2]   W. Preez, O. Damm and D. Vuuren, "Progress towards a Titanium Metal Industry for South Africa," in *World Conference on Titanium*, 2011.

[3]   W. Preez, *Beneficiation of South Africa's Titanium Resource,* Free State: Central University of Technology, 2014.

[4]   G. Lutjering and J. Williams, Titanium, Springer, 2007.

[5]   Y. Zhang, "A Study of Direct Powder Rolling Route for Cp-Titanium," Centre for Material Engineering (UCT), Cape Town, 2010.

[6]   Z. Fang, J. Paramore, P. Sun, K. Chandran, Y. Zhang, Y. Xia, F. Cao, M. Koopman and M. Free, "Powder Metallurgy of Titanium - Past, Present and Future," *International Materials Reviews,* vol. 63, no. 7, pp. 407-459, 2018.

[7]   S. Oosthuizen, "In Search of Low Cost Titanium: The Fray Farthing Chen (FFC) Cambridge Process," in *The South African Institute of Mining and Metallurgy, Advanced Metals Initiative, Light Metals Conference*, 2010.

[8]   P. Cavaliere, B. Sadeghi and A. Shabani, "Spark Plasma Sintering: Process Fundamentals," in *Spark Plasma Sintering of Materials*, Springer Nature Switzerland AG, 2019, pp. 3-20.

[9]   R. Orru, R. L. A. Locci, A. Cincotti and G. Cao, "Consolidation/Synthesis of Materials by Electric Current Activated/Assisted Sintering," *Materials Science and Engineering,* vol. 63, pp. 127-287, 2009.

[10]  F. Kellogg and C. Mock, "The Effect of Current Pathways on Spark Plasma Sintering," in *Spark Plasma Sintering of Materials*, Springer Nature Switzerland AG, 2019, pp. 61-92.

[11]  Z. Shen, M. Johnsson, Z. Zhao and M. Nygren, "Spark Plasma Sintering of Alumina," *Journal of the American Ceramic Society,* vol. 82(8), pp. 1921-1927, 2002.

[12]  D. Giuntini, J. Raethel, M. Hermann, A. Michaelis and E. Olevsky, "Advancement of Tooling for Spark Plasma Sintering," *Journal of the American Ceramic Society,* vol. 98, no. 11, pp. 3529-3537, 2015.

[13]  H. Wang, Z. Fang and P. Sun, "A Critical Review of Mechanical Properties of Powder Metallurgy Titanium," *International Journal of Powder Metallurgy,* vol. 46, no. 5, pp. 45-57, 2010.

[14]  V. Moxson and V. Duz, "Process of Direct Powder Rolling of Blended Titanium Alloys, Titanium Matrix Composites, and Titanium Aluminides". United States Patent US 2006/0147333 A1, 6th July 2006.

[15]  V. Moxson and V. Duz, "A Process of Direct Powder Rolling of Blended Titanium Alloys, Titanium Matrix Composites, and Titanium Aluminides". United States Patent US 7,311,873 B2, 25th December 2007.

[16]  "Titanium," Encylcopaedia Britannica, [Online]. Available: https://www.britannica.com/science/titanium. [Accessed 23rd May 2020].

[17]  T. Motsai, S. Chikosha, C. Machio and M. Makhatha, "A Comparative Study of Oxygen Pick-up of TiHDH Powder During Press and Sinter and Loose Sintering Processing," in *Materials Science and Engineering*, Vanderbijlpark, 2018.

[18]  G. Chen, D. Fray and T. Farthing, "Direct Electrochemical Reduction of Titanium Dioxide to Titanium in Molten Calcium Chloride," *Nature,* vol. 407, pp. 361-364, 2000.

[19]  W. Kroll, "The Production of Ductile Titanium," *Transactions of The Electrochemical Society,* vol. 78, no. 1, pp. 35-47, 1940.

[20]  M. Qian, G. Schaffer and C. Bettles, "Sintering of Titanium and its Alloys," in *Sintering of Advanced Materials - Fundamentals and Processes*, 2010, pp. 324-355.

[21]  C. Leyens and M. Peters, Titanium and Titanium Alloys: Fundamentals and Applications, Wiley, 2003.

[22]  J. Williams and A. Belov, Titanium and Titanium Alloys, New York: Springer, 1982.

[23]  G. Cantin and M. Gibson, "Titanium Sheet Fabrication from Powder," in *Titanium Powder Metallurgy*, Elsevier, 2015, pp. 383-403.

[24]  X. Goso and A. Kale, "Production of Titanium Metal Powder by the HDH Process," *The Journal of the Southern African Institute of Mining and Metallurgy,* vol. 111, pp. 203-210, 2011.

[25]  G. Cantin, P. Kean, N. Stone, R. Wilson, M. Gibson, D. R. M Yousuff and R. Rajakumar, "Innovative Consolidation of Titanium and Titanium Alloy Powders by Direct Rolling," *Powder Metallurgy,* vol. 54, no. 3, pp. 188-192, 2011.

[26]  A. Harooni, "Comparison of Nozzle Gas Shielding Techniques for Laser Cladding of Zirconium," 2015.

[27]  G. Upadhyaya, Powder Metallurgy Technology, Cambridge International Science Publishing, 1997.

[28]  R. German, Powder Metallurgy Science, Metal Powder Industries Federation, 1994.

[29]  G. DeGroat, "One-Shot Powder Metal Parts," *American Machinist,* vol. 109, no. 21, pp. 107-109, 1965.

[30]  G. DeGroat, *American Machinist,* vol. 110, p. 135, 1966.

[31]  K. Inoue, "Electric-Discharge Sintering". United States Patent 3241956, 22 March 1966.

[32]  K. Inoue, "Servocontrol System for Discharge Sintering". United States Patent 3508029, 21 April 1970.

[33] Z. Munir, U. Anselmi-Tamburini and M. Ohyanagi, "The Effect of Electric Field and Pressure on the Synthesis and Consolidation of Materials: A Review of the Spark Plasma Sintering Method," *Journal of Materials Science,* vol. 41, pp. 763-777, 2006.

[34] P. Guigon and O. Simon, "Roll Press Design - Influence of Force Feed Systems on Compaction," *Powder Technology,* vol. 130, pp. 41-48, 2003.

[35] H. Ro, M. Toaz and V. Moxson, "The Direct Powder-Rolling Process for Producing Thin Metal Strip," *Journal of Metals,* vol. 35, pp. 34-39, 1983.

[36] J. Johanson, "A Rolling Theory for Granular Solids," *Journal of Applied Mechanics,* vol. 32(4), pp. 842-848, 1965.

[37] B. Kurtz, "Compacting Granular Solids," *Chemical Engineering Progress,* vol. 56, pp. 67-72, 1960.

[38] R. Smucker, "Perfected and Practical Methods of Processing Powder Into Commercial Strip," *Iron and Steel Engineer Year Book,* p. 562, 1958.

[39] P. Kleinebudde, J. Khinast and J. Rantanen, Continuous Manufacturing of Pharmaceuticals, Chennai: Wiley, 2017.

[40] W. Jenike and R. Shield, "On the Pastic Flow of Coulomb Solids Beyond Original Failure," *Journal of Applied Mechanics,* vol. 26, pp. 599-602, 1959.

[41] G. Bindhumadhavan, J. Seville, M. Adams, R. Greenwood and S. Fitzpatrick, "Roll Compaction of a Pharmaceutical Excipient: Experimental Validation of Rolling Theory for Granular Solids," *Chemical Engineering Science,* vol. 60, pp. 3891-3897, 2005.

[42] V. Mamedov, "Spark Plasma Sintering as Advanced PM Sintering Method," *Powder Metallurgy,* vol. 45, no. 4, pp. 322-328, 2002.

[43] R. Chaudhari and R. Bauri, "Microstructure and Mechanical Properties of Titanium Processed for Spark Plasma Sintering (SPS)," *Metallography, Microstructure and Analysis,* vol. 3, pp. 30-35, 2014.

[44] P. Phillips, Electrical Principles, Cengage AU, 2019.

[45] R. Dean, J. Long, F. Wartman and E. Anderson, "Preparation and Properties of Ductile Titanium," *Transactions of the American Institute of Mining, Metallurgical and Petroleum Engineers,* vol. 166, pp. 369-381, 1946.

[46] S. Song, Z. Wang and G. Shi, "Heating Mechanism of Spark Plasma Sintering," *Ceramics International,* vol. 39, pp. 1393-1396, 2013.

[47] E. Weisstein, "Fourier Series - Square Wave," MathWorld - A Wolfram Web Resource, [Online]. Available: https://mathworld.wolfram.com/FourierSeriesSquareWave.html. [Accessed 31 May 2020].

[48] A. d'Adrian, "Article of Fused Metallic Oxide and Process of Producing the Same". United States Patent 1430724, 3 October 1922.

[49] S. Hoyt, "Hard Metal Composition and Method of Making the Same". United States Patent 1843768, 2 February 1932.

[50] G. Taylor, "Apparatus for Making Hard Metal Compositions". United States Patent 1896854, 7 February 1933.

[51] G. Cremer, "Powder Metallurgy". United States Patent 2355954, 15 August 1944.

[52] W. Ross, "Method and Apparatus for Making Solid Objects from Metal Powder". United States Patent 2372605, 27 March 1945.

[53] R. Balaguer, "Method of Making Carbon Articles". United States Patent 3001237, 26 September 1961.

[54] K. Inoue, "Apparatus for Electrically Sintering Discrete Bodies". United States Patent 3250892, 10 May 1966.

[55] R. Boesel, M. Jacobson and I. Yoshioka, *Materials Engineering,* vol. 70, p. 32, 1969.

[56] C. Goetzel and V. D. Marchi, *Powder Metallurgy International,* vol. 3, 1971.

[57] H. Zenshiro and A. Kiyoaki, *Journal of the Japan Society of Powder and Powder Metallurgy,* vol. 24, pp. 16-22, 1977.

[58] H. Zenshiro and A. Kiyoaki, *Journal of the Japan Society of Powder and Powder Metallurgy,* vol. 25, p. 193, 1978.

[59] H. Zenshiro and A. Kiyoaki, *Journal of the Japan Society of Powder and Powder Metallurgy,* vol. 25, p. 198, 1978.

[60] H. Zenshiro and A. Kiyoaki, *Journal of the Japan Society of Powder and Powder Metallurgy,* vol. 26, p. 180, 1979.

[61] C. Liu and P. Kao, *Scripta Metallurgica et Materiala,* vol. 24, p. 2279, 1990.

[62] O. Guillon, J. Gonzalez-Julian, B. Dargatz, T. Kessel, G. Schierning, J. Rathel and M. Hermann, "Field-Assisted Sintering Technology/Spark Plasma Sintering: Mechanisms, Materials, and Technology Developments," *Advanced Engineering Materials,* vol. 16, no. 7, pp. 830-849, 2014.

[63] F. Zhang, Y. Quan, M. Reich, O. Kessler and E. Burkel, "Sintering and Heat Treatment of Titanium Alloys by Pulsed Electric Current Sintering," in *Sintering Applications*, IntechOpen, 2013, pp. 259-283.

[64] M. Asl, A. Namini, A. Motallebzadeh and M. Azadbeh, "Effects of Sintering Temperature on Microstructure and Mechanical Properties of Spark Plasma Sintered Titanium," *Materials Chemistry and Physics,* vol. 203, pp. 266-273, 2018.

[65] M. Eriksson, "Spark Plasma Sintering and Deformation Behaviour of Titanium and Titanium/TiB2 Composites," Stockholm University Division of Inorganic Chemistry, Stockholm, 2007.

[66] N. Muchavi, S. Chikosha, H. Chikwanda and E. Makhatha, "Determination of Roll Compaction Parameters Required for High Green Density, Defect Free Ti-6Al-4V Strips," in *Materials Science and Engineering*, Vanderbijlpark, 2018.

[67] J. Schwedes and D. Schulze, "Measurement of Flow Properties of Bulk Solids," *Powder Technology,* vol. 61, pp. 59-68, 1990.

[68] S. Joo, H. Chang, W. Bang, N. Nan and K. Oh, "Analysis of Alligatoring Behavior during Roll Pressing of DRI Powder with Flat Roller and Indentation-type Roller," *Materials Science Forum,* Vols. 475-479, pp. 3223-3226, 205.

[69] S. Chikosha, R. Machaka and H. Chikwanda, "Evaluating the Johanson Theory for Titanium Powder," *Materials Science Forum,* Vols. 828-829, pp. 447-452, 2015.

[70] S. Ramlall, G. Hoskins, N. Moodley and J. Nagiah, "Design and Research Project Final Semester Report," University of KwaZulu-Natal, Discipline of Mechanical Engineering, Durban, 2017.

[71] O. Simon and P. Guigon, "Interaction between Feeding and Compaction During Lactose Compaction in a Laboratory Roll Press," *KONA,* vol. 18, pp. 131-138, 2000.

[72] AWS D1.1: Structural Welding Code - Steel, American Welding Society, 2020.

[73] M. Balicki, "Numerical Methods for Predicting Roll Press Powder Compaction Parameters," Ecole Des Mines D'Albi-Carmaux, Albi, 2003.

[74] E. Maynard, "Ten Steps to an Effective Bin Design," *American Institute of Chemical Engineers,* vol. Nov, pp. 25-32, 2013.

[75] G. Haeffler, L. Schmidt, S. Lakio, G. Reynolds, J. Odman and P. Tajarobi, "A Systematic Study of the Impact of Changes of Roller Compactor Equipment on Granule and Tablet Properties," *Powder Technology,* vol. 341, pp. 11-22, 2018.

[76] H. Ananian, D. Robertson, W. Shirry and J. Ward, "Pulse Electrical Current Assisted Sinter Rolling Mill," McGill University , Montreal, 2010.

[77] "Timken Quick-Flex Couplings Brochure," [Online]. Available: https://www.timken.com/pdf/10426_QuickFlex%20Couplings%20Brochure.pdf. [Accessed 23 June 2020].

[78] V. Bhandari, Design of Machine Elements, Pune: Tata McGraw-Hill, 2007.

[79] "Beams - Fixed at Both Ends - Continuous and Point Loads," Engineering Toolbox, [Online]. Available: https://www.engineeringtoolbox.com/beams-fixed-both-ends-support-loads-deflection-d_809.html. [Accessed 30 June 2020].

[80] R. Juvinall and K. Marshek, Fundamentals of Machine Component Design, New Jersey: Wiley, 2006.

[81] N. Chawake, L. Pinto, A. Srivastav, K. Akkiraju, B. Murty and R. Kottada, "On Joule Heating During Spark Plasma Sintering of Metal Powders," *Scripta Materialia,* vol. 93, pp. 52-55, 2014.

[82] "Calculation Data: Power Handling Capacity - E-Core," Eilor, 2017. [Online]. Available: https://eilor.co/calculation-data/. [Accessed 8 June 2020].

[83] F. Kellogg, M. Kornecki, S. Raju, B. McWilliams and R. Brennan, "Comparison of AC to DC Current Sources for Field-Assisted Sintering of Aluminium Alloy 5083 Powder," *Journal of the American Ceramic Society,* vol. 102, no. 2, pp. 621-627, 2018.

[84] J. O'Flynn and S. Corbin, "Effects of Powder Material and Process Parameters of the Roll Compaction, Sintering and Cold Rolling of Titanium Sponge," *Powder Metallurgy,* 2019.

[85] N. Park, J. Kim and J. Hong, "Characteristics of Powder-Rolled and Sintered Sheets Made from HDH Ti Powders," *Key Engineering Materials,* vol. 520, pp. 281-288, 2012.

[86] K. Sommer and G. Hauser, "Flow and Compression Properties of Feed Solids for Roll-Type Presses and Extrusion Presses," *Powder Technology,* vol. 130, pp. 272-276, 2003.

[87] O. Simon and P. Guigon, "Correlation between Powder-Packing Properties and Roll Press Compact Heterogeneity," *Powder Technology,* vol. 130, pp. 257-264, 2003.

[88] M. Bagheripoor and H. Bisadi, "An Investigation on the Roll Force and Torque Fluctuations during Hot Strip Rolling Process," *Production and Manufacturing Research,* vol. 2, no. 1, pp. 128-141, 2014.

[89] D. Bland and H. Ford, "The Calculation of Roll Force and Torque in Cold Strip Rolling with Tensions," *Proceedings of the Institution of Mechanical Engineers,* vol. 159, pp. 144-163, 1948.

[90] I. Robertson and G. Schaffer, "Refinement of Master Densification Curves for Sintering of Titanium," *Metallurgical and Materials Transactions,* vol. 41A, pp. 2949-2958, 2010.

[91] H. Su and D. Johnson, "Master Sintering Curve: A Practical Approach to Sintering," *Journal of the American Ceramic Society,* vol. 79, pp. 3211-3217, 1996.

[92] I. Robertson and G. Schaffer, "Comparison of Sintering of Titanium and Titanium Hydride Powders," *Powder Metallurgy,* vol. 53, no. 1, pp. 12-19, 2010.

[93] I. Robertson and G. Schaffer, "Some Effects of Particle Size on the Sintering of Titanium and a Master Sintering Curve Model," *Metallurgical and Materials Transactions,* vol. 40A, pp. 1968-1979, 2009.

[94] O. Guillon and J. Langer, "Master Sintering Curve Applied to the Field-Assisted Sintering Technique," *Journal of Materials Science,* vol. 45, pp. 5191-5195, 2010.

[95] P. Christensen, H. Everfelt and N. Bay, "Pressure Distribution in Plate Rolling," *Annals of the CIRP,* vol. 35, no. 1, pp. 141-146, 1986.

[96] E. Olevsky, "Theory of Sintering: From Discrete to Continuum," *Materials Science and Engineering,* vol. 23, pp. 41-100, 1998.

[97] D. Yang and H. Conrad, "Enhanced Sintering Rate of Zirconia (3Y-TZP) by Application of a Small AC Electric Field," *Scripta Materialia,* vol. 63, pp. 328-331, 2010.

[98]  J. Fisher, "Calculation of Diffusion Penetration Curves for Surface and Grain Boundary Diffusion," *Journal of Applied Physics,* vol. 22, no. 1, pp. 74-77, 1951.

[99]  C. Herzig and Y. Mishin, "Grain Boundary Diffusion in Metals," 2005, pp. 337-366.

[100] M. Qian, Y. Yang and S. Luo, "Pressureless Sintering of Titanium and Titanium Alloys: Sintering Densification and Solute Homogenization," in *Titanium Powder Metallurgy: Science, Technology and Applications*, Butterworth-Heinemann, 2015, pp. 201-218.

[101] F. Djavanroodi and M. Janbakhsh, "Formability Characterization of Titanium Alloy Sheets," in *Titanium Alloys - Advances in Properties Control*, IntechOpen, 2013, pp. 81-113.

[102] J. Duroudier, "Stresses in Hoppers and Silos: Filling, Emptying and Content Homogeneity," in *Divided Solids Mechanics*, ISTE Press - Elsevier, 2016, pp. 57-87.

[103] U. Anselmi-Tamburini, S. Gennari, J. Garay and Z. Munir, "Fundamental Investigations on the Spark Plasma Sintering/Synthesis Process II. Modelling of Current and Temperature Distributions," *Materials Science and Engineering,* vol. 394, pp. 139-148, 2005.

[104] V. Thayalan and R. Landers, "Regulation of Powder Mass Flow Rate in Gravity-Fed Powder Feeder Systems," *Journal of Manufacturing Processes,* pp. 1-32, 2006.

[105] E. Olevsky, E. Aleksandrova, A. Ilyina, D. Dudina, A. Novoselov, K. Pelve and E. Grigoryev, "Outside Mainstream Electronic Databases: Review of Studies Conducted in the USSR and Post-Soviet Countries on Electrics Current-Assisted Consolidation of Powder Materials," *Materials,* vol. 6, pp. 4375-4440, 2013.

[106] H. Danninger, R. Calderon and C. Gierl-Mayer, "Powder Metallurgy and Sintered Materials," in *Ullman's Encyclopedia of Industrial Chemistry*, Weinheim, Wiley, 2017, pp. 1-57.

[107] S. Rao, "Overview of Finite Element Method," in *The Finite Element Method in Engineering*, Butterworth-Heinemann, 2018, pp. 3-52.

[108] E. Olevsky and D. Dudina, "Sintering by High-Voltage Electric Pulses," in *Field-Assisted Sintering*, Springer International Publishing, 2018, pp. 37-87.

[109] S. Grasso, Y. Sakka and G. Maizza, "Electric Current Activated/Assisted Sintering (ECAS): A Review of Patents 1906-2008," *Science and Technology of Advanced Materials,* vol. 10, pp. 1-24, 2009.

[110] J. Kozlik, H. Becker, J. Strasky, P. Harcuba and M. Janecek, "Manufacturing of Fine-Grained Titanium by Cryogenic Milling and Spark Plasma Sintering," *Materials Science and Engineering,* vol. 772, pp. 1-26, 2020.

[111] Y. Ye, S. Kure-Chu, Z. Sun, X. Li, H. Wang and G. Tang, "Nanocrystallization and Enhanced Surface Mechanical Properties of Commercially Pure Titanium by Electropulsing-Assisted Ultrasonic Surface Rolling," *Materials and Design,* vol. 149, pp. 214-227, 2018.

[112] R. Guo, F. Byus and G. Gerard, "A Journey to Optimal Rolling Mill Design from Provided Product Mix," in *International Conference on Steel Rolling*, Beijing, 2011.

[113] R. Guo, "On the Optimization Procedure of Rolling Mill Design," in *International Exhibition and Conference on Minerals, Metals, Metallurgy and Materials*, New Delhi, 2012.

[114] Y. Yang and M. Qian, "Spark Plasma Sintering and Hot Pressing of Titanium and Titanium Alloys," in *Titanium Powder Metallurgy*, Elsevier, 2015, pp. 219-235.

[115] Z. Esen, E. Bor and S. Bor, "Characterization of Loose Powder Sintered Porous Titanium and Ti6Al4V Alloy," *Turkish Journal of Engineering and Environmental Sciences,* vol. 33, pp. 207-219, 2009.

[116] C. Yu, P. Cao and M. Jones, "Titanium Powder Sintering in a Graphite Furnace and Mechanical Properties of Sintered Parts," *Metals,* vol. 7, pp. 1-14, 2017.

[117] M. Shi, S. Liu, Q. Wang, X. Yang and G. Zhang, "Preparation and Properties of Titanium Obtained by Spark Plasma Sintering of a Ti Powder-Fibre Mixture," *Materials,* vol. 11, pp. 1-10, 2018.

# Appendix A

**MATLAB code for the DPR mill simulation:**

```matlab
d2r=pi/180; %degrees to radians conversion
r2d=180/pi; %radians to degrees conversion


S=1.6; %roll gap
D=350; %roll diameter
W=50; %roll width


K=5.62; %compressibility factor
d=46.91*d2r; %delta - effective angle of internal friction of the powder
m=0.382; %mu - co-efficient of wall friction
p=atan(m); %phi - wall friction angle
u=(pi/4)-(d/2); %another way of expressing internal friction - used in nip
angle determination
n=(1/2).*(pi-(asin(sin(p)./sin(d)))-p); %nu - angle which relates internal and
wall friction


a=12.29*d2r;
nh=(D/2)*sin(a); %nip height in mm


t=0:pi/1000:pi/3;


P0=196000 %40KPa is equivalent to applying the weight of a 10kg mass onto the
powder


%stress gradient in nip region
gn=(K.*(2.*cos(t)-1-(S./D)).*tan(t))./((D./2).*((1+(S./D)-cos(t)).*cos(t)));


%stress gradient in slip region
A=(t+n+(pi/2))/2;
gs=(4.*((pi/2)-t-n).*tan(d))./((D./2).*(1+(S./D)-cos(t)).*(cot(A-u)-
cot(A+u)));


%note that the stress appears in the numerator of both equations above, thus
%when equated (at the nip angle) they can be cancelled out


plot(t*r2d,gs,t*r2d,gn);
title('Determination of Nip Angle');
xlabel('Angular Position (θ)');
ylabel('Stress Gradient (dσ/dx)');
legend('Stress Gradient, Slip Region','Stress Gradient, Nip Region')


f=((pi/2)-n)*r2d; %feed angle in degrees
fh=(D/2)*sin(f*d2r); %feed height in mm


th=0:pi/1000:pi/18;


%mean normal stress in slip region (constant from feed angle to nip angle)
s0=P0/(1-sin(d));
```

```matlab
%mean normal stress in nip region (increasing from s0 at nip angle to sm at
minimum roll gap)
sn=s0*(((1+(S/D)-cos(a))*cos(a))./((1+(S/D)-cos(th)).*cos(th))).^K;

sm=max(sn)

dt=4510;
dr90=0.9*dt;

s1=P0*(1+sin(d))/(1-sin(d));
Pmr=204400000*(dr90/(0.663*dt))^K %required stress at t=0 (ensure this value
is less than sm)

Pm=P0*(sm/s0)*(1-sin(d))/(1+sin(d)) %horizontal stress at min rolling gap
Pm2=2*sm-Pm; %vertical stress at min rolling gap
MA=(sm/s0)*((1-sin(d))/(1+sin(d)));

rde1=2990*10^(log10(Pm/204400000)/K)/dt %expected relative density - from
experiments, 2990kg/m^3 density at 204.4MPa

plot(th*r2d,sn)
xlabel('Angular Position (θ)');
ylabel('Normal Stress (Pa)')
title('Stress Distribution in Nip Region');

fnF=@(t) (((((S./D)./(1+(S./D)-cos(t)).*cos(t)).^K).*cos(t));
F=integral(fnF,0,a);

RF=Pm*(W/1000)*(D/1000)*F/2 %separating force per roll

fnT=@(t) (((((S./D)./(1+(S./D)-cos(t)).*cos(t)).^K).*sin(2*t));
T=integral(fnT,0,a);

TQ=Pm*(W/1000)*(D/1000)^2*T/8 %torque per roll

Tmot=TQ/52; %gear ratio = 52


%linearspeed=RPMroll*pi*D/60
%63-209mm/s linearspeed range used in Muchavi paper
RPMminroll=63/(pi*D/60) %min reasonable rpm for consolidation to occur
RPMmaxroll=209/(pi*D/60) %max reasonable rpm for consolidation to occur
RPMminmot=RPMminroll*52;
RPMmaxmot=RPMmaxroll*52;
fmin=RPMminmot/839*50
fmax=RPMmaxmot/839*50

%max motor torque is limited to 61Nm, therefore maximum roll torque is
%limited to the following:
Tmaxmotor=61
```